Master's thesis

NTNU
Norwegian University of Science and Technology
Faculty of Engineering
Department of Geoscience and Petroleum

Kari Noer Lilli

Ice Growth and Decay on Road Cuts along Bynesveien in Trondheim

Master's thesis in Geotechnology
Supervisor: Reginald Hermanns
June 2020

NTNU
Norwegian University of
Science and Technology

Kari Noer Lilli

Ice Growth and Decay on Road Cuts along Bynesveien in Trondheim

Master's thesis in Geotechnology
Supervisor: Reginald Hermanns
June 2020

Norwegian University of Science and Technology
Faculty of Engineering
Department of Geoscience and Petroleum

NTNU
Norwegian University of
Science and Technology

Summary

The growth, melt and collapse processes of the ice covering a rockwall along road 715 in Trøndelag in Norway were surveyed throughout the winter of 2019/2020, with the aim of investigating the impact of air and rock temperature on its evolution. Daily changes in ice volume were detected by three dimensional photogrammetry models. The models were developed by Structure from Motion with a handheld DSLR camera, and with three action cameras mounted on a moving car. The photogrammetry models were compared to LiDAR models collected on the same day. LiDAR models are assumed to reconstruct the three dimensional surfaces most adequately. The comparison was done to investigate the suitability of the method of photogrammetry for reconstructing ice-covered rock. Additionally, the detailed ice evolution was recorded by an automated camera capturing images every 10 minutes, allowing for exact recordings of ice growth and ice falls. Furthermore, air and rock temperature loggers were installed at the study site. The changes in ice volume were discussed in correlation to the rock and air temperature records, and to temperature data from nearby weather stations.

One main ice formation period in February/March 2020 was observed during the time of study, generating a total ice volume of approximately 25 m^3. The majority of the ice formed during a period of six days with temperatures between 0°C to -8°C. The following six days were characterized by temperatures slightly above 0°C. During that period the ice thickness continued to increase during the first three days, followed by a stabilization of the volume. A temperature increase of 6.7°C/11hrs initiated the ice reduction. The decay occurred as a combination of melting and small ice falls. The rock temperature was above 0°C throughout ice coverage, suggesting that the ice is adhered to the wall by friction and not by ice bridges.

The data were compared to observations from two cold periods in March and November 2019. The latter was documented in a previous specialization project. It consisted of a growth period of 11 days, generating a volume of 29 m^3, followed by ice decay. This was initiated after 11 days of positive temperatures, after a temperature increase of 5°C/7hrs. The decay deviated from that of March 2020, occurring primarily by more massive ice falls, some of which crossed the road. The ice extent of March 2019 was documented by NGU to test the equipment. The ice volume was larger, but no data from the period of decay was documented.

A total of 17 models of Structure from Motion were used to detect the three-dimensional changes in the ice volume throughout the ice formation periods of February/March 2020, November 2019 and March 2019. Investigating the thickness of the ice in limited areas provided a method for detailed observation of changes. The precision of the photogrammetry models increased throughout the period of study, stabilizing on a standard deviation of error of 5-7 mm, as the acquisition procedure and processing were optimized. Large contrasts between rock and ice demand optimal camera exposure for capturing details in both surfaces. Point clouds of low precision were generally associated with over- or underexposed photos. All models demanded a high degree of manual adjustments, largely improving the result. The DLSR models correspond well to LiDAR models with an error of 0±12 mm, an increase from 0±4 mm when no ice is present in the models. The primary error results from poor reconstruction of freely hanging icicles, while the massive ice and surrounding rock reveal small errors.

Temperature data from the last century reveal a large variation in the severity of the winters, with a trend towards an increase of winters with shorter and warmer periods of negative temperatures. Only five winters have had cold periods as short and comparable warm as the winter of 2019/2020. Four of these six winters occurred during the last 13 years. It is suggested that climate change causing larger fluctuations in temperatures from below 0°C to above 0°C, and increased liquid precipitation during winter may result in an increased frequency of ice falls as periods of growth and decay occur several times during one winter.

A total of four minor rock falls were observed along the 340 m long road section during the winter of 2019/2020, supporting the high number of rock falls registered in the public landslide database. Statistics from the study area show an increase in rock falls during winter and spring, suggesting a large impact of freeze-thaw processes on the occurrence of rock falls. Only one of the four mapped rock falls were registered in the landslide database, revealing an under reporting in registrations.

Sammendrag

Dannelse-, smelte- og nedfallsprosessene til en iskjøving langs fylkesvei 715 i Trøndelag i Norge ble kartlagt gjennom vinteren 2019/2020, med det formål å undersøke påvirkningen av luft- og bergtemperatur på endringer i isvolumet. Daglige volumendringer ble dokumentert ved tredimensjonale fotogrammetrimodeller. Modellene ble laget ved hjelp av Structure from Motion, med et håndholdt DSLR kamera, samt med tre actionkameraer montert på en bil. Modellene ble korrelert med LiDAR-modeller fra samme dag. LiDAR-modellene antas å rekonstruere overflaten med høyest nøyaktighet. Sammenligningen ble benyttet for å undersøke egnetheten av fotogrammeteri for å rekonstruere isdekket berg. I tillegg ble isutviklingen dokumentert med et automatisert kamera som tok bilder hvert tiende minutt. Dette ga detaljerte observasjoner av isvekst og isnedfall. I tillegg ble berg- og lufttemperaturloggere installert på studieområdet. Endringer i isvolumet ble diskutert i sammenheng med den registrerte berg- og lufttemperaturen, samt med temperaturdata fra værstasjoner i nærheten.

Én isformasjonsperiode ble observert i løpet av studieperioden i februar/mars 2020. Den genererte et isvolum på omtrent 25 m^3. Mesteparten av isen ble dannet i løpet av seks dager med temperaturer mellom 0°C til -8°C. De påfølgende seks dagene karakteriseres av temperaturer rett over 0°C. I denne perioden økte istykkelsen de første tre dagene, etterfulgt av en stabilisering av isvolumet. En temperaturøkning på 6,7°C/11 timer initierte isreduksjonen. Nedgangen i isvolumet foregikk ved en kombinasjon av smelting og små isras. Bergtemperaturen var over 0°C under hele iskjøvingsperioden, noe som tyder på at isen er festet til veggen ved friksjon og ikke ved hjelp av isbroer mellom isen og berget.

Erfaringene fra denne perioden ble sammenlignet med observasjoner fra to kuldeperioder i mars og november 2019. Sistnevnte ble dokumentert i forbindelse med en tidligere prosjektoppgave. Den besto av en vekstperiode på 11 dager, som dannet et isvolum på 29 m^3, etterfulgt av isreduksjon. Reduksjonen ble initiert etter 11 dager med plussgrader, etter en temperaturøkning på 5°C/7 timer. Isreduksjonen avvek fra mars 2020 ved at den hovedsakelig forekom ved mer massive isras, hvorav noen krysset veien. Isomfanget i mars 2019 ble dokumentert av NGU for å teste utstyr. Isvolumet var noe større, men isreduksjonsperioden ble ikke dokumentert.

Totalt 17 Structure from Motion-modeller ble brukt for å kartlegge de tredimensjonale endringene i isvolumet i løpet av isperiodene i februar/mars 2020, november 2019 og mars 2019. Ved å beregne isens tykkelse i avgrensede områder kunne detaljerte endringer i isen kartlegges. Fotogrammetrimodellenes presisjon økte i løpet av studieperioden, og stabiliserte seg på et standardavvik i feil på 5-7 mm, som følge av at fotograferingen og prosesseringen av modellene ble optimalisert. Store kontraster mellom stein og is krever optimal bildeeksponering for å fange detaljer i både is og stein. Punktskyene med lav presisjon ble assosiert med over- eller undereksponerte bilder. Alle modellene krevde manuelt justerte kamerainnstilligner. Dette forbedret resultatet i stor grad. DLSR-modellene samsvarer bra med LiDAR-modellene med en feil på 0 ± 12 mm, en økning fra 0 ± 4 mm når det ikke er is i modellene. Den primære feilen skyldes dårlig rekonstruksjon av fritthengende istapper, mens massiv is og det omkringliggende berget viser lavere feil.

Temperaturdata fra 1923 og fram til i dag viser stor variasjon i vintrene, med en trend mot vintre med kortere og varmere perioder med minusgrader. Kun fem vintre har hatt så korte og så varme kuldeperioder som vinteren 2019/2020. Fire av de seks vintrene ble observert i løpet av de siste 13 årene. Det diskuteres om økte svingninger i temperaturen over og under 0°C som følge av klimaendringer kan øke israsfrekvensen.

Totalt ble fire mindre steinsprang observert langs den 340 m lange vegstrekningen i løpet av vinteren 2019/2020, noe som underbygger høy steinsprangaktivitet, som dokumentert i NVEs skreddatabase. Statistikk fra området viser en økning i steinsprang om vinteren og våren, noe som antyder at fryse-tineprosesser påvirker skråningens stabilitet. Kun ett av de fire steinsprangene ble registrert i NVEs skreddatabase, noe som antyder stor underrapportering.

Acknowledgements

This thesis constitutes the final work of my 5 years degree in Engineering Geology and Rock Mechanics at the Norwegian University of Science and Technology. The thesis accounts for 30 ECTS, and was written during the spring of 2020. Reginald Hermanns (NTNU/NGU) has been the main supervisor of the thesis and Pierrick Nicolet (NGU) has been the co-supervisor.

I would like to give a large thanks my supervisor, Reginald Hermanns for invaluable guidance, interesting discussions and good help in the field. Furthermore, I owe Pierrick Nicolet a massive thanks for answering all my questions on the topic of the various 3D models, teaching me the different softwares and being available whenever i needed help. In addition, I want to thank NGU for providing me with all the necessary field equipment, a desk at their office and a square in their video meetings when we were all working from home due to the restrictions caused by the Corona virus. Thank you to the IT department at NGU that helped setting up the computer, and aiding with various computer related problems. Thank you to NGI and Statens Vegvesen who have supported the study financially.

Furthermore, I want to thank my friends and classmates for the years in Trondheim, and for invaluable support and distraction throughout the work of the thesis. Thank you to my parents, I am grateful that you are unconditionally impressed by whatever I do and for your excellent comma skills.

I cross my fingers that someone else will continue the work on rockwall icings, as there is certainly more to investigate on this topic.

Trondheim, June 15th 2020

Kari Noer Lilli

Table of Contents

List of Tables

List of Figures

Abbreviations

AADT = Annual average daily traffic
C2M = Cloud to mesh
DEM = Digital elevation model
dGPS = Differential global positioning system
DSLR = Digital single-lens reflex
FDD = Freezing degree days
FDH = Freezing degree hour
GNSS = Global navigation satelitte system
GPS = Global Positioning System
ICP = Iterative closest point
LiDAR = Light detection and ranging
masl. = Meter above sea level
MP = Mega pixel
NGU = Norwegian Geological Survey
NTNU = Norwegian University of Science and Technology
NVE = Norwegian Water Resources and Energy Directorate
RGB = Red green blue
SD = Standard deviation
SDE = Standard deviation of error
SfM = Structure from Motion
SfM-EV = Structure from Motion embarked on a vehicle
TLS = Terrestrial laser scanner

List of Symbols

R^2 = Coefficient of determination
Q_{cc} = Conductive heat flux at rock-ice interface
Q_{cv} = Sensible convective heat flux at air-water interface
Q_{evap} = Latent heat flux at air-water interface
Q_{ice} = Latent heat release during formation of ice
Q_{rad} = Radiative heat flux
Q_{w} = Sensible convective heat flux from flowing water
t = Time [time unit]
t_0 = Beginning of cold period [time unit]
T_a = Air temperature [$^\circ$C]
T_f = Freezing point of water $^\circ$C

Chapter 1

Introduction

1.1 Background of Study

Every winter a large amount of road cuts in cold climate regions are covered by ice of substantial thickness, known as rockwall icings (Gauthier et al., 2015a). The decay and possible collapse of these rockwall icings poses a serious threat to road safety. A collapse may interrupt traffic and impact vehicles, causing economic and personal losses, with the possible consequence of life loss (NRK, 2013). The landslide database of the Norwegian Water Resources and Energy Directorate (NVE) includes close to 6000 registered ice fall events in Norway. In addition to the obvious threat of falling ice blocks, ice growth along road cuts has several secondary effects on the economy and safety of roads. Freezing water is an important weathering process on rock slopes, which over time increases the rock fall hazard (Bjerrum and Jørstad, 1968; Matsuoka and Murton, 2008). Mitigation measures such as rock and ice fall nets may be damaged by the weight of the ice, and thereby increasing the costs related to rockfall protection. Regular removal of ice along the road network may increase the cost of road maintenance significantly (Norem, 1998). Nevertheless, there is very limited research about the topic of the temporal evolution and the meteorological influence on ice growth and collapse, or the impact of rockwall icings on rock falls.

The ice growth along the main road between Trolla and Flakk in Trøndelag, Norway has been studied throughout the winter of 2019/2020. The road cut is covered by thick ice formations every year, thus being known for its good and easily accessible ice climbing possibilities. Moreover, it is known as one of the most landslide exposed roads in the entire region (Adresseavisen, 2012), both in terms of rock and ice falls.

Norem (1998) studied problems related to ice falls on Norwegian roads, with focus on possible mitigation measures. Previous research from Canada and the Alps has shown that the air temperature is the main factor controlling the evolution of rockwall icings (Bianchi, 2004; Gauthier et al., 2013; Gauthier, 2013; Montagnat et al., 2010). Gauthier et al. (2015a,b) proposed models for predicting the ice growth and ice falls along road cuts, based on meteorological data from Northern Canada. Similar studies do not exist neither in Norway nor in other Nordic countries, as far as we know. The Norwegian climate deviate significantly from the climate from which the models were developed, resulting in a need for studying the topic more locally.

Mapping of the temporal change of rockwall icings have previously been performed by simple, two dimensional image analysis based on photos from automated cameras (Bianchi, 2004; Montagnat et al., 2010), and by the use of light detection and ranging (LiDAR) (Gauthier et al., 2015a, 2013). During recent years the three dimensional method of Structure from Motion (SfM) has enabled the mapping of geomorphological changes with accuracies similar to those of traditional photogrammetry and LiDAR (Fonstad et al., 2013; Smith et al., 2016). Despite its limitations in reconstructing reflective surfaces and large contrasts - characteristics that are descriptive of ice - SfM has been applied successfully in studies such as on the mapping of river ice (Alfredsen et al., 2018) and on glacier change (Mallalieu et al., 2017; Piermattei et al., 2015; Whitehead et al., 2013). SfM embarked on a vehicle (SfM-EV) is an even more recent method in the field of geohazard surveying, and has shown acceptable results in change detection (Voumard et al., 2017, 2018). Both methods only require consumer grade cameras, reducing costs significantly compared to LiDAR, and are easy and effective to apply in the field. It is thus of interest to investigate new fields of application for the methods.

1.2 Aim of Study and Methodology

The main goal of this study is to investigate and increase the understanding of the impact of air and rock temperature on the growth and decay of rockwall icings. Other impacting factors such as precipitation, runoff and sun radiation are also briefly addressed, including a discussion on climatic changes. A large focus is on the various methods applied for detecting the temporal changes in ice growth. In addition, the impact of ice formation on road cuts are discussed in regard to slope stability and rock falls.

Following is an overview of the buildup of the thesis, and the various methods applied:

- An introduction to the study site, and a brief overview of historical ice falls in Norway, based on data from NVE's landslide database. Additionally, previous work prepared by the author on the same topic is summarized.
- A literature study on the existing knowledge of rockwall icings. This includes defining the various types of rockwall icings, describing the growth mechanisms, meteorological and hydrological impact on rockwall icings, in addition to presenting the known causes for ice wall failure. Lastly, a brief introduction to the theory behind the method of SfM is presented.
- A description of the methods applied for surveying the ice growth, temperature and rock falls. These include the following:
    - Temperature measurements in the air and the rock, allowing for studying the temperature changes in relation to ice growth and decay, in addition to investigating the correlation between the study site temperature and data from nearby weather stations.

  - Collection of photos with an automated camera positioned at the study site, providing a detailed understanding of the visible ice changes.
  - Sequential photogrammetry models by the method of SfM and SfM-EV, surveying the annual and daily volumetric changes of the rockwall icing.
  - Collection of two LiDAR models, applied as a tool to study the accuracy of the photogrammetry models.
  - Detection of rock falls occurring throughout the winter, based on field mapping and photos.
- A presentation of the results, with a corresponding discussion on the various findings on ice growth and decay, on rock fall impact, and an evaluation of the methods applied.

1.3 Ice Falls in Norway

Rockwall icings are a common sight when driving along Norwegian roads during the winter. A part of the ice falls related to these are being registered in the Norwegian landslide database (NVE, n.d). Figure 1.1 presents a map of all registered ice fall events in Norway. The registered events are distributed unevenly across the country, with a higher density close to the coast, and considerably less ice falls documented inland. In Figure 1.2 the number of ice fall events and the ice fall density (ice falls per km^2) are distributed by region. Sogn og Fjordane and Nordland are the regions with the highest number of registered ice fall events, followed by Troms. The ice fall density is largest in Sogn og Fjordane with a density of 0.08 events per km^2. Vest-Agder, Hordaland, Nordland, Troms and Rogaland follows with around 0.04 events per km2. The data may however be regarded as biased, as registration of ice falls depends on the population and road density. Northern Norway and parts of the inland have a lower population density than other parts of the country, which impacts the number of registrations (Statistisk Sentralbyrå, 2019). In Figure 1.3 all ice falls as distributed throughout the year are plotted, showing most ice falls occurring between mid November and mid May.

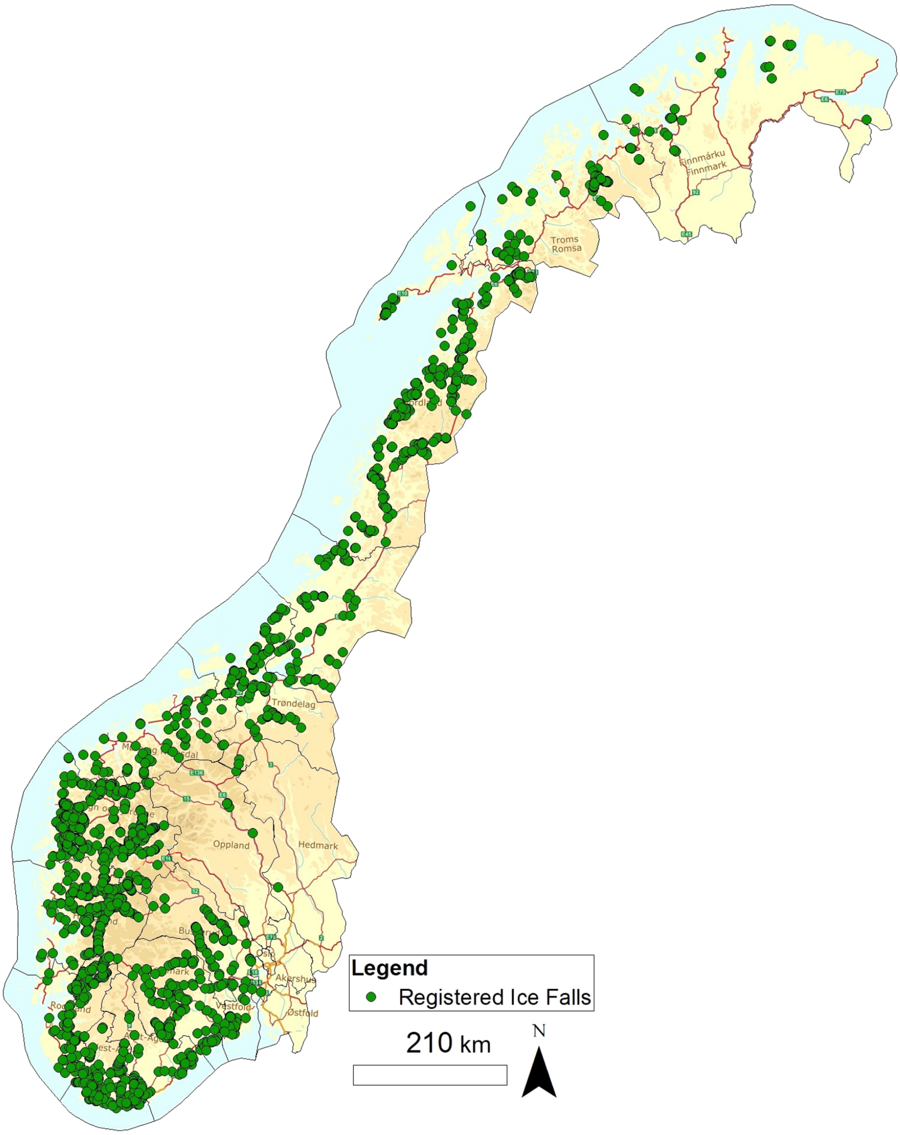

Figure 1.1: All registered ice fall events in Norway marked in green, as registered in NVE's landslide database. Close to 6000 events are registered, with the first event occurring in 1733..

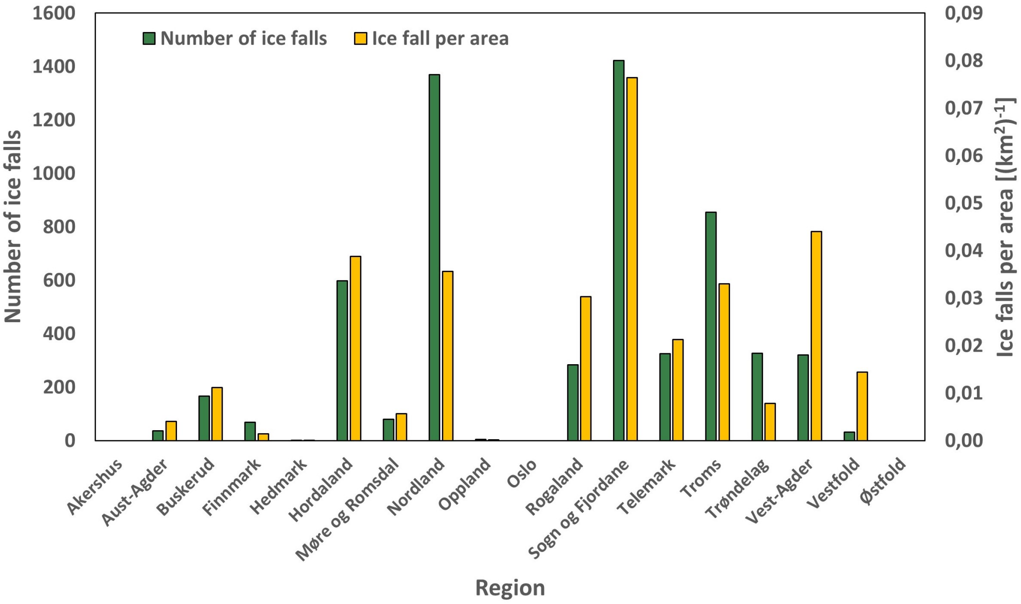

Figure 1.2: All registered ice fall events in Norway divided by region (based on the 2019 division of regions), as registered in NVE's landslide database. The left axis represents the number of ice falls, while the right axis is a measure of the ice fall density per region.

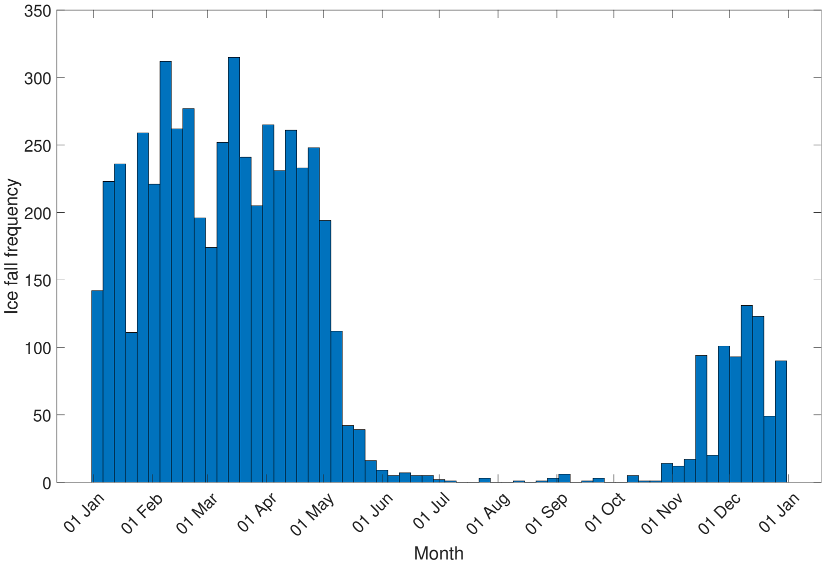

Figure 1.3: All ice fall events registered in NVE's landslide database, as distributed throughout the year.

1.4 Study Site Introduction

The studied road section is situated along Bynesveien, on road 715 in the Trøndelag region in Norway, as mapped out in Figure 1.4. It is situated about 5 km north west of Trondheim city. For surveying the ice growth, two overlapping sections were studied, recognized as section A and B in Figure 1.4. Other than a large ice production during the winter, this particular section was chosen due to practicalities, as it is situated between two rest stops along the road. It was also attempted to locate an area with minor coverage of rock fall nets, as these are known to be poorly reconstructed by photogrammetry (Voumard et al., 2017). Photogrammetry models collected with a handheld digital single-lens reflex (DSLR) camera were created along Section A, in addition to being monitored by a stationary camera, while section B was modelled from images collected with action cameras mounted on a moving car.

Section A is a 40 m long and up to 20 m high road cut. Section B is about 340 m long and has a varying height of 5 to 20 meters. The slope is cut steeply with a dip angle of 80-90°, facing 330 - 340° towards north north-west, receiving close to no sun. A photo of a part of the rock cut is shown in Figure 1.5, taken during a cold period in March 2020. The road follows the fiord at a 30-35 meters distance, at an elevation of about 22 masl. A variety of rock and ice fall mitigation measures are installed along the road, including bolting, rock fall nets, ring net barriers and gabions.

Bynesveien has an annual average daily traffic (AADT) of 3700 cars per day (Statens vegvesen, n.d), and is the main road between Trondheim city and the ferry leading to Fosen. The traffic is thus to a large extent defined by the timetable of the ferry, with cars arriving in intervals, going to or from the ferry. In the periods between the ferry arrivals there are notable less traffic.

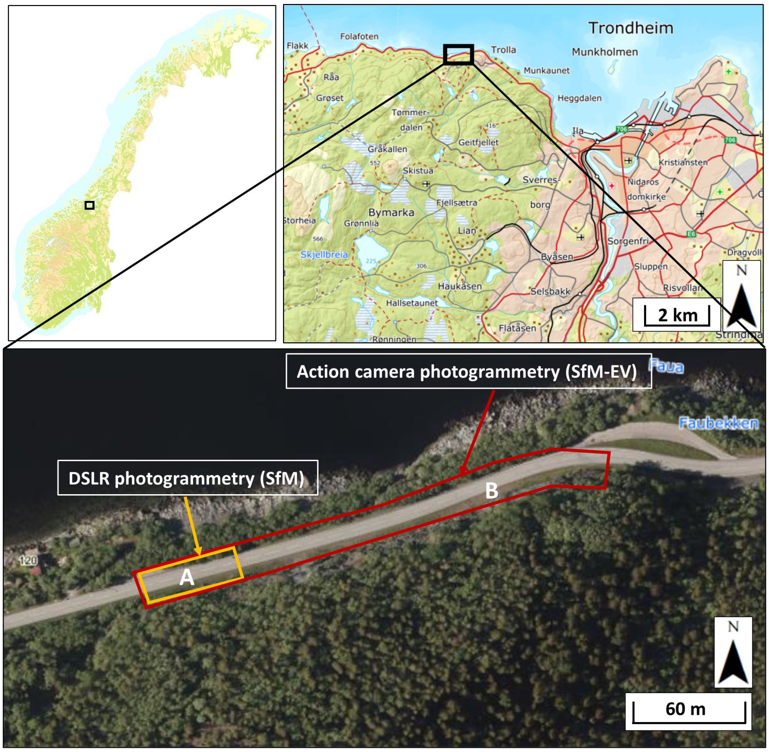

Figure 1.4: Overview map of the road section at which the ice growth was studied. Photogrammetry models were collected using a DSLR camera along section A, while action cameras mounted on a car were used to develop photogrammetry models of section B.

Figure 1.5: The photo is shot at the study site the 3rd of March, when ice had formed after a period of cold temperatures.

1.4.1 Weather and Climate

The study area is situated in the northern part of the temperate climate zone. The climate is relatively mild and wet, with a coastal climate. As the road section is facing towards north northwest and has a steep fall, the site receives close to no sun during the winter months.

The mean temperature and precipitation in Trondheim is presented in Figure 1.6, based on data from 1997 to 2018. December, January and February have a mean temperature slightly below 0°C, while the remaining months are above 0°C. The mean minimum temperature is below 0°C from October to May, while the mean maximum temperature is above zero the entire year, indicating temperatures that fluctuate around zero throughout the winter. The yearly average temperature is 5.9°C. The yearly precipitation is 840 mm per year. The spring months receive the least precipitation, while the late summer and autumn are the periods of highest precipitation (Norsk Klimaservicesenter, n.d).

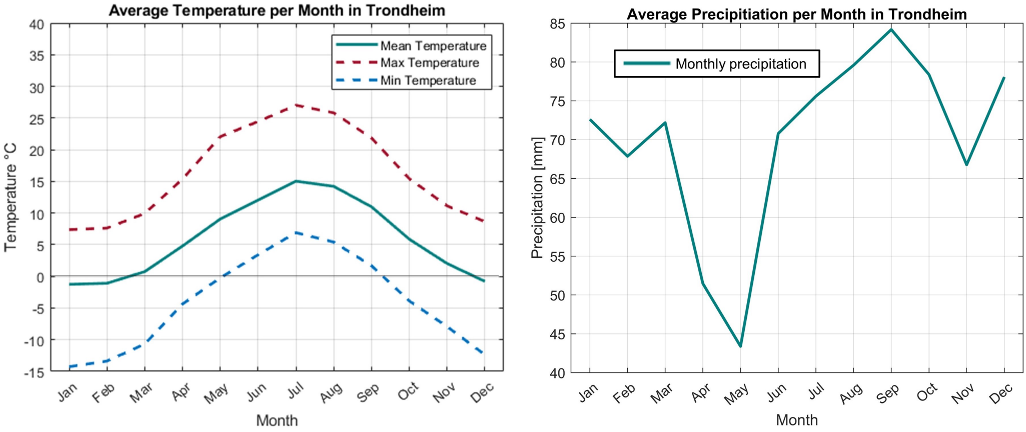

Figure 1.6: Climate data between 1997-2018 in Trondheim. Left: Average temperature, average maximum temperature and average minimum temperature per month. Right: Average precipitation per month. The data are recorded as Voll weather station, see Figure 3.3 for map.

1.4.2 Geology

The study area is a part of the Støren Nappe, which is one of three geological groups constituting the Trondheim Nappe Complex. The Støren Nappe is interpreted as oceanic crust lifted during the Caledonian orogeny. It consists of several kilometers of deformed pillow lava and volcanic intrusions, with layers of chert and phyllite, as well as gabbro and ofiolittic fragments (Fossen et al., 2013; Gale and Roberts, 1974). Bynesveien is situated within an area of greenstone and greenschist, interrupted by sections of trondhjemitt and quartz keratophyre, as shown in the map in Figure 1.7 (Solli et al., 2003).

The study area is situated below the marine limit. The surrounding soils mainly consist of thin moraine deposits and weathered material, as presented in Figure 1.8.

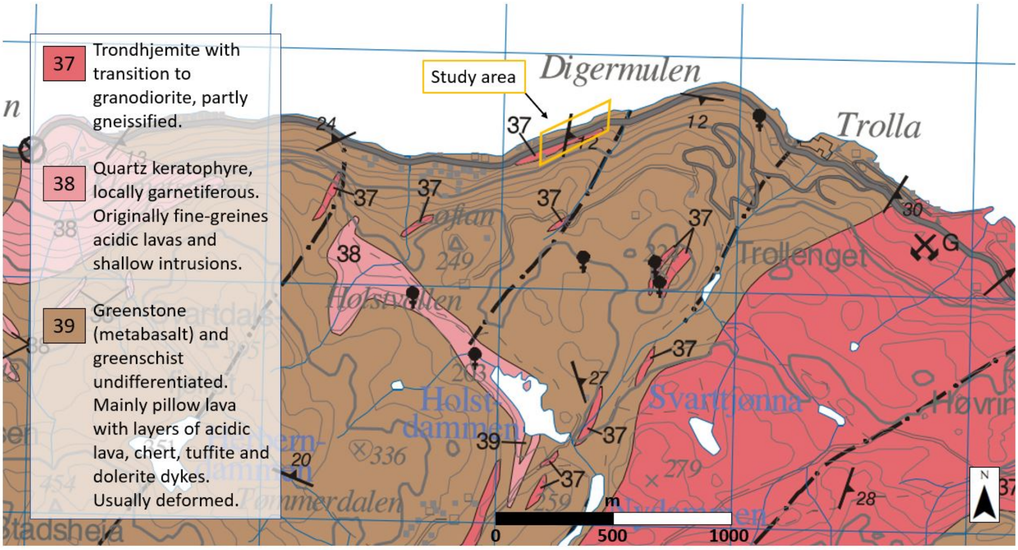

Figure 1.7: Geological map of the study area and the surroundings. The study area is marked in yellow. Map modified from Solli et al. (2003) (NGU).

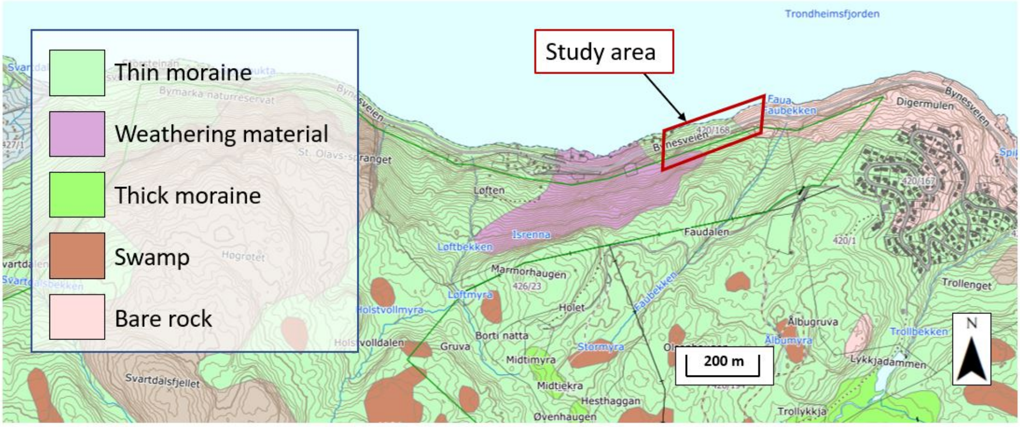

Figure 1.8: Quarternary map of the study area and the surroundings. The study area is marked in red. Map modified from NGU (n.d).

1.4.3 Rock and Ice Fall Events along the Study Site

Bynesveien is known to be heavily impacted by landslides, and particularly rock and ice falls. According to the Norwegian Public Roads Administration it is one of the most landslide exposed roads in the Trøndelag region (Adresseavisen, 2012), and there is ongoing work for investigating the possibility of building a tunnel along the stretch (Adresseavisen, 2020). Figure 1.9 shows several photos of ice and rock falls that have occurred along Bynesveien during previous years.

Figure 1.9: Photos from Bynesveien captured during previous years, showing removal of ice along the road, and one of many rock falls reaching the road. The figure to the right is taken on the 21st of March 2019. The date is unknown for the two other photos. Photos: Agnethe Weisser, Rune Petter Ness, Morten Antonsen (Adresseavisen, 2020).

Between 2000 to 2020 a total of 29 rock and ice falls are registered in NVE's database along a 1 km long section of Bynesveien, presented in Figure 1.10. These consist of 3 ice falls and 26 rock falls. Along the 340 m long study area, a total of 10 rock falls are registered, in which one was recorded during the winter of 2020, on February 21st. Several rock and ice falls have however been observed during the period of study, of which only one was registered, inferring a large under reporting of events.

Alvestad (2016) studied the road section between Trolla and Flakk in his master thesis, with the main focus of identifying the landslide hazard along the road section. Six localities along the study area were considered particularly prone to rock fall. The volumes are estimated to be between small rock blocks of 0.1 m^3 to larger blocks of up to 70 m^3.

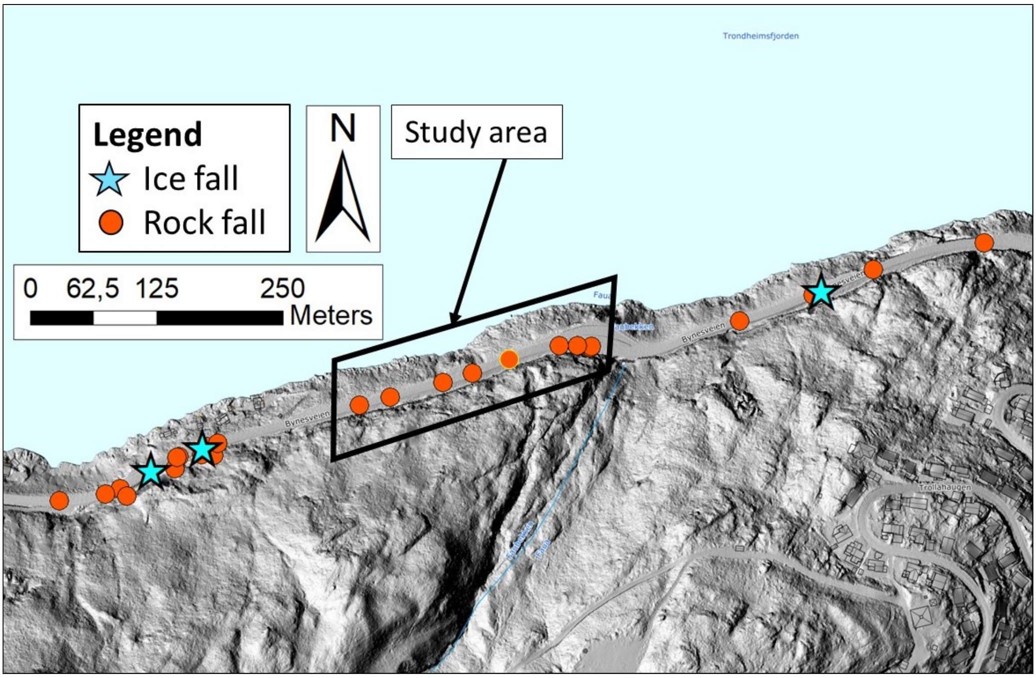

Figure 1.10: Registered landslides along the study area and its proximity. A total of 9 rock falls are registered along the 340 m long study area. One rock fall was recorded during the period of study, marked by a yellow circumference. Data from NVE's landslide database (NVE, n.d)

1.5 Summary of Initial Work

As part of the preparatory work for this thesis, the author prepared a 15 ECTS specialisation report on the topic of rockwall icings during the autumn of 2019 (Lilli, 2019). Following is a summary of what was included in the report, and the most important results.

- A literature study on the existing knowledge of rockwall icings and ice falls. A large part of the literature study is repeated in this thesis, as it is just as relevant for the work presented.
- A statistical overview of historical ice fall data in Norway, and particularly in the region of Trøndelag. This provided a basis for establishing the ice fall frequency on Norwegian roads and investigating the extent of the problem. Furthermore, historically registered ice falls were correlated to meteorological data, as an attempt to understand the meteorological conditions favouring ice falls. The analysis was based on ice fall data from the landslide database. In total, 57 registered ice falls were correlated with temperature and precipitation data from four different weather stations in Trøndelag. Days of ice falls were characterized by daily temperature means between 0 to 7 °C. The majority of ice falls occurred on days with maximum temperatures between 4°C to 11°C. In addition, precipitation seemed to accelerate the ice fall frequency, as the majority of the ice falls occurred succeeding precipitation. The correspondence between the position of the ice falls and the position of the

weather station was however not studied, thus it was not known whether the meteorological data were actually representative for the ice falls. In addition, the registered time of the ice falls may be inaccurate, and a large proportion of the ice falls are never registered, making such an analysis challenging.

- An initial study on the feasibility of photogrammetry for estimating ice volume. Two photogrammetry models were collected with a DSLR camera, one containing no ice (03.10.2019) and one collected after a period of ice formation (11.11.2019). The methods for processing and aligning the point clouds were equal to the methods that will be presented later. Both models are included in this thesis.
- A stability analysis of the studied road cut. The analysis was based on geological field work and a kinematic feasibility test. The rock mass was interpreted to consist of mainly green schist, with interrupting dykes of granodiorite. It is deformed, with repeating deformation planes along the entire section. The rock mass consists of three main joint sets (J1-J3) with dip/dip direction of respectively J1: 83°/211°, J2: 89°/125°and J3: 86°/346°. In addition, there are two deformation planes (D1-D2) that are repeated throughout the entire section. Their dip/dip direction is D1: 49°/117°and D2: 70°/330°. The foliation is close to horizontal with a dip/dip direction of 15°/108°. The kinematic analysis investigated the probability of planar sliding, wedge sliding and block toppling. The most probable failure mechanism was found to be wedge sliding, followed by planar sliding and lastly toppling. The deformation plane D2 largely affects the stability of the slope, and 100% of the registered D2 planes are feasible for either planar sliding or wedge sliding.

Chapter 2

Theory and Existing Knowledge

2.1 Rockwall Icings

Following is an overview on the existing knowledge on rockwall icings. This includes a definition of the different types of rockwall icings, and an overview of the various factors impacting the growth and decay of rockwall icings. Lastly, existing knowledge on ice falls and driving forces are presented, as well as the impact of ice on rock slope stability. Chapter 2 was written during the work of the specialization report (Lilli, 2019), and is also fully relevant for this thesis. The following is thus copied directly from the specialization report, with some minor modifications.

2.1.1 Classification of Rockwall Icings

Rockwall icings are created when runoff water or precipitation gradually freeze when percolating over a rockwall. The dimensions of the rockwall icings may vary from small freely hanging icicles, to massive meter thick walls of ice (Gauthier et al., 2015a).

A rockwall icing may be classified in several ways. Gauthier (2008) suggested using the terms «ice cascade» or «ice waterfall» when the rockwall icing is developed from the freezing of persistent surface runoff such as streams, waterfalls, and snow melt, and «ice wall» when groundwater seepage percolates over a cliff face and freezes. Bianchi (2004) divides the ice cascades into «frozen waterfalls with flow» and «ghost frozen waterfalls». The first one refers to ice cascades developed from the freezing of continuous waterfalls, while ghost frozen waterfalls originates from intermittent flows created due to rainfall or snow melt (Bianchi, 2004; Gauthier et al., 2013).

Rockwall icings consist of ice developed from three different sources, as listed below. One rockwall icing may contain ice originating from all three sources (Bianchi, 2004):

- Ice developed from the freezing of water.
- Ice developed from droplets created by waterfall spray.

- Ice developed from snow that has undergone metamorphosis.

Research on the topic of rockwall icings, and thus the definition of terms is generally new. However, climbers have used ice as a climbing medium since the 1970s. One type of classification used by the international ice climbing community is the terms stalactite, free-standing columns and ice columns, presented in Figure 2.1. This division is also an indicator of the mechanical strength of rockwall icings, as stalactites and free-standing columns generally tend to be less strong compared to ice columns attached to the rockwall (Lowe, 1996; Montagnat et al., 2010).

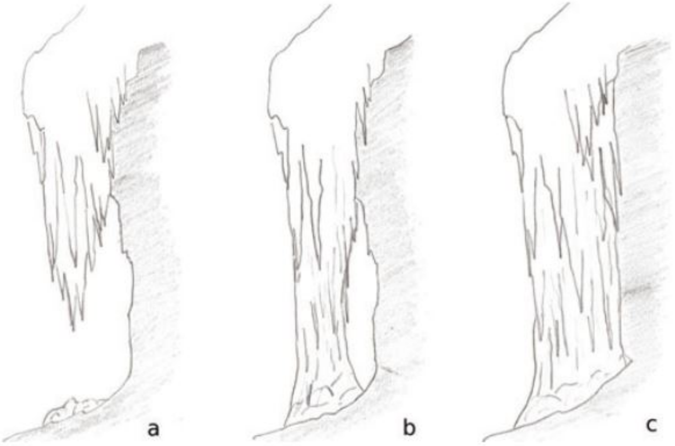

Figure 2.1: Types of rockwall icings, as known by the international ice-climbing community. The sketch shows: A) ice stalactite, B) free-standing waterfall and C) ice column (Montagnat et al., 2010).

2.1.2 Meteorological Impact on the Growth of Rockwall Icings

The growth of rockwall icings is highly dependent on the meteorological conditions. The climatic factor having the largest impact on the formation of ice walls and ice cascades is the air temperature (Bianchi, 2004; Gauthier et al., 2013; Gauthier, 2013; Montagnat et al., 2010). The parameters freezing degree hours (FDH), and freezing degree days (FDD) have been used successfully as a parameter to describe the general evolution of ice walls and ice cascades (Gauthier et al., 2015a; Montagnat et al., 2010). It is traditionally used to estimate the trends and severity of winters (Assel, 2003), and for empirical calculations of lake ice thickness (Hinkel, 1983). It is essentially a measure of how cold it has been for how long. FDH is calculated as:

$$FDH = \int_{t_0}^{t} (T_f - Ta)dt \tag{2.1}$$

where T_f is the freezing point of water (0°C) and T_a is the hourly mean air temperature. The minimimum value of the parameter is 0, such that if the sum become negative due to a longer period of plus degrees, the sum will be reset to zero. The equation of FDD is equal, but T_a is the mean temperature of each day.

In addition to temperature, the growth potential of rockwall icings depends on several other meteorological factors, and a factor solely based on temperature is thus not able to completely predict the ice growth evolution. The amount of liquid precipitation and water available for freezing certainly impacts the ice growth and decay. With air temperatures above zero, the supply of liquid precipitation and melt water will add energy to the ice, resulting in ice decay. Gauthier et al. (2015a) studied the correlation between precipitation and the ice volume of rockwall icings, but did obtain any clear correlation. Furthermore, direct solar radiation may impact the growth and decay to a large extent. This results in different melting regimes for different orientation of the rock slope. Lastly, the air humidity, wind speed and wind direction do also impact, but have been found to be of less importance (Gauthier et al., 2015a,b). A quantitative correlation between these factors and the ice growth have been studied, but no clear relation has been established (Gauthier et al., 2015a).

2.1.3 Hydrogeological Conditions Impacting Ice Growth

In addition to the climatic factors, hydrogeological factors impact ice growth along rockwalls, in particular in defining the spatial distribution and the volume of the icings. During negative air temperatures, a high water flow results in low growth rate due to the large energy transfer from the water. The largest icicles form under conditions where the initial water supply is low, followed by a continuous increase in the water supply, as the ice grows larger (Makkonen, 1988). The water available for freezing thus works as a limiting factor on the size of the icing. The water may either derive from surface water, from water in the unsaturated zone, or from groundwater. (Liereng, 2016).

Surface water is concentrated in draining paths forming streams, rivers and waterfalls. These channels are characterised by being water filled throughout the whole year, fed by a larger catchment and water magazines above. As the water source is consistent, these drainage paths may result in the formation of large ice cascades (Liereng, 2016; Norem, 1998).

Ice walls are most commonly formed along road cuts that are surrounded by layers of soil with high permeability (Norem, 1998). These are soils such as fluvial and glaciofluvial deposits, moraine soils or swamps. Rockwall icings often start forming at the boundary layer between the soil and the rock, where the water is forced out over a rock cut (Norem, 1998). In the unsaturated zone the water source is typically intermittent and dependent on the amount of precipitation, such that the size of the ice walls is limited (Liereng, 2016).

Groundwater in rock joints may also be a source for rockwall icings. The joint spacing, persistence, aperture, weathering and joint infill are factors that impact the permeable properties of the rock (Wyllie and Mah, 2004). According to Norem (1998) it is, however, rare that water from joints make a considerable impact on the formation of rockwall icings, as the amount of water often is relatively small. Weak rock types tend to generate more rockwall icings compared to hard rock. This is assumed to be related to the weak rocks producing a more fertile soil during weathering, which may create thicker vegetation layers and thus have a larger water storage available for freezing (Norem, 1998).

A large portion of problems related to rockwall icings are due to human interventions. The creation of road cuts changes the hydrogeological regime, forcing the surface- and groundwater to take new paths (Norem, 1998).

In the eastern part of Norway the winters are mild and precipitation is high. The inland receive less precipitation, and have colder winters. The latter results in a deeper frost line, and a larger amount of the stored water freezes in situ. This creates low water surface discharge during the winter and thus a lower potential for the creation of large ice formations along rockwalls (Norem, 1998). This contributes to the ice fall pattern as seen across Norway, with less ice falls inland than along the coast.

2.1.4 General Thermodynamics

Heat transfer occurs through three different processes, which are all active during the formation of rockwall icings. These consist of conduction, convection and radiation. Heat conduction is the movement of heat between objects of different temperatures and are transferred by vibration and colliding atoms in an object. The heat transfer can occur between liquids, solids and gases, but does not include transport of materials. Convective heat transfer is related to the energy transfer between a moving fluid or gas, such as blowing wind or moving water, and does include transport of materials. Radiative heat is transferred through electromagnetic waves, and is emitted without direct contact between the objects. All surfaces above absolute zero emits radiation heat (Sonntag and Borgnakke, 2013).

The heat transfer can further be divided into sensible and latent heat. These defines the effect that the energy transfer has on an object. Sensible heat is energy that contribute to the temperature change of an object, such as the heating of water and warming of ice, but it does not change the phase of the object. Latent heat, on the other hand, does not change the temperature of the object, but the phase of the object. This includes melting/freezing of ice/water, evaporation and condensation (Rao, 2011; Sonntag and Borgnakke, 2013).

2.1.5 The Thermodynamics of Rockwall Icings

When ice freezes, latent heat is created and must be removed in order for the ice to continue growing. The speed at which the latent heat is removed by the environment thus controls the growth of the ice (Makkonen, 1988).

Following is an overview of the various heat fluxes that are assumed to be involved in the evolution of ice on a rockwall. Gauthier et al., 2013 and Gauthier et al., 2015a proposed a thermodynamic model of ice growth along rock walls, based on empirical data from three ice walls and one ice cascade in Northern Canada. Figure 2.2 presents a simplified theoretical model which address all heat fluxes. The volume V is the amount of ice that results anchored to the wall. A certain percentage freezes to ice, but evacuates the system and does not contribute to the ice volume along the wall, represented as $\%$ ice in Figure 2.2. The energy balance between the rock, ice, water and atmosphere interface, as proposed by Gauthier et al., 2013 is written as:

$$0 = Q_{cv} + Q_{evap} + Q_{cc} + Q_{rad} + Q_w + Q_{ice} \tag{2.2}$$

Q$_{cv}$ is the convective sensible heat transfer between the air and water interface. The movement of air around the flowing water, or the falling of water droplets may either add energy, and thus heat to the water, or extract energy from the water decreasing the water temperature. Q_{cv} depends on the air temperature and the wind speed. Q_w is the sensible convective heat from the water to the ice. It is highly dependent on the water discharge, and thus the amount of available water that can form ice. The temperature of the water also impacts Q_w. Q_{evap} is the energy resulting from the latent heat released during evaporation of water, while Q_{ice} is the latent heat released during freezing of water. Q_{rad} is the sum of the incoming and outgoing radiation to the surface (Gauthier et al., 2015a). All objects emit radiative heat thorough electromagnetic radiation. Radiative heating from the sun will contribute to melting of the ice during the day. On a cloudless night sky the radiative heat from the atmosphere can drop below zero, resulting in outward radiation from the ice to the atmosphere (Hamberg et al., 1987). The radiative heat mainly depends on the air temperature and the sun radiation. Q_{cc} is the conductive heat transferred directly between the rock and the ice wall. It mainly depends on the temperature of the rock and the thermal conductivity of the rock (Gauthier et al., 2015a, 2013).

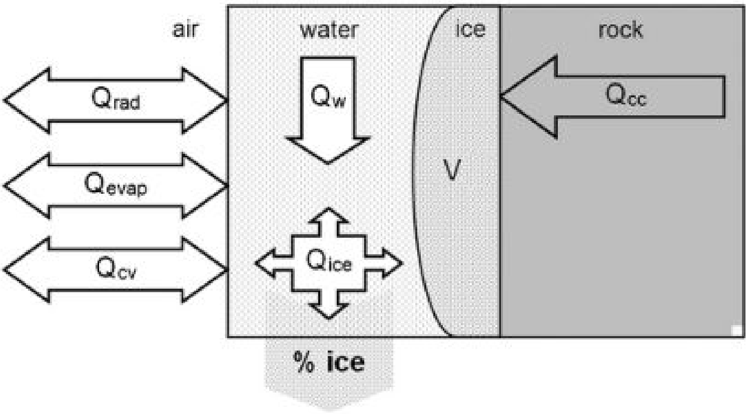

Figure 2.2: A conceptual and simplified model of the heat transfers occurring in relation to the evolution of rockwall icings. The model is developed by Gauthier et al., 2015a.

Gauthier et al. (2015a) found that the convective heat flux (Q_{cv}), which is dependent on the air temperature and wind speed, is the main factor influencing the growth of both north and south-facing ice walls. In north-facing walls, the radiative heat Q_{rad} is of low importance, while on south facing walls Q_{rad} from the sun impacts the ice growth to a larger extent. For melting of the ice walls, Q_{cv} is the factor that influences the melting process the most on north facing walls, while on south facing walls the solar radiation is the most important factor.

Furthermore, a low water discharge favours the ice growth, while increasing flow generally decrease the growth or favours melting (Gauthier et al., 2013; Maeno et al., 1994; Makkonen, 1988). Q_{evap} proved to be important during the initial ice growth when the temperature is slightly below zero, and the humidity is low. The heat exchange between the ice and the rock surface (Q_{cc}) was found to be of lower importance.

It is however important to take into account that the findings from Gauthier et al. (2015a) and

Gauthier et al. (2013) are based on field results from Northern Canada, which generally experience temperatures far below the temperatures in Trøndelag, has longer periods of consistent negative temperature and accumulate more precipitation. The results are thus not necessarily directly transferable to the Norwegian climate.

2.1.6 Ice Block Failure

The failure probability of ice blocks along rock cuts depends on meteorological factors such as temperature and precipitation, hydrological factors such as the runoff amount and water source, glaciological factors such as the ice structure, and geomorphological factors such as slope angle and aspect (Bianchi, 2004; Gauthier et al., 2015a; Montagnat et al., 2010; Weiss et al., 2011). Recent research have attempted to predict ice block falls based on both a qualitative and quantitative approach. The research is mainly based on data from the French and Italian Alps (Bianchi, 2004; Weiss et al., 2011) and from Northern Canada (Gauthier et al., 2015b; Gauthier et al., 2012; Graveline and Germain, 2016).

Bianchi (2004) proposed the following list of hydroclimatic situations that may destabilise rockwall icings and increase the probability of ice falls.

- High maximum temperatures or sudden increases in temperature.
- Indirect heat from solar radiation, warming the air and the rocks.
- Large variation in daily temperature.
- Sudden increase in water discharge.
- Sudden drops in temperature.

Weiss et al. (2011) studied the mechanical stability of ice waterfalls in the Alps. The results indicated that more than three days of temperatures above 0°C generally creates favourable conditions for ice failure. Furthermore, sudden temperature drops of several $^{\circ}\mathrm{C\ h^{-1}}$ and low air temperature (less than -10°C) induce tensile stresses far above the tensile strength of ice, and may lead to a collapse. Periods where the temperature fluctuates above and below 0°C during day and night, were found to not necessarily create ice block falls, as the ductility of the ice prevents the creation of cracks.

Gauthier et al. (2015b) proposed a predictive model for ice block falls based on data from Northern Canada. The best fitting model is based solely on different air temperature variables and is capable of predicting some of the largest ice collapses that occurred at the study area. The model does, however, not include the precipitation, which from ice fall records is shown to have a large impact on the ice fall probability (Gauthier et al., 2015b).

Furthermore, the solar irradiance impacts the size of the ice falls. Roads facing towards south generally generate smaller ice volumes. The ice is however more sensitive to sunny days, and may experience several smaller ice falls during a day of sun. North facing walls are less impacted by the solar irradiance and thus form larger ice volumes. This results in a lower ice fall frequency, however, when ice fall do occur, they may be of larger volumes (Norem, 1998).

Norem (1998) divides ice falls from rock slopes into three different types, based on the failure mode. These are similar to the failure mechanisms of rock falls. The mechanisms include toppling, direct fall and sliding, as presented in Figure 2.3. Ice falls generally have a shorter travel length compared to other landslides, often 3-6 m, and rarely more than 10-15 m (Norem, 1998).

Toppling occurs along steep rock cuts where the ice is supported in the bottom (free-standing waterfall or ice column as defined in Figure 2.1). For toppling to occur the entire back of the ice wall must be detached from the rock wall, such that it is only supported by the toe of the ice column. Due to this, toppling typically occur late in a melting period.

Direct fall is ice fall from ice hanging more or less freely (ice stalactite in Figure 2.1). It is dependent on the shear and tensile strength of the ice. This failure type typically occurs first during a melting period and often release relatively small blocks.

Sliding occurs on sloping rock walls where the ice is attached to the rock. The minimum angle of failure depends on the roughness of the slope. Water between the ice and the rock may contribute to ice sliding on low angled slopes. Norem (1998) found that slopes of 45° to 55° have the longest runout length. This type of ice fall generally occurs late in the season after longer periods of melting.

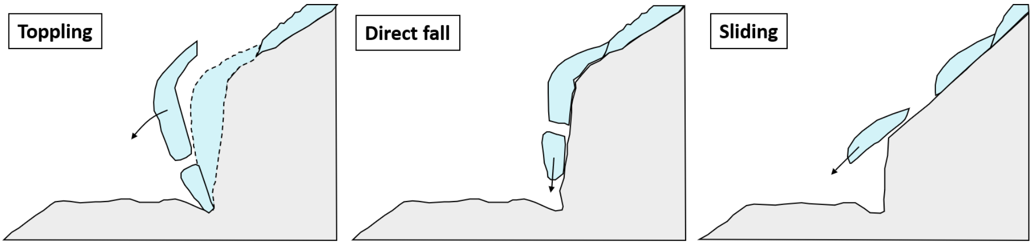

Figure 2.3: Conceptual sketch of the three main types of ice block failure: toppling, direct fall and sliding, as proposed by Norem (1998). The figure is modified after Norem (1998).

2.1.7 Ice Growth Impact on Rock Slope Stability

Frost weathering occurs wherever the temperature fluctuates around 0°C, and where there is moisture available. Freeze-thaw cycles impacts rock strength and rock slope stability in several different ways; during the phase change from water to ice, during the period of stable ice, and during the phase change from ice to water (Matsuoka and Murton, 2008).

The phase change from water to ice impacts the joint properties and reduces the strength of the rock mass. The volume of water increases by approximately 9% during freezing. This may result in joint wedging and increased joint aperture, or may progress existing joints. In hard rock the joint frequency governs the ice weathering to a large extent, while in soft rock, ice weathering is also dependent on the porosity and the strength of the rock. The freezing of ice may also lead to blockage of drainage paths, resulting in the groundwater taking new paths, and possibly changing the stress conditions in the rock mass (Matsuoka and Murton, 2008).

It is well known that the presence of ice in discontinuities generally stabilises the rock slope due to its adhering effect on rock (eg. Bjerrum and Jørstad, 1968). Studies have however shown that at temperatures close to zero and certain normal stresses, an ice filled joint may have a lower shear strength than an ice-free joint (Davies et al., 2000; Davies et al., 2001; Patton et al., 2019).

The rockfall frequency in alpine and sub-alpine environments is often well correlated with the freeze-thaw season in late autumn and early spring (Bjerrum and Jørstad, 1968; Douglas, 1980; Matsuoka and Sakai, 1999). The cementing effect that the ice has on the rock is reduced during melting, which decreases the stabilising forces on the rock slope. In addition, the water content in the rock slope increases during melting of the ice, resulting in larger water pressures on the rock joints.

The depth to which the ice penetrates into the rock is mainly dependent on the temperature and duration of the freeze-thaw cycles, the water content, the thermal conductivity of the rock and the thickness of the ice adhered to the surface (Matsuoka and Murton, 2008). Freeze-thaw cycles vary between daily periodicity, annual cycles and long term cycles resulting from climate change. Daily cycles usually result in limited ice depth penetration (<50 cm) (Matsuoka, 1994), which may break down the rock, creating blocks of pebble to cobble size. Seasonal variations may impact the rock on a meter scale. As the freezing occur at a slower rate during annual cycles, the impact on joint wedging tend to be somewhat smaller (Matsuoka and Murton, 2008). Lastly, impact from long term cycles typically include permafrost. The thawing of permafrost has shown to be of impact on the stability of rock slopes (eg. Krautblatter et al., 2013).

2.2 Photogrammetry - Structure from Motion

SfM is a method used to reconstruct three dimensional objects from a set of overlapping photographs taken from multiple viewpoints, as illustrated in Figure 2.4 A. The method relies on an iterative bundle adjustment solving the geometry of the feature and the camera positions and orientations, without the need of a pre-calibrated camera or physical targets with known position (Westoby et al., 2012). This results in a fast and low cost method, compared to traditional survey methods (Bemis et al., 2014). Studies have shown that SfM in many occasions produces results as good as airborne and terrestrial laser scanning (eg. Fonstad et al., 2013; Wilkinson et al., 2016).

SfM embarked on a vehicle (SfM-EV) is a method of photogrammetry where the cameras are mounted on a moving body, allowing for fast photo acquisition, and the possibility of surveying large areas in a short amount of time. The method is illustrated in Figure 2.4 B. Action cameras are commonly used, as they are easy to mount on various bodies, they are robust and small, and the wide angle captures a large view. The main disadvantages are the reduction in photo quality, and less possibility for manual control of the settings (Voumard et al., 2018).

There are several recommendations on the data acquisition for SfM in order to obtain an optimal result. Each point on the photographed surface should appear in a minimum of two photos taken from different angles, however more photos will largely improve the reconstruction of the feature. The optimal amount of images depends on the complexity and size of the feature (Smith et al., 2016). Furthermore, a maximum angular change of 10° to 20° between each camera position (referred to as "station") is advisable. Moving objects such as vegetation moving due to wind might reduce the quality of the data (Bemis et al., 2014). Increasing the resolution of the input photos may increase the model quality, however this will lead to larger processing times (Westoby et al., 2012). For SfM-EV the distance to the photographed feature and the speed of the moving vehicle largely impacts the result. Voumard et al. (2017) found that at distances larger than 25 m and/or at velocities above 25 km/hr, the reconstruction accuracy was notably decreased.

Reflective surfaces such as ice and water may be challenging to reconstruct due to the appearance changing depending on the angle from which it is seen (Bemis et al., 2014; Smith et al., 2016). Successful studies on ice using SfM have however been published, such as on river ice (Alfredsen et al., 2018) and on glaciers (Mallalieu et al., 2017; Piermattei et al., 2015; Whitehead et al., 2013). Sharp contrasts in an image due to solar shadows, and change in texture may also reduce the quality of the model (Gómez-Gutiérrez et al., 2014).

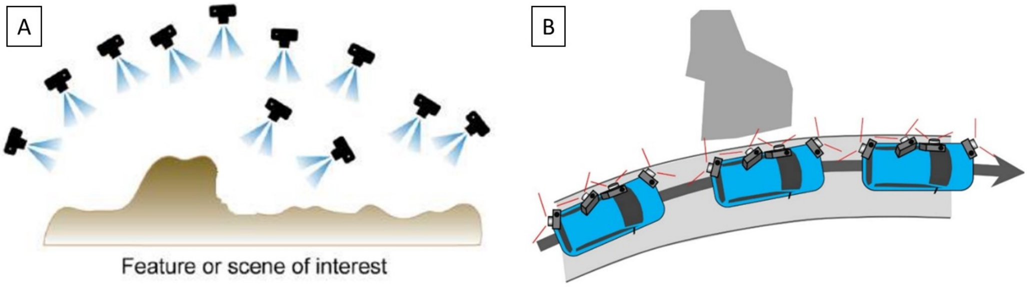

Figure 2.4: Survey methods of SfM. A) Illustration of the image acquisition for creating 3D models by the method of SfM. At each camera position several photos are collected, covering the entire area. The model requires images from different positions and camera angles. Modified after Schwind and Starek (2017). B) SfM embarked on a moving vehicle, such as on cars, trains, bicicles etc. allows for faster aquisition of photogrammetry models (Voumard et al., 2018).

2.3 Light Detection and Ranging (LiDAR)

Light Detection and Ranging (LiDAR) is an active remote sensing method used to obtain high accuracy point clouds of the geometry of objects, by the use of laser. It consist of a scanner with a transmitter/receiver that emits highly directional infrared laser pulses. The pulses are back-scattered when impacting objects and the delay in travel time is used for calculating the distance to the object. In addition, the incoming angle of the pulse is registered by the scanner. This results in an X Y Z position of each point of back scatter, and a scan thus results in a point cloud where each point corresponds to a scatter point (Jaboyedoff et al., 2012). The scanner may be airborne (ALS) or operated from the ground, so-called terrestrial laser scanner (TLS). The latter is utilized in this study.

In addition to registering the coordinates of each point in the LiDAR point cloud, the scanner registers the intensity of each point. The intensity is a measure of the ratio between the emitted signal and the received signal. It depends primarily on the distance to the scanned object, the incident angle, the geometry of the object, and the moisture and type of material scanned (Abellán et al., 2011).

Chapter 3

Methods

3.1 Temperature Measurements

A total of 14 temperature loggers were installed at the study area along section B (Figure 1.4). 11 loggers were installed into the rock and 3 air temperature loggers were installed at the site, inside ratiation shields. The period of data acquisition was between November 29th and May 1st. The logger info is listed in Table 3.1, with the position indicated in Figure 3.1. Figure 3.2 shows photos of the field installations.

The temperature loggers are of the type iButton DS1922L-F5#. According to the manufacturer, the loggers have a temperature accuracy of ± 0.5 °C. They were programmed to register the temperature once every hour. All loggers were placed inside a rubber pocket, shown in Figure 3.2 C, as this reduces the impact of the conductive heat from materials in direct contact with the logger. The rock temperature loggers were installed along the rock cut, attempting to have an equal distribution of loggers being covered and not covered by ice. They were installed at a depth of 1.5-3.5 cm into the rock, secured with silicon, sealing in the borehole. All air temperature loggers were placed inside a radiation shield, as shown in Figure 3.2 B, in order to omit the impact from thermal radiation, as well as protecting the loggers from dirt, snow, etc. One air temperature logger was installed in a lamppost along the road, while two others were installed in the same shield in a tree, positioned approximately 3 meters above the road. Photos of the position of the rock temperature loggers are given in Appendix A.

Table 3.1: Summarising table of the 14 installed loggers. Three loggers measured air temperature, while the remaining were installed in the rock wall. Three of the rock loggers appeared to be defect and did not record any data.

Logger ID	Medium	Date installed	Date extracted	Installation depth
001	Air	29.11.2019	06.04.2020	-
002a	Air	12.11.2019	06.04.2020	-
002b	Air	12.11.2019	06.04.2020	-
411a	Rock	29.11.2019	06.04.2020	Defect
411b	Rock	29.11.2019	02.04.2020	2.4
412	Rock	29.11.2019	02.04.2020	2.4
413	Rock	29.11.2019	06.04.2020	2.2
414	Rock	29.11.2019	01.05.2020	2.5
415	Rock	29.11.2019	01.05.2020	Defect
416	Rock	29.11.2019	01.05.2020	3.5
417	Rock	29.11.2019	06.04.2020	3.6
418	Rock	29.11.2019	01.05.2020	3.5
419	Rock	12.11.2019	01.05.2020	Defect
420	Rock	12.11.2019	01.05.2020	3.5

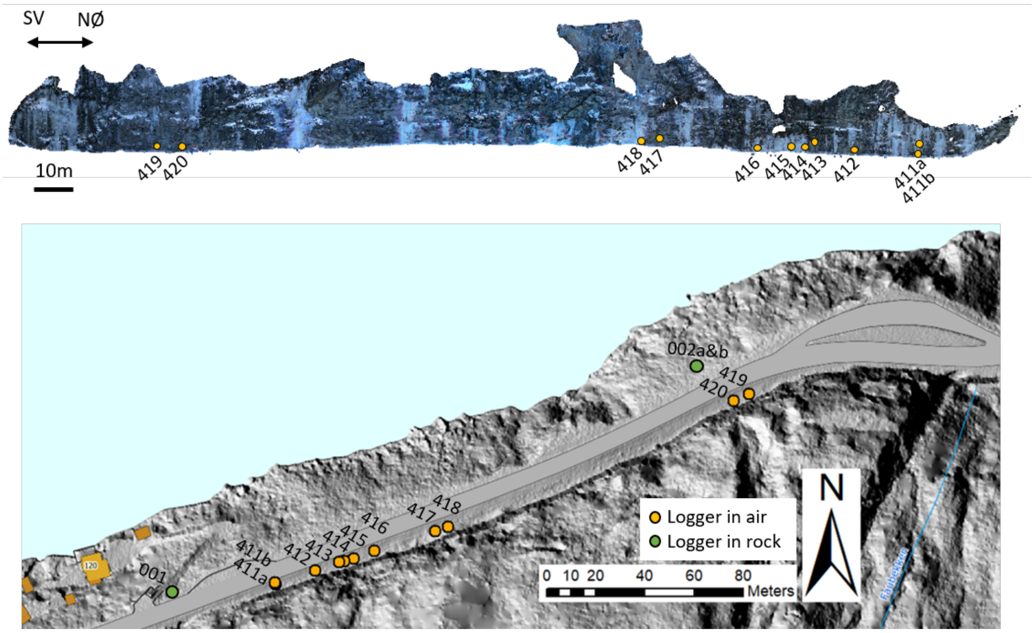

Figure 3.1: Upper: The position of each rock temperature logger as distributed throughout the rock cut. Lower: the position of each logger as positioned in a map. The loggers installed in rock are marked in yellow, while air temperature loggers are marked in green.

Figure 3.2: A) Installation of rock temperature loggers using a drill and silicone for sealing. B) Installation of radiation shield for air temperature loggers. The second box was installed in a lamp post. C) Photo of three loggers, encapsulated in rubber pockets and colored visible.

3.2 Temperature Analysis

In addition to providing information on the variation of temperature in the air and the rock, the data from the loggers were applied for studying the temperature differences between the study site and the temperature recorded at existing weather stations surrounding the study area. This provides an indication on whether one can apply the data from the weather stations alone for studying the ice growth, or if the temperature deviates significantly, necessitating local measurements. The basic statistics of the temperature series were investigated. The two loggers that were placed in the same radiation shield were used to study the precision of the temperature loggers, as these theoretically should provide equal results.

The closest available weather station to Trolla is Høvringen, situated approximately 2.4 km from the study area at an elevation of 44 masl. It records temperature, precipitation and wind, with the first records starting May 1st 2018. Weather stations at Sverresborg, Lade and Voll were also studied, as these have longer historical records allowing for estimating ice growth further back in time. Figure 3.3 shows the location of the four weather stations. Metadata for the stations is summarized in Table 3.2.

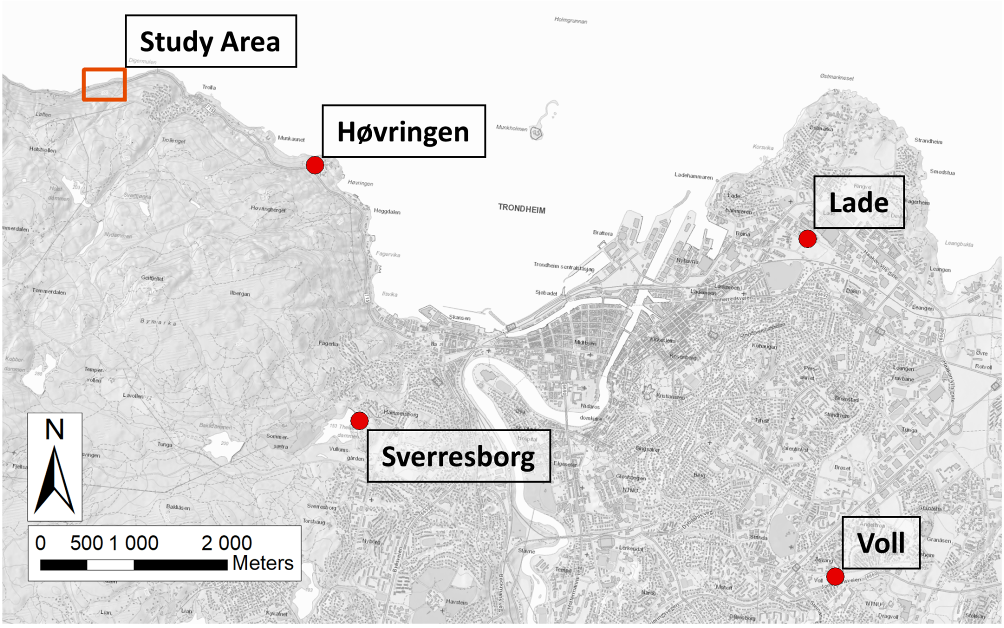

Figure 3.3: Map of the location of the four weather stations for which temperature data are compared to the study site temperature.

Table 3.2: Weather station metadata. The study site is situated at 22 masl.

Station	**Height [masl]**	**Distance to study area [km]**	**Records starting**	**Data types**
Høvringen	44	2.4	01.05.2018	Temperature, precipitation, wind
Sverresborg	156	4.5	01.01.2012	Temperature, precipitation, snow depth
Lade	13	7.7	01.02.2012	Temperature, precipitation, snow depth
Voll	127	9.4	01.01.1923	Temperature, precipitation, snow depth

For investigating the differences in recorded temperature, a paired T-test and a 2-sample T-test was performed. A T-test is a statistical hypothesis test used to determine whether there is a statistical difference in the mean values of two datasets. A paired T-test is applied for testing whether the mean difference between pairwise and dependent observations is equal to zero. In this context, the pairwise observations refer to the temperature recorded at the same time and place by two different loggers. In addition, a 2 sample T-test was applied for testing the mean differences between the data from the weather stations and the logger data. A 2-sample test is used when the data derives from different samples, which in this context refers to different locations, and different time of day of measurement.

For the two T-tests to be valid, the following assumptions must be met:
1) The data must be normally distributed. This assumption was confirmed by applying a normality test.
2) The data should be randomly sampled, in order to represent the population properly. This assumption is regarded as met as the temperature is recorded throughout the entire day.
3) The values must be continuous, and not discrete. This assumption is not fully met, as the iButton loggers seem to record discrete values. However, as the sample size is very large (2782 observations), the assumption may be ignored, as a consequence of the Central Limit Theorem.

In addition, two separate assumptions must be met for each of the tests. For the 2-sample T-test the assumption is that 4) the two groups of observations must be independent. The fourth assumption of the paired T-test is that 4) the observations must be related to two dependent groups creating pairwise observations.

The various statistical tests were performed using the statistical program Minitab (V. 18.1). Further details on statistical tests and validation of assumptions is described in Walpole et al. (2016).

3.3 Photogrammetry

The 3D temporal changes of the rockwall icing were registered by collecting sequential photogrammetry models during ice formation and decay. Section A, as marked in Figure 1.4, was photographed using a DSLR camera, while Section B was photographed using three action cameras mounted on a moving car. The main focus in the thesis is on section A, as DSLR photos were collected more frequently. The method of SfM-EV was applied mainly due to three reasons. Before this study was initiated, a photogrammetry model was collected by NGU in order to test equipment. It was collected by SfM-EV during the winter of 2018/2019. This was used for comparison to models collected in the 2019/2020 winter, providing valuable information on the annual ice changes. In addition, the method was attempted for applying as a tool to detect changes in the rock surface due to rock falls. Lastly, the method allows for much faster acquisition of large areas along roads, and it is thus valuable to investigate its applicability in comparison to the handheld DSLR generated models.

3.3.1 Acquisition Procedure and Settings

The applied DSLR camera was a Nikon D800, with 36.3 megapixels and a fixed 105mm f/1.4 lens. The acquisition was performed by photographing the section from several positions and angles along the rock wall, collecting photos covering the entire section at each position. The amount of camera stations varied from 5 to 17, with the majority being between 9 to 10 stations. As the study site is north facing, and the photos were collected mainly during winter/spring it was aimed to photograph the site during the hours of most light. The images were captured with a shutter speed of 1/400 to 1/600 seconds and ISO of 500 to 800, depending on the light conditions. A lower ISO and higher shutter speed generally produce better quality images and would have been preferable, but was necessary due to the low light conditions. The distance from the camera to the rockwall was approximately 10 meters. The first DSLR model, referred to as the reference model, was acquired the 3rd of October 2019, and the rock wall had no ice coverage at the time. During acquisition of the reference model, the position of each photo was registered with a dGPS connected to the camera, allowing for scaling and georeferencing of the point cloud.

Figure 3.4: The three Gopro cameras were mounted on a car, collecting photos every 0.5 seconds while driving at a speed of 15-20 km/h along the rock cut.

Section B (Figure 1.4) was photographed using three action cameras of the type GoPro Hero 7 Black, with automatic camera setting. The cameras have a 12 MP photo resolution, and vertical, horizontal and diagonal field of view of respectively 94.4°, 122.6°and 149.2°. Photos were acquired using the time lapse setting, collecting photos every 0.5 seconds, with GNSS registration. The three cameras were mounted on the roof of a car, while driving at around 15-20 km/h along the section. The middle camera was mounted facing directly towards the slope, while the two others at an angle of approximately 45°from the mid camera, as recommended by Voumard et al. (2018), photographed in Figure 3.4. The photos were collected at a distance of approximately 10 meters from the rock wall. The study area initially covered a stretch of approximately 1.2 km, which was later reduced to the area specified in Figure 1.4. This was in order to reduce the work related to processing and manual adjustments.

Two point clouds generated by respectively DSLR and action cameras are presented in Figure 3.5, illustrating the difference in camera stations between SfM and SfM-EV.

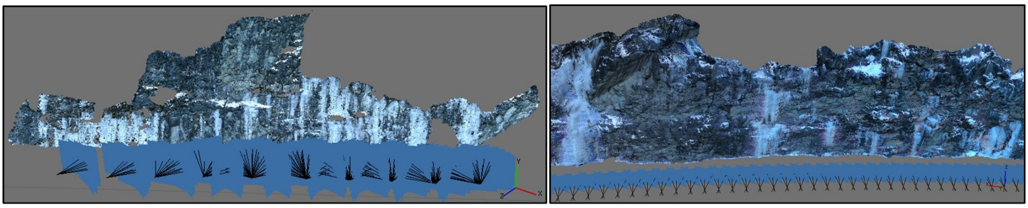

Figure 3.5: The left model is developed using the DSLR camera, applying the method of SfM, while the right model was developed using action cameras mounted on a car (SfM-EV). The tail of the blue squares represent the position of the cameras. The photo acquisition is different, with discrete camera position in the left model, and continuous collection using action cameras, illustrated in the right model.

3.3.2 Point Cloud Processing

Generating the point clouds was performed using the photogrammetric processing software Agisoft Metashape. Agisoft PhotoScan Professional (V.1.2.6) was used to edit the models, while Agisoft Metashape Professional (V. 1.5.5) was used to generate the sparse cloud and the dense cloud. The workflow consisted of the following five steps. Step 1 was only applied to the action cameras, while step 2-5 was performed for both the DSLR and the action cameras.

1. The images were split into groups based on the action camera it was collected by, allowing for exact camera calibration. Masks were applied to omit areas of the images where the car is visible in parts of the photo.
2. Alignment of the photos, developing a sparse dense cloud.
3. Optimizing the model by several methods, such as realigning wrongly aligned images, deleting uncertain tie points such as sky and vegetation, realigning or deleting images and/or tie points that contain few common projections or have a large pixel error.
4. When the photos are aligned correctly, a dense cloud of medium quality was generated.
5. Removal of vegetation and points of no interest from the dense cloud, such as the sky and the road.

3.3.3 Data Alignment

One DSLR model and one action camera model was collected on October 3rd 2019, before any ice had formed. These were used as the reference models, and all ice models were aligned and compared to these. The point cloud and mesh processing software CloudCompare (V.2.10.2) was applied for the purpose.

A mesh was calculated from the point clouds of the two ice free reference models, using a Delaunay 2.5D triangulation (best fit plane) in CloudCompare. The DSLR point clouds were reduced to 20 million points in order to reduce the memory requirements and processing times. The action camera clouds consisted of fewer points and were not reduced.

All models were further aligned and scaled to the respective reference mesh. The models were first correlated roughly using the tool «Point pairs picking» in CloudCompare, recognising equal features in the models. The scans were further aligned using the iterative closest point (ICP) algorithm. To base the alignment on only stable and common terrain, all ice was removed. This was achieved by filtering out the ice based on the red green blue (RGB) composite colors. The process is illustrated in Figure 3.6. In some models this proved slightly challenging, as there were only small contrasts in color between the rock and the ice.

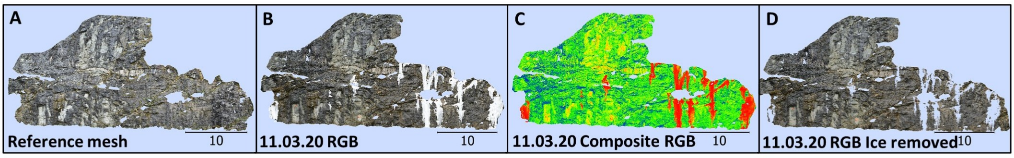

Figure 3.6: An overview of the alignment procedure of the DSLR models. A) Ice free reference mesh. All point clouds were aligned and compared to this mesh. B) A point cloud collected on the 11th of March 2020, partly covered by ice. C) The same model as in B, but converted to composite RGB colors. D) Ice removed based on color contrast. This model was aligned to the reference mesh, and the transformation matrix obtained from the alignment was applied on model B.

3.3.4 Investigation of Errors

To detect changes in the ice volume, the distance between the reference mesh and each point cloud was calculated with the «Cloud to mesh» (C2M) tool in CloudCompare. Part of the cloud to mesh distances are related to error, caused by inherent errors in the models, or by errors in the alignment of the models to the reference mesh. As the changes in ice thickness appears on a centimeter scale, it was important to investigate the accuracy and precision of the models.

As a reminder, the accuracy is closeness of the measured value to the true value, while precision is how close the measured values are to each other (Lane et al., 2000). For the purpose of this study, it is valuable to know the precision or reproducibility of the acquired models, and not necessarily the absolute accuracy. The precision of the SfM models were quantified by repeated measurements, comparing areas of the ice free rock face. This allows for obtaining the mean error (ME) and the standard deviation of error (SDE) by fitting a normal distribution curve to the obtained cloud to mesh distances of the rock surface, as indicated in Figure 3.7. The SDE can be used as a measure of the precision of each of the models (Voumard et al., 2018).

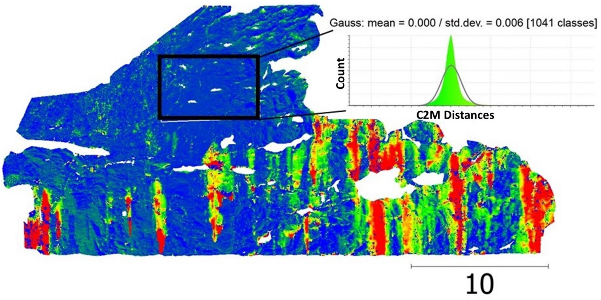

Figure 3.7: To quantify the errors in each model, the cloud to mesh distance was calculated on an ice free rock surface, assumed to only show cloud to mesh distances related to error. A normal distribution curve was fitted to the data, from which the mean and standard deviation of the errors (ME and SDE) were calculated.

For investigating the accuracy of the DSLR models, an ice free and an ice covered point cloud were compared to two corresponding LiDAR models, providing a rock-rock and ice-ice comparison of the two methods. Even though the LiDAR model cannot be regarded as the «absolute truth», the method is regarded as a slightly more accurate method, thus providing an indication of the accuracy of the photogrammetry models (Lato et al., 2015; Sturzenegger and Stead, 2009). A measure of the accuracy of the photogrammetry models was obtained by a similar approach as above, by calculating the overall ME and SDE of the cloud to mesh distances on the ice-ice and rock-rock models, where ME represents the accuracy and SDE is a measure of the scatter around ME. The acquisition procedure of the LiDAR models is reported in Section 3.4.

3.3.5 Volume Calculation

In order to calculate the total volume of the ice, the point clouds were exported as raster graphics for analysis in ArcMap (V.10.7.1). The pixel size was 0.01 m x 0.01 m , and pixels without information were interpolated. The ice volume was calculated by applying the «cut and fill» tool in ArcMap. As the majority of the ice formed in the lower part of the models, the area of calculation was reduced to a 283 m^2 area, as represented by the polygon in Figure 3.8. This avoids including unnecessary errors related to the ice free surface. The total volume was calculated by adding all positive volumes.

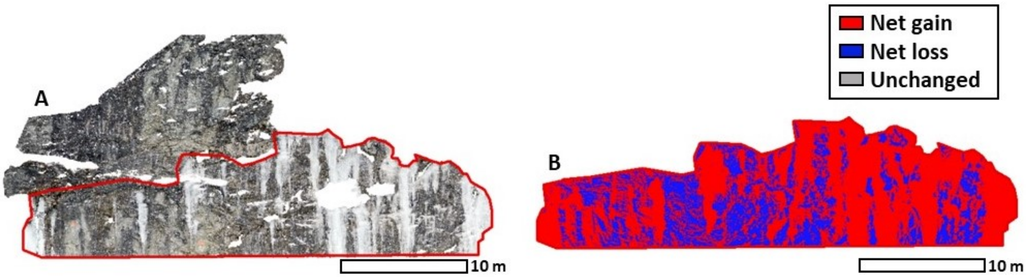

Figure 3.8: The volume change was calculated over an area of 283 m^2 by applying the cut and fill tool in ArcMap. The pixels containing no data were interpolated in CloudCompare. One of the models (04.03.2020) is shown in A, and the areas of positive increase, are assessed as areas of ice growth, shown in red in B.

3.4 LiDAR

As a tool to investigate the accuracy of the photogrammetry models, laser scans were collected using a terrestrial laser scanner (TLS). Comparing an ice free photogrammetry model to a corresponding LiDAR model will indicate the accuracy of the method itself. In addition, by repeating the procedure on two models containing ice will indicate whether introducing ice as a medium will impact the accuracy of the photogrammetry models. A comparison allows for detection of particular trends in deviation, and gives an indication of the reconstruction accuracy of the DSLR models.

3.4.1 Acquisition Procedure and Settings

The scans were performed using an Optech ILRIS-3D, as shown in Figure 3.9. It works at a minimum scanning distance of 3 m. The scan was performed at a distance of approximately 10-15 m, with the closest distance at the lower part of the rock wall.

Four scans were collected at four different days, from which only two are used in this study, as the other two scans showed to cover an area were the ice formation was at a minimum. Of the scan used, one was collected when there was no ice present (01.05.2020), while the other scan was collected during a day where ice had gathered (04.03.2020). Each scan consists of three partially overlapping scans, collected from three different positions. The scans were sampled with a point spacing of 7.5mm and set to register the last pulses arriving, reducing the pulses scattered from vegetation. At a distance of 15 meter, the diameter of the laser beam is approximately 9 mm on a perpendicular surface. The scanner is, according to the manufacturer, "specifically designed to scan ice, snow and wet surfaces with the same high accuracy and precision as other ILRIS models" (Optech, n.d.).

Figure 3.9: The Optech ILRIS-3D during acquisition of the ice free model.

3.4.2 Point Cloud Processing

The files obtained were transformed into a cartesian system using the software ILRIS Parser, provided by Optech. The scans were further processed using CloudCompare. Points of no interest and vegetation were removed from each scan, in addition to trimming the edges of the scans, as the result is generally poorer at the edges of the scans. The three individual scans from equal days were correlated by point to point picking, and the ICP tool, using one of the scans as a reference. This created one single point cloud with the same local reference system. Lastly, a mesh was created using a Delaunay 2.5D triangulation (best fit plane) in CloudCompare. Aligning the photogrammetry point clouds to the LiDAR models was performed in the same manner as described in Section 3.3.2.

3.5 Automated Camera

In order to obtain data on the continuous changes of the ice along Bynesveien, a camera of the type Canon EOS 600D SLR was mounted along the roadside in a tree. The camera was mounted inside a protective box, connected to a car battery and a solar panel, Figure 3.10 D. The camera collected photos every 10 minutes starting the 4th of February. It was de-mounted by the police the 7th of April as a suspected crime was discovered in the area, and the photos could be of help.

In addition to providing useful visual observations of the ice changes, the photos were also used quantitatively by mapping the boundaries of the ice, calculating the normalized area of the ice and comparing the ice boundaries of several days. A similar two dimensional approach was applied by Montagnat et al. (2010) and Bianchi (2004). The boundaries were mapped using the Color Tresholder tool in Matlab (V. R2019a). The tool allows for separating an image based on colors in the photo. It was used to separate the ice from the rock from which ice boundaries could be drawn. The workflow is visualized in Figure 3.11. From the original photo, a binary image was created based on the image colors, where ice is represented by 1 and the remaining image as 0. The image was then multiplied by a binary mask such that all areas of no interest were multiplied by 0, and the areas of interest were multiplied by 1. This excluded areas such as the snow covered road or vegetation. The sum of the remaining image represents the number of pixels inside the mask that is covered by ice, and the normalized area can be calculated as the ratio of pixels of ice to all pixels. The ice extent is visualized as lines representing the boundaries in the masked binary image.

Figure 3.10: The stationary camera shooting photos every ten minutes. On April 7th the camera was collected by the police due to an assumption of the camera having captured photos of a suspected crime that occurred in the area. To our knowledge the police discovered mostly icicles. Photo: Adresseavisen (2020a)

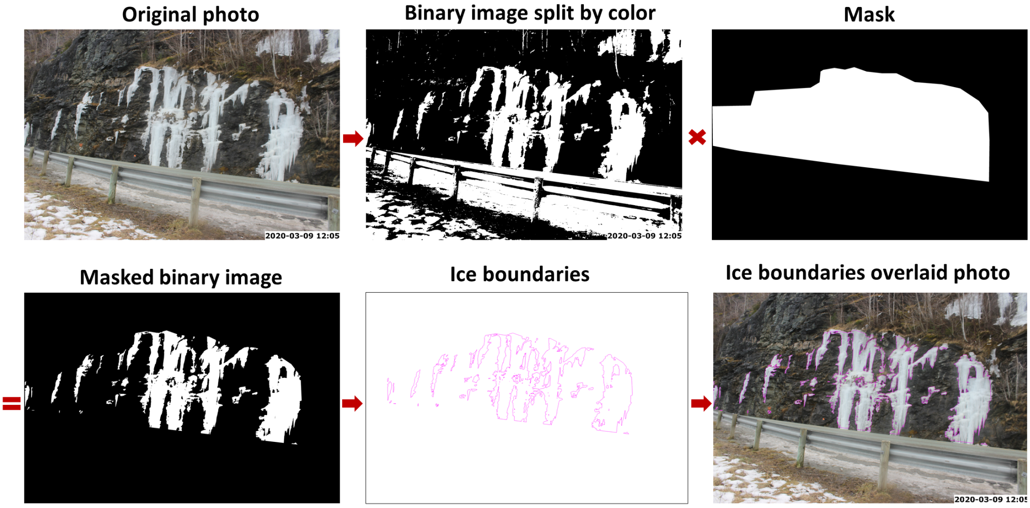

Figure 3.11: The figure presents the workflow that was applied to map the ice area in the images captures by the stationary camera. The original photo was split based on colors, such that ice is represented by 1 and the remaining photo as 0, resulting in a binary image. A polygon covering the area of interest was used to exclude other white parts of the image. This resulted in a masked binary image in which the boundaries represent the ice boundaries. The entire process was completed Matlab.

3.6 Detection of Rock Falls

During the autumn of 2019, geological field work was performed on the site, with the goal of recognizing the most probable failure mechanisms in terms of rock fall. The main findings are presented in Section 1.5 (Lilli, 2019). The geological field work consisted of measuring the orientation (dip and dip direction) of the various discontinuities and recording the general appearance of the structures, such as persistence, aperture, roughness and joint infilling. Based on the field work, a kinematic analysis was prepared recognising the most probable failure mechanisms.

Part of the intention of the study was to compare the rock cut before and after a winter, detecting rock falls occurring throughout the winter, and apply the results from the kinematic analysis as a tool. In order to detect rock falls, two photogrammetry models were collected, one before the winter (03.10.2019) and one after the winter (01.05.2020). These were processed and aligned using the same procedure as in Section 3.3. It did however prove difficult to detect changes based on the photogrammetry models. As a consequence, the detection of rock falls was mainly based on identifying rock blocks in the road shoulder that had appeared throughout the winter, comparing photos from before the winter.

Chapter 4

Results

4.1 Introduction

The winter of 2019/2020 consisted of mainly two relatively short periods of ice formation. The longest period occurred in November 2019, with negative temperatures lasting for approximately 11 days. The second longest period occurred in February/March 2020, with the main ice formation occurring in a period of about six days. Additionally, there were several smaller periods of minus degrees, but none that were of the character to initiate substantial ice growth.

At the initiation of the cold period in November 2019 no field equipment was yet deployed, as this was prior to the work of the thesis. One photogrammetry model was collected during this period, on the 11th of November. It was collected during the work of the specialization project (Lilli, 2019). During the cold period in February/March 2020, all field equipment was installed, and photogrammetry models were collected up to every day.

The following results are mainly based on data from the cold period in February/March. Additionally, the data that is available from November is presented. The results also include data on the winter of 2018/2019, as NGU collected one photogrammetry model in March 2019, allowing for a comparison between the two winters.

4.2 Temperature and Precipitation

This study has mainly focused on the temperature in relation to ice formation and decay, as temperature is the only meteorological parameter that was thoroughly measured throughout the period of study.

In the following sections the results from the air and rock temperature loggers are presented. Initially, the air temperature data are presented, and the precision of measurement is investigated. The temperature from the period of measurement is correlated to data from nearby weather stations. The correlation was used to infer the temperature for the periods where logger data does not exist. In addition, the correlation was also used to study the historical temperature records in relation to ice growth. The latter is presented in the discussion. Furthermore, the rock temperature data are presented and compared to the air temperature and periods of ice formation. Lastly, a brief comparison between the precipitation at the study area and a nearby weather station is presented, based on observations from the stationary camera.

4.2.1 Air Temperature Records at the Study Site

Figure 4.1 presents the data recorded by the three air temperature loggers. Logger 001 was deployed 14 days before logger 002a and b. The two latter were placed in equal locations, in order to investigate deviations due to logger equipment.

Table 4.1 summarizes the basic statistics of the three air loggers, between the 12th of December and the 6th of April, as this is the common period in which all were recording. During this period, the loggers 002a and 002b show a mean temperature of 3.3 and 2.7°C, respectively. A paired T-test shows that the two loggers record statistically significant different results. The estimated true difference is 0.6 ±0.1 (95% confidence interval). Even though the pairwise differences are within the accuracy specified by the manufacturer of ±0.5°C, the mean should theoretically scatter around an equal value. As both loggers were situated in the same radiation box, the measured differences must be related to the logger error. The logger 001, situated at a distance of 230 m away from 002a and b show a smaller deviation in mean temperature from the two loggers, of -0,2 and +0,4 °C, respectively. The temperature variation between the two sites is thus within the logger accuracy and is not detectable.

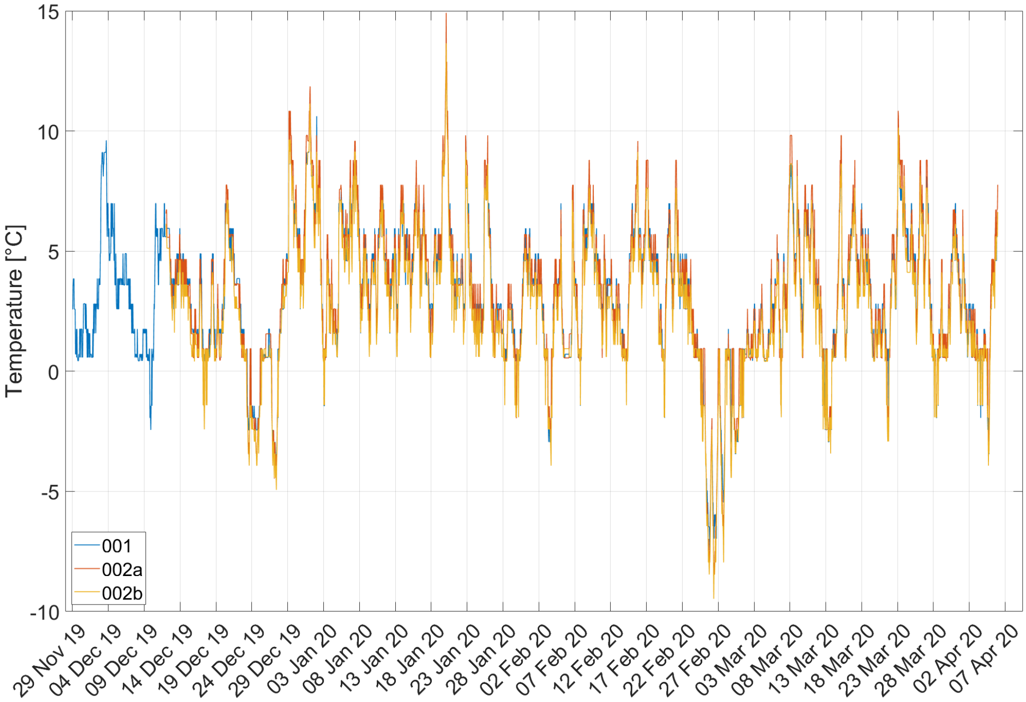

Figure 4.1: The air temperature as recorded by the three loggers, with recording interval of one hour. Logger 001 was installed 14 days before 002a and b. Logger 002a and 002b were placed in the same radiation box, while logger 001 was placed 230 meters northwest of the two.

Table 4.1: Mean, standard deviation (SD), minimum and maximum temperature as recorded by the three air temperature loggers, recorded between 12.12.2020 and 06.04.2020.

Logger ID	Mean Temp.	SD	Min. Temp.	Max. Temp.
001	3.1	2.9	-7.5	13.7
002a	3.3	3.0	-9.0	14.9
002b	2.7	2.9	-9.5	13.7

4.2.2 Temperature Correlated to Existing Weather Stations

Figure 4.2 plots the hourly mean of the three air temperature loggers at the study site, with the temperatures recorded at the four weather stations Høvringen, Voll, Sverresborg and Lade, during the same period.

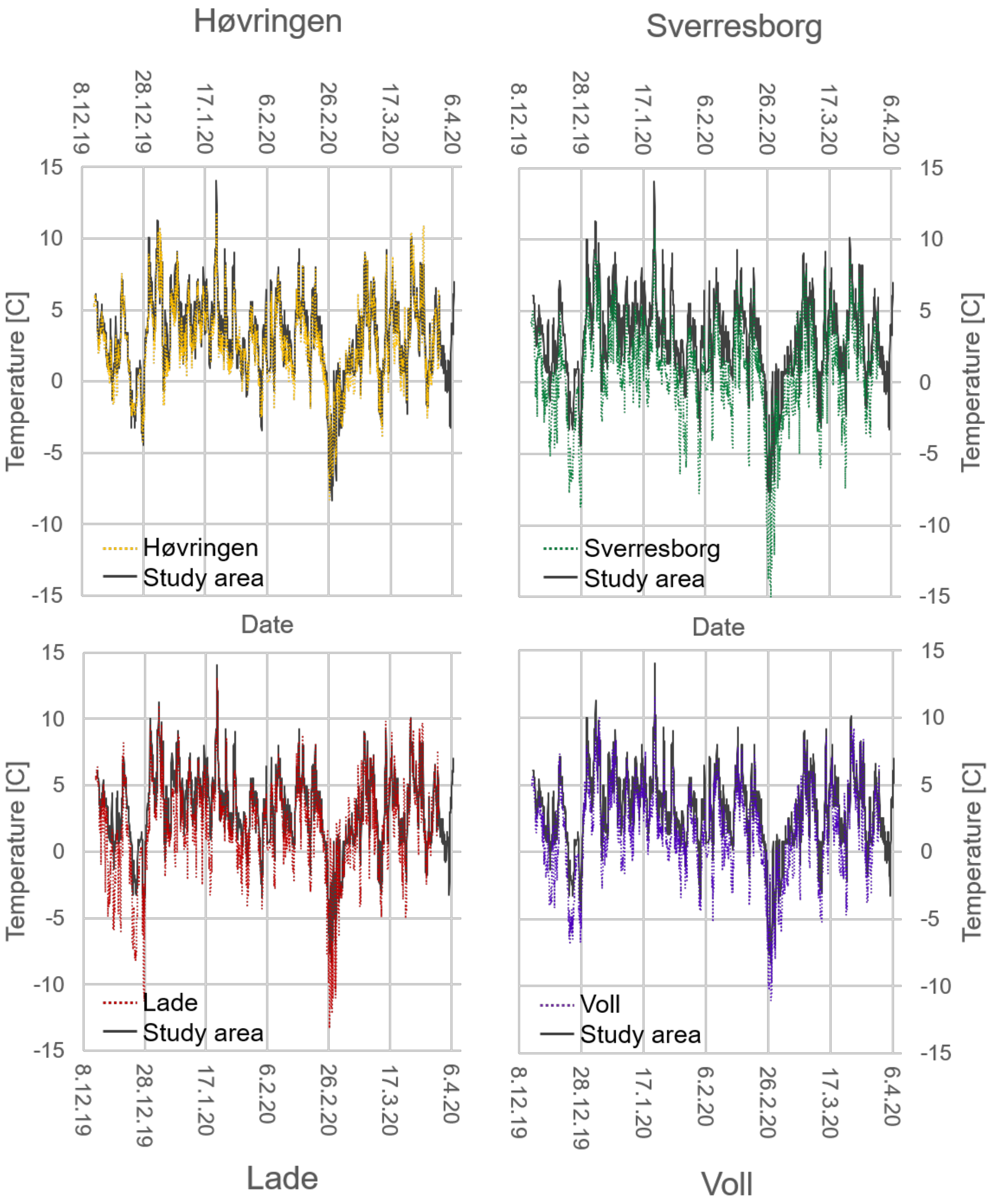

Figure 4.2: The hourly mean temperature of logger 001, 002a and 002b is plotted together with temperature data of four weather stations in Trondheim. The grey line represent the study site temperature, while the colored graphs are the temperature recorded at the weather stations. The trends and variation in temperature throughout the period is similar for all weather stations, but the study site temperature is generally above the temperature at the nearby weather stations.

A 2 sample T-test was performed, comparing the data from the weather stations to the logger data. Due to the deviation between the loggers, the data was compared to all loggers individually. Table 4.2 reports the difference between the mean temperature recorded by the weather stations and the mean temperature of the individual loggers. The result is listed as an interval, as comparing the weather stations to different loggers give an interval of 0.7°C, with logger 002b giving the lowest difference and 022a the highest, while 001 is in between. The 2 sample T-test showed that the mean temperatures recorded at Høvringen cannot be said to be statistically different from logger 002b (P-value = 0.105), while comparing the data to logger 001 and 002a, Høvringen records a lower temperature, with 95% confidence. The mean difference between Høvringen and the loggers varies between 0.1°C (logger 002b) and up to 0.8°C (logger 002a). As expected, the weather stations situated further away, give larger mean differences.

As the difference between the means is only a measure of the population as a whole and does not compare pairwise temperature observations, the latter is given in the three last columns in Table 4.2. The table summarizes the percentage of weather station observations that are more than -0.5°C below the study site temperature at equal times, above 0.5 °C and between -0.5 and 0.5°C. In these columns the study site temperature is calculated as the mean of logger 001, 002a and 002b, at equal times. The iButton loggers record temperature every hour at hh:47, while the weather stations record temperature every hour at hh:00, resulting in a shift of 13 minutes. This will contribute to a slight increase in error.

Table 4.2: The difference in mean temperature between the weather station and the individual loggers is calculated as the mean of the weather station data, minus the mean of the individual logger data, throughout the period of measurement. The difference is presented as an interval as it depends on which logger the data are compared to. Logger 002b gives the lowest difference, while logger 002a reports the highest difference. The three end columns show how the temperature differences distributes, and is calculated as $T_{\text{weather station}} - T_{\text{mean(001,002a,002b)}}$, given as a percentage of the total records.

Station	Mean difference (002a, 002b)	<-0.5°C [%]	≤-0.5,0.5≥ [%]	>0.5 [%]
Høvringen	(-0.8, -0.1)	51,4	38,1	10,4
Voll	(-1.8, -1.1)	83,5	11,0	5,4
Sverresborg	(-2.7, -2.1)	95,4	3,0	1,6
Lade	(-1.4, -0.7)	60,9	31,5	7,6

Lastly, it was attempted to obtain a simple correlation between the temperature at the weather stations and the logger temperatures. Figure 4.3 plots the study site temperature along the x-axis, and the weather station temperature along the y-axis, at corresponding hours. A linear line of best fit is drawn for each dataset, and its equation and the coefficient of correlation, R^2 is given in equation 4.1 to 4.4. An R^2 value of 1 represents a perfect correlation between the data points and the line, while 0 represents no statistical correlation. The mentioned shift of 13 minutes in time of recording will also impact slightly on the correlation.

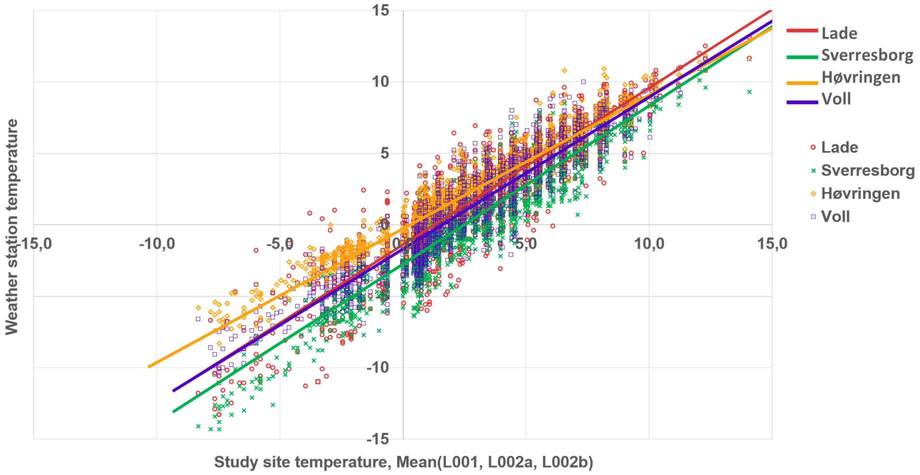

Figure 4.3: Temperature records from the four weather stations Høvringen, Lade, Sverresborg and Voll are plotted against the air temperature recorded at the study site. A line of best fit is added for each dataset. Høvringen weather station has the best fit with the study area with an R^2 of 0.92.

$$\text{Høvringen} \quad y = 0.94x - 0.29, R^2 = 0.92 \tag{4.1}$$

$$\text{Lade} \quad y = 1.10x - 1.40, R^2 = 0.82 \tag{4.2}$$

$$\text{Sverresborg} \quad y = 1.11x - 2.75, R^2 = 0.88 \tag{4.3}$$

$$\text{Voll} \quad y = 1.06x - 1.70, R^2 = 0.87 \tag{4.4}$$

Høvringen is the weather station of best correspondence, with an average temperature deviation from the study site of -0.1 to 0.8°C and an R^2 of 0.92. The good correspondence is rather expected, as it is close in distance, have a similar height above the sea, and is situated by the fiord. The records are however limited, dating back to mid 2018.

All weather stations record temperatures lower than the study site temperature, to various extent. This is expected, as most of the stations are either at higher elevations, or situated further inland, thus being less impacted by the fiord temperature. The general trends in temperature are similar, and the periods of persistent cold weather where ice is formed is evident in all graphs in Figure 4.2. All but Høvringen do however show cold periods that are generally colder and slightly longer than what is measured at the study site. Predicting ice growth using data from these stations may thus lead to a slight over estimation of ice volume. In addition, Sverresborg, Lade and Voll have more frequent periods of negative degrees compared to the logger temperature. The R^2 value is relatively high for all graphs, and by applying the linear correlation listed in Figure 4.3 one may obtain an improved estimate of the study site temperature. This also allows for back calculating the study site temperature to March and November 2019 where data on ice volume is available but loggers were not yet installed. This was done using data from Høvringen, due to the close correlation. The graphs are presented in the following section.

Lastly, it must be noted that the data comparison is only based on a limited period of four months during 2019/2020. Trends may change over years, and may not necessarily be representative for every year. It does however give an adequate indication of the general temperature trends.

4.2.3 Air Temperature and FDH During the Periods of Ice Formation

In Figure 4.4 the temperature and the corresponding freezing degree hours (FDH), as was presented in Equation 2.1, are plotted for the three periods in which data on ice volume exists. The linear relationship between the air temperature at the study site and temperature data at Høvringen weather station, Equation 4.1, is used to plot the temperature for the periods in March 2019 and November 2019. The FDH increases with negative temperatures, and decreases with positive temperatures, with 0 being the minimum value. The parameter can be used as a measure of the "severity" of each cold period, where the severity refers to how cold and how long each cold period is (Assel, 2003).

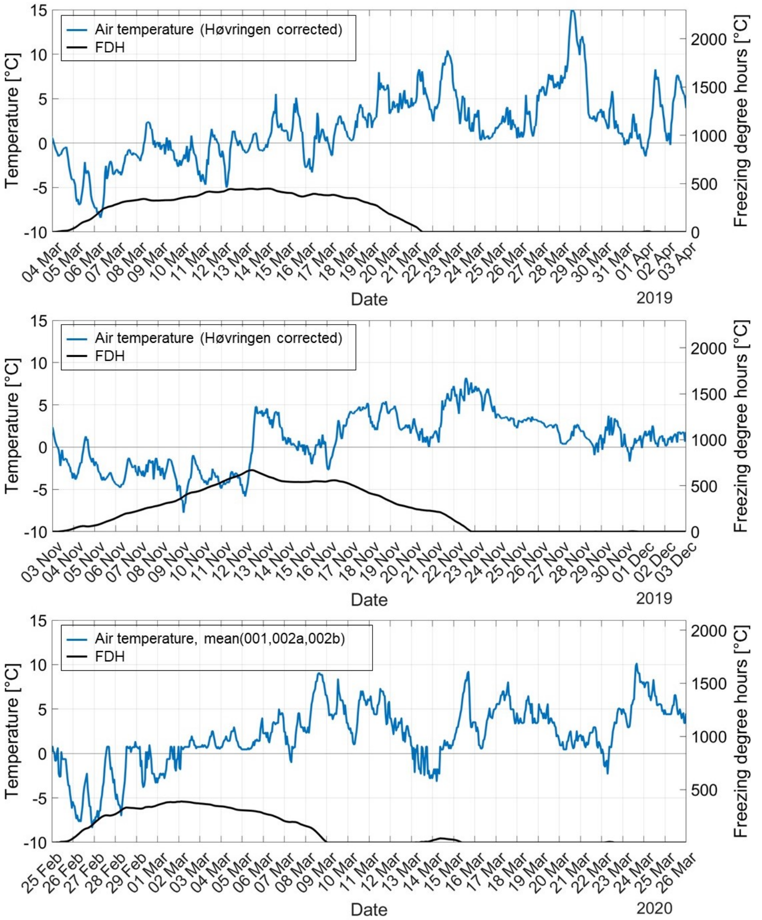

Figure 4.4: The temperature of each period in which data on ice volume exists is plotted in blue. The black line corresponds to the FDH, which is a measure of the cumulative negative degrees throughout a cold period.

4.2.4 Precipitation

As precipitation is visible on the stationary camera, it was possible to compare the days of precipitation at the study site to the recorded precipitation at Høvringen. A simple comparison is presented in Figure 4.5, with days of observed precipitation marked in red and cyan, and precipitation recorded at Høvringen plotted as bars. It is apparent that the precipitation during the period of February 25th to March 25th was relatively local, as the days of precipitation do not directly correspond.

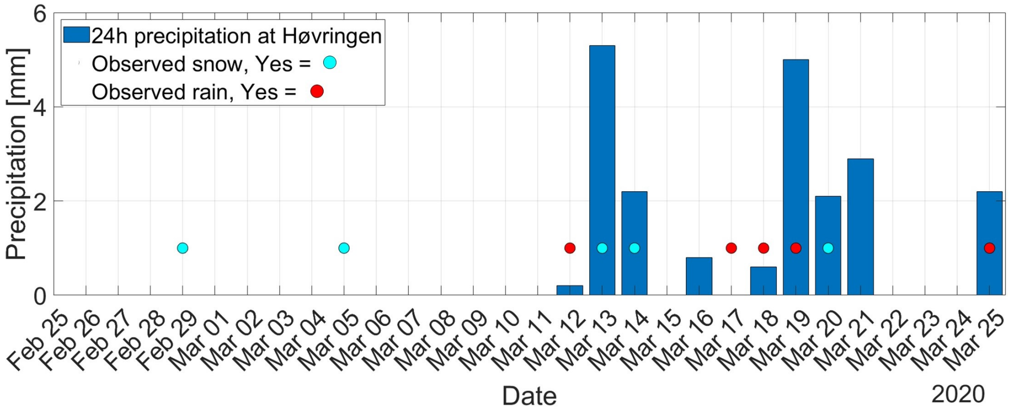

Figure 4.5: Precipitation recorded at Høvringen weather station is plotted in blue bars, reported as the accumulated daily precipitation. The circles represent days in which precipitation was observed at the study site. The cyan dots represent the days of snow, while red circles represent days of rain. The precipitation was only visually observed through photos, and the amount is thus not recorded.

4.2.5 Rock Temperature

A total of 11 temperature loggers were installed into the rock. Of these, logger 411a, 415 and 419 showed to have a defect and had not recorded any data. These loggers were all covered by ice and were visible in the frame of the stationary camera, thus resulting in loss of important data. Of the 8 functioning loggers, three were covered by ice, from which one was visible in the frame of the stationary camera. Table 4.3 provides details and basic statistics on all loggers, including the air temperature loggers, for comparison. The daily temperature mean for all loggers are plotted in Figure 4.6. The temperatures are plotted as means for readability. Appendix C list all graphs with the original sampling rate of 1 hour.

Table 4.3: Overview of the temperature loggers and basic statistics. The numbers are calculated between 12.12.2019 and 02.04.2020, which is the common recording period for all loggers.

Logger ID	Medium	Ice cover	Mean	SD	Min	Max
001	Air	-	3.2	2.9	-7.5	13.6
002a	Air	-	3.3	3.0	-9.0	14.9
002b	Air	-	2.7	2.9	-9.5	13.7
411b	Rock	28.02-09.03	1.5	1.5	-5.5	7.9
412	Rock		1.6	1.7	-5.7	7.9
413	Rock		2.0	1.5	-4.4	7.1
414	Rock		1.3	1.7	-5.5	8.1
416	Rock	29.02-22.03	1.4	1.2	0.5	7.9
417	Rock		1.5	1.6	-5.2	7.7
418	Rock	29.02-at least 05.03	1.5	1.7	-5.5	7.8
420	Rock		1.6	1.5	-5.0	6.8

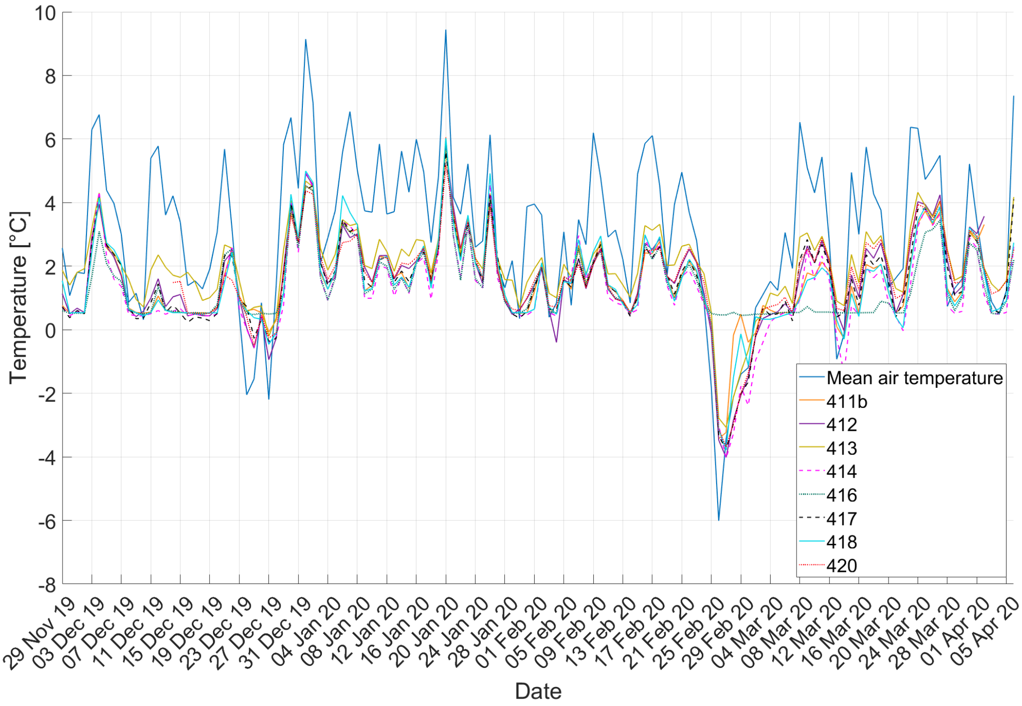

Figure 4.6: The figure plots the daily mean temperature as recorded by the eight rock temperature loggers. The daily mean air temperature is plotted in blue, for comparison.

Logger 413 quite consistently records the highest rock temperatures, with a mean temperature of

2°C. The mean temperature of the remaining loggers calculates to between 1.3 to 1.6°C, and do not show distinct trends in being significantly higher or lower than the others. Logger 413 was installed in a massive granodioritic rock, while most of the other loggers were installed in the green schist, that generally has a higher joint frequency. Logger 416 stands out, as it never during the logging period records temperatures below 0°C. All the remaining loggers measure minimum temperatures of around -5°C. 416 is tested in a freezing environment, correctly measuring negative degrees, such that one can not suggest that this is due to a defect.

Figure 4.7 shows the same data as in Figure 4.6, but limited to the period where the rock wall had ice attached, and plotted with hourly temperature values, corresponding to the logging interval. In addition, the time span in which the three loggers 411b, 416 and 418 were covered by ice is visualized.

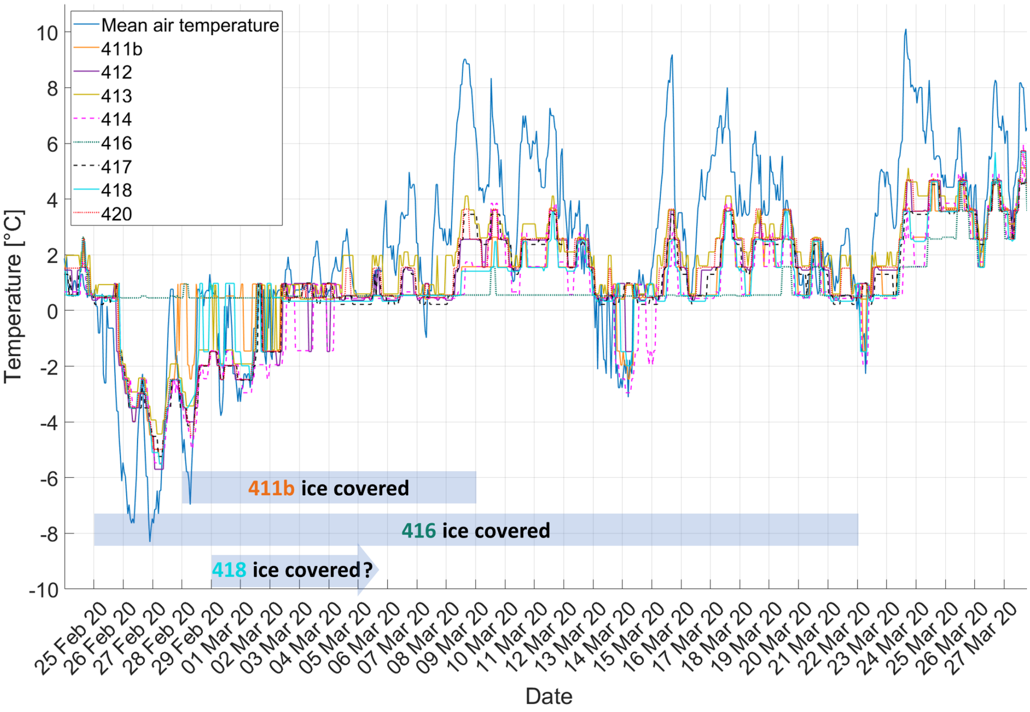

Figure 4.7: The graph plots the hourly rock temperature between February 25th to March 27th 2020, in addition to the air temperature, for reference. Logger 411b, 416 and 418 were installed in an area where the rock cut got covered by ice. The duration of the ice coverage for each logger is illustrated by blue squares.

Logger 416 was instantaneously covered by ice when the air temperature dropped below zero during the 25th of February. The ice covering this logger kept stable for a long time, and did not disappear completely until around the 22nd of March. The exact uncovering is slightly uncertain, as photos show a column of ice covering the logger, but it is not possible to determine whether there is a void between the ice and the rock at some point. Throughout the entire period where the logger is ice covered, the logger have records deviating significantly from the other loggers, quite consistently measuring 0.6°C. On the 23rd of March this trend changes, and the logger starts recording temperatures equal to the other loggers. This corresponds more or less to the time at which the ice cover disappears.

Logger 411b and 418 were covered by ice on respectively the 28th and the 29th of February. Both loggers record an increase in temperature soon after they get covered by ice. The temperature is raised to 1°C, but both loggers record fluctuating temperatures, varying between +1°C and -2°C for approximately 4-5 days. On the 2nd of March the temperature stabilizes around 1°C. This corresponds to when the air temperature crosses above 0°C. The stable rock temperature lasts until the 8th, when the temperature of both 411b and 418 raise simultaneously, and return to coinciding with the temperature of the uncovered loggers.

On the 8th of March the ice cover of logger 411b was very thin, and on the 9th the ice was completely melted in this area. The duration of the ice coverage on logger 418 was not recorded for longer than the 5th of March, when it had a thin cover of ice. From the behaviour of the temperature one may assume that the ice cover duration was similar to that of logger 411b.

4.3 Ice Growth and Decay

In the following chapters the results from the various methods of surveying ice growth along Bynesveien are presented. The photos from the stationary camera provides a visual overview of the ice evolution in February and March. From these, the area of the ice is calculated based on color recognition, which can be used as a 2D proxy for the ice volume. Furthermore, the results from the photogrammetry models are presented. The models created from the DSLR photos are used for detecting the temporal changes during the cold period in February/March 2020, and for comparing the ice quantity to that of November 2019. The SfM-EV processed models provide a comparison of the annual changes in ice quantity, by including a model collected in March 2019. Lastly, the results of the LiDAR scan are presented, comparing the scans to two corresponding DSLR photogrammetry models as a tool to estimate the accuracy of the photogrammetry models.

4.3.1 Stationary Camera Observations

The stationary camera was installed in order to obtain a more continuous overview of the ice changes. Photos captured every 10 minutes allow for noticing changes in the ice with a high level of detail. The camera was installed on February 4th, and covered the last period of ice formation, which was initiated on the 25th of February.

Following is a series of photos from the mentioned period, presented in Figure 4.8, 4.9, 4.10 and 4.11. The ice coverage was mapped out with the method described in Section 4.3.1 to show the variation in areal extent. Days with snow coverage or thin ice coverage were difficult to map based on color. These are either presented, as in Figure 4.8, or are described. All photos presented are captured at 5 minutes past 12. Figure 4.9, 4.10 and 4.11 illustrate the ice change occurring over 2-5 consecutive days. Each figure consist of a photo from a particular day, with the ice extent of the succeeding days mapped out in colors.

The main period of temperatures below 0°C, between the 25th of February to the 1st of March, was the predominant period of ice formation. Following these days the temperature increased to above zero. Until the 8th of March, the reduction in ice extent occurred mainly by melting, and no significant ice falls were observed. On the 8th the temperature increased up to 9°C and several smaller ice falls occurred. Following the 8th the ice reduction appeared as a combination of melting and smaller ice falls. The largest observed ice falls were on the 12th and the 18th of March where significant sections of ice are detached. Ice falls are marked by arrows in the figures. On the 25th of March, the majority of the ice is melted or has fallen down. A more detailed description of the ice evolution is given in the figure text.

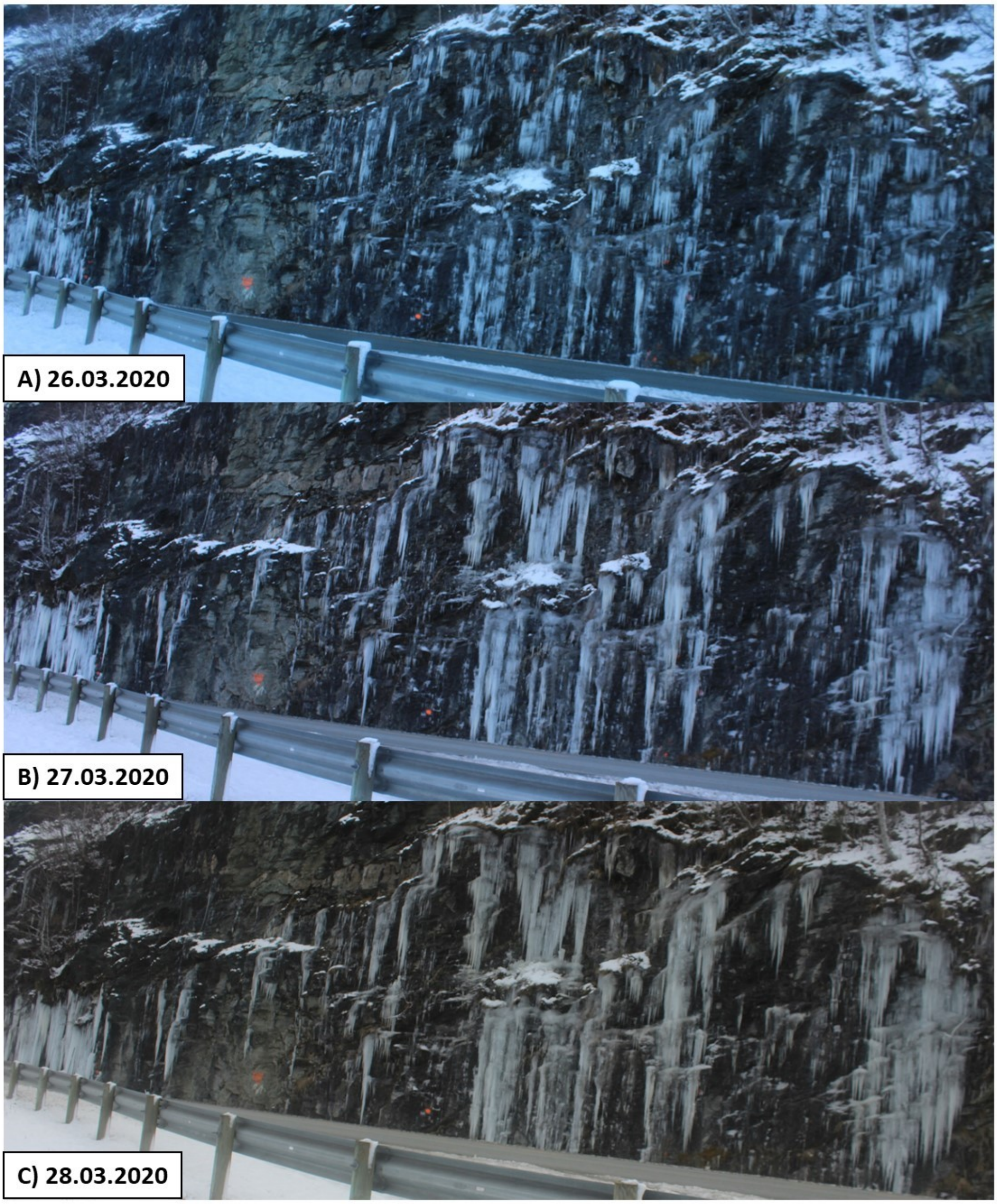

Figure 4.8: Temperatures dropped below 0°C on February 25th, with ice starting to form rapidly after. Figure A, B and C show the progress during the 26th, 27th and 28th. The initial growth consists of the formation of a thin ice crust on the rock, and icicles extending continuously. On the 28th some icicles have reached the ground and have started forming ice columns. The boundaries of the ice was mapped by color recognition on the 28th. The previous days the color contrast of the ice and the rock was not suitable for mapping.

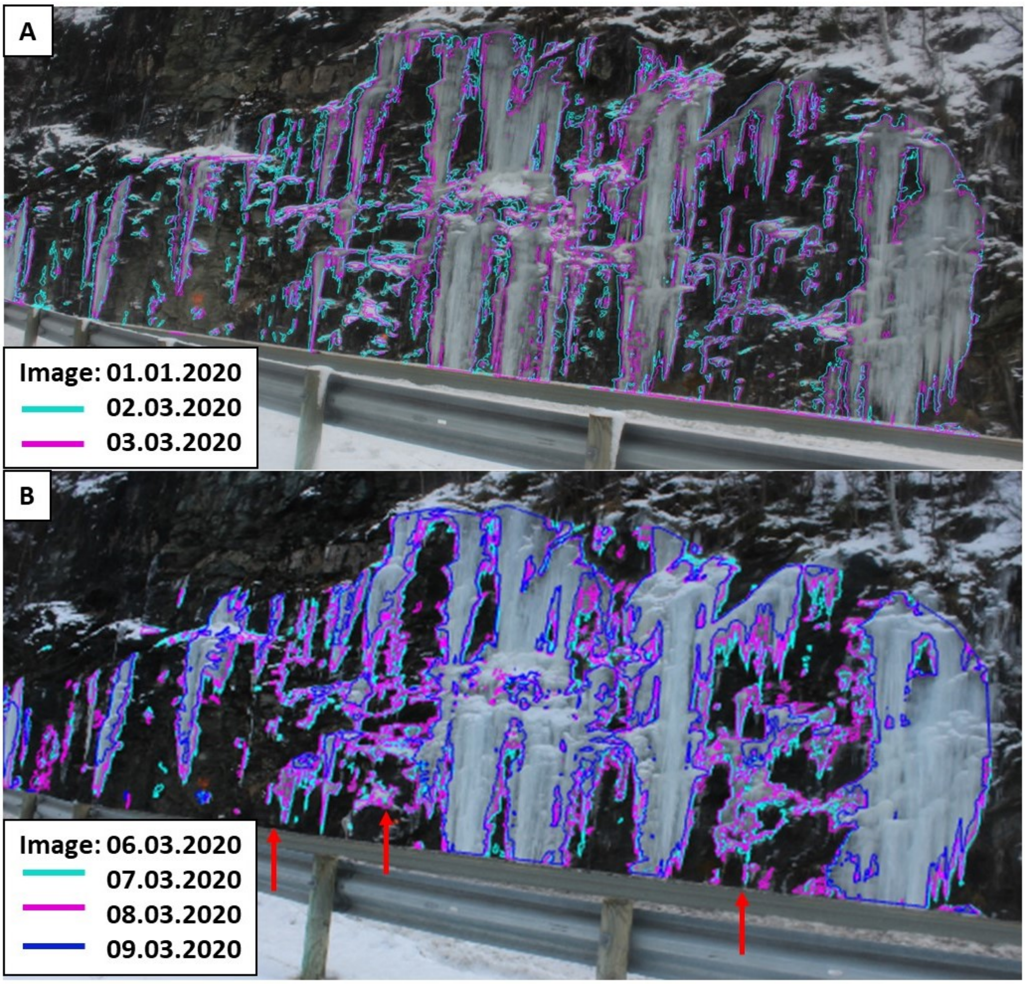

Figure 4.9:
A) 1st of March is the background photo. The ice extent the 2nd and 3rd of March is overlain. The ice extent was slightly reduced during these days, mainly by melting. No significant ice falls were observed. On the 5th there was a snow fall, covering the wall such that the ice extent could not be mapped.
B) A photo from the 6th of March is overlain by the mapped ice extent the 7th, 8th and 9th of March. Until the 8th the ice was reduced mainly by melting. During the 8th and 9th the temperature increased to 9°C, and the melting accelerated. In addition, several smaller ice falls occurred, marked by red arrows. It is mainly the thinner sections of ice that are subject to ice fall.

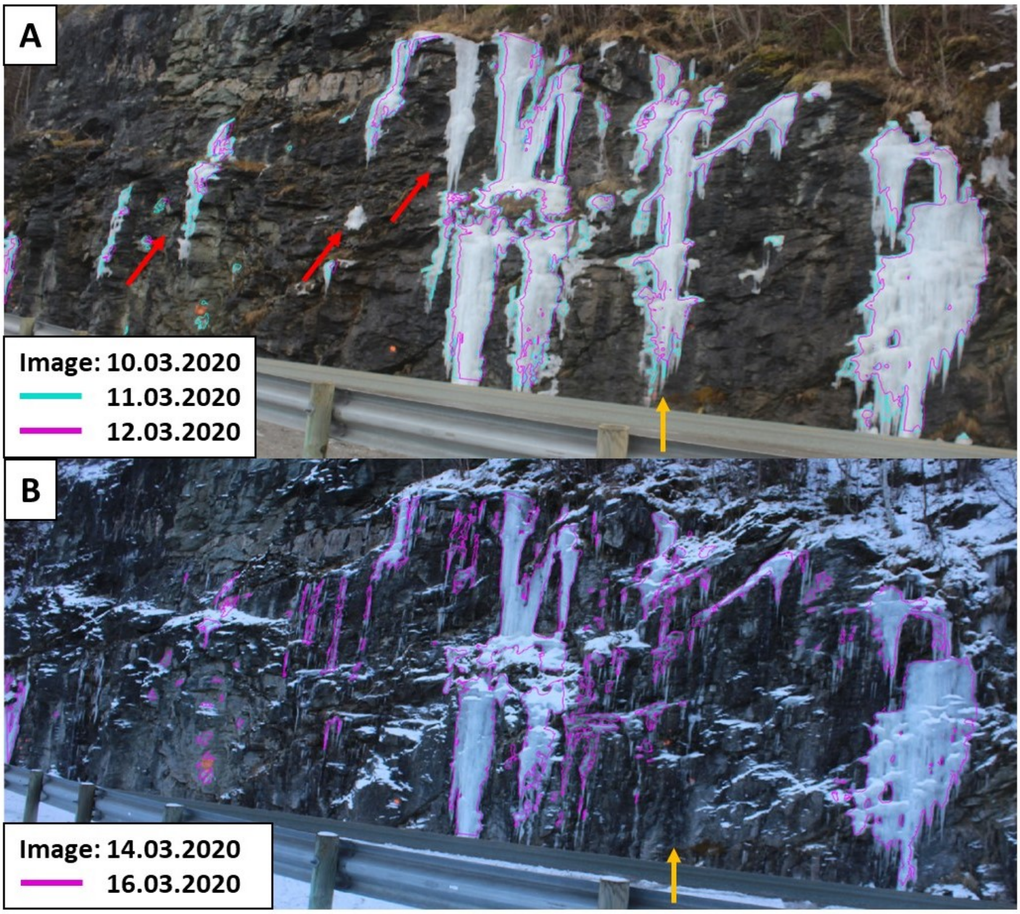

Figure 4.10:
A) The ice extent of 11th and 12th of March is drawn on top of an image from the 10th of March. The development is similar to the previous days, with ice continuing to melt and smaller ice chunks collapsing, marked by red arrows. On the night between the 12th and 13th a larger column of ice collapsed, as still visible in the middle right in photo A, detached in photo B, marked by a yellow arrow.
B) On the 13th a snow fall occurred covering parts of the rock cut. During the 13th and 14th of March the temperature dropped below 0°C again, initiating minor icicle growth, and creating a thin ice crust on parts of the rock cut. With a temperature rise the 15th, the ice that was formed melted quickly again, and the larger columns continued to thin.

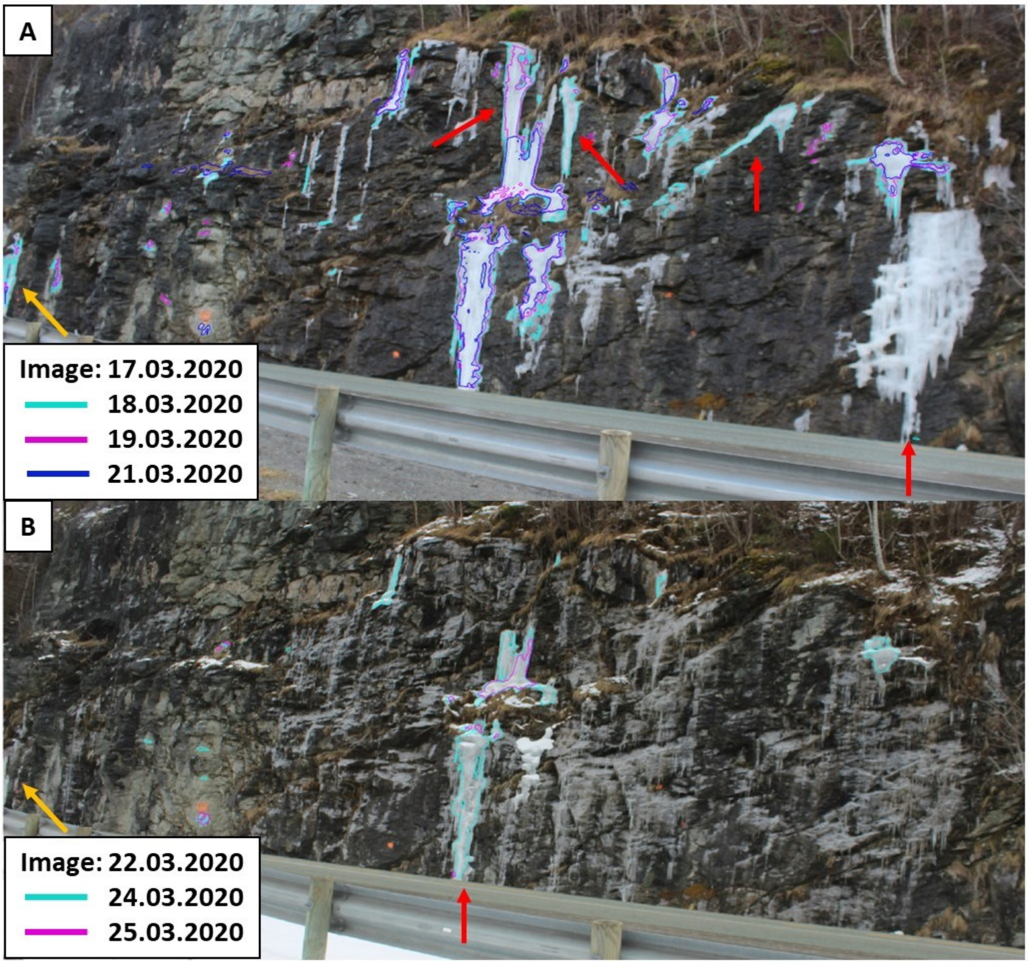

Figure 4.11:
A) On the 17th there were several smaller ice falls. On the morning of the 18th the leftmost ice section collapsed, marked in yellow. At this point the majority of the ice is melted or collapsed.
B) Five hours of negative temperatures on the night of the 22nd quickly created an ice crust on the rock. After 1.5 days of positive temperatures, the crust again was completely melted. The remaining ice column collapsed on the 24th leaving only a minor part of ice left.

Lastly, the normalized area of the ice, given as the ratio of number of pixels representing ice to total pixels in the photos was calculated for each photo. Figure 4.12 presents the daily changes with the corresponding air temperature, as recorded by the temperature loggers. The area of the ice provides a value based on the 2D evolution of the ice and is investigated as an alternative method for calculating the ice changes.

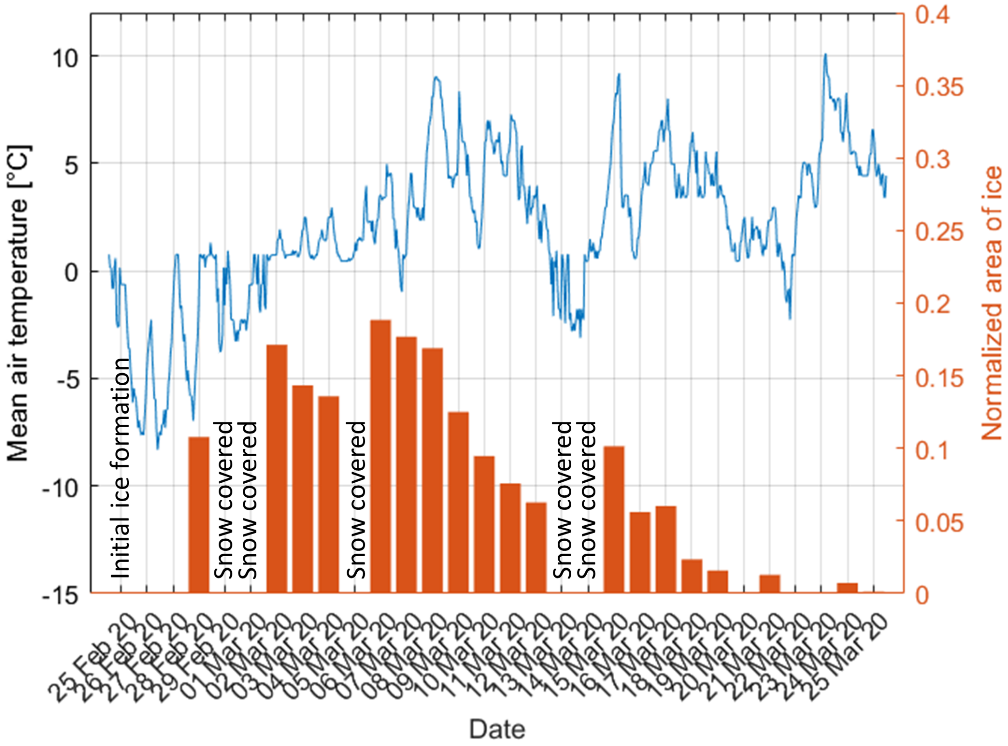

Figure 4.12: The bars represent the normalized area of the ice, based on the photos captured by the stationary camera. The blue graph represents the air temperature as recorded by the temperature loggers. On the days where the rock cut was snow covered it was not possible to obtain a value of the area, due to poor color recognition.

4.3.2 Ice Evolution as Detected by Structure from Motion

Overview of the Photogrammetry Models

A total of 15 SfM models were collected with the DSLR camera, of which 13 are presented in the thesis. These include two ice free models, which were collected on October 3rd and May 1st. The first was used as the reference model, and all the following ice covered SfM models were aligned to this. The latter was used to compare to a LiDAR scan for investigation of the accuracy of the SfM. The remaining models were collected during ice coverage. One model was collected in November (11.11.19), during the first period of significant ice formation, as part of the specialization report (Lilli, 2019). Two models were collected in the month change of January/February. On those days only a very minor ice cover had formed, and did not provide satisfactory data on neither ice volume evolution, nor on ice fall occurrence. These two models are not included in the thesis. Finally, in late February and March the temperature decreased, and a sequential time series of photogrammetry models were collected. During this period, models were gathered up to every day. On the 5th of March, two models were collected, one during the morning and one in the afternoon. All models are presented in Appendix C.

Table 4.4 lists all 13 photogrammetry models. Approximately 250 photos were used for generating each model. Throughout the study period, the amount of stations and the image overlap were more standardized. The point density refers to the amount of points per m^2 in each point cloud, while the mean reprojection error is a measure of the accuracy of the position of the tie points in the sparse point cloud, providing an indication of the reconstruction quality of the clouds.

Table 4.4: List of the 13 SfM models, collected by a DSLR camera. (1)Number of images used in the model / Total number of images. (2)Point density in a search radius of 0.01m, obtained in CloudCompare. (3)The reprojection error is reported by the Agisoft software, and is the root mean square error of x,y and z averaged over all tie points in the sparse cloud. It is a measure of the accuracy of the tie points in the point cloud.

Acquisition Date	**Stations**	(1)**Images**	**Points in point cloud**	(2)**Point density [$m^{2^{-1}}$]**	(3)**Mean reprojection error [pix]**
03.10.2019	17	379 / 429	19 546 031	32 093	1.17
11.11.2019	5	378 / 378	16 268 660	30 099	1.17
29.02.2020	8	572 / 603	18 777 082	40 879	0.54
03.03.2020	10	288 / 293	15 779 950	27 120	0.51
04.03.2020	10	281 / 292	17 251 152	28 850	0.56
05.03.2020 (10:30)	10	262 / 263	17 796 265	28 940	0.64
05.03.2020 (17:30)	10	242 / 249	19 946 611	40 879	0.44
06.03.2020	10	258 / 254	18 713 135	30 943	0.74
07.03.2020	10	244 / 226	20 000 000	39 315	0.49
09.03.2020	9	215 / 233	18 658 976	31 787	0.54
11.03.2020	9	264 / 272	18 530 274	33 303	0.46
16.03.2020	9	242 / 249	18 329 994	31 773	0.44
01.05.2020	9	262 / 262	2 716 031	33 043	0.39

Investigation of Precision

After aligning all point clouds to the reference model, the ME and SDE of the cloud to mesh distances on an ice free surface of the point clouds were calculated as a mean to evaluate the quality of the models, as described in Section 3.3.4 and Figure 3.7. A low ME and SDE is indicative of a high precision. The values for each point cloud are listed in Table 4.5. ME vary between -4 mm to +5 mm, with the majority of the models being around 1 mm. The SDE vary between 5 mm and up to 3 cm. In particular four models show slightly larger errors. These are the three first models, and the model collected on the morning of 05.03.

Table 4.5: The table lists the mean error and standard deviation of error of each model, calculated on an ice free rock surface.

Aquisition Date	ME [m]	SDE [m]
11.11.2019	0.005	0.018
29.02.2020	-0.004	0.030
03.03.2020	0.004	0.015
04.03.2020	0.000	0.006
05.03.2020 (1)	0.003	0.021
05.03.2020 (2)	0.001	0.009
06.03.2020	0.002	0.010
07.03.2020	0.001	0.005
09.03.2020	0.001	0.007
11.03.2020	0.001	0.006
16.03.2020	0.001	0.006

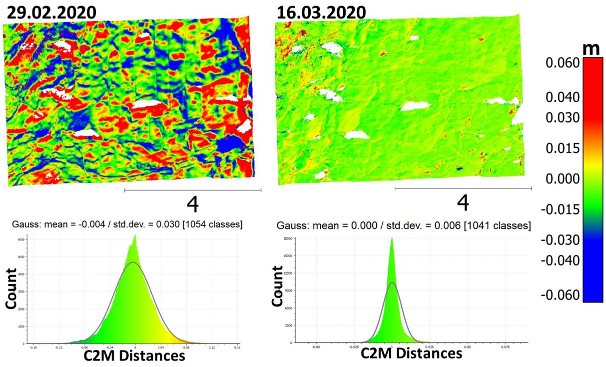

Figure 4.13: The figure presents the cloud to mesh distance in two of the point clouds, over an ice free surface. The 29.02 model shows one of the largest errors, while the 16.03 model have one of the smallest errors. The histograms below represent the distribution of the cloud to mesh (C2M) distances and the fitted gaussian curve.

Calculated Changes in Ice Growth

The evolution of the ice growth, as documented by the DSLR SfM models, was investigated in several different ways. The day to day changes of the ice was studied on a small scale, by examining the thickness of the ice in two small squares of the models and two longer cross sections. In addition, the total volume of the ice was calculated, providing a larger overview.

The cloud to mesh distances of two small ice covered sections of respectively 0.7 and 1 m^2 were studied. The sections are illustrated in Figure 4.14. The mean value ± SDE of the ice thickness for each point cloud is plotted in Figure 4.15. The red curve refers to area A, while the

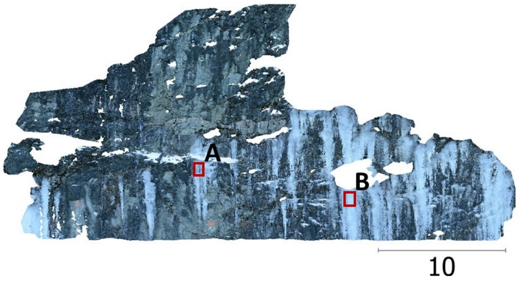

Figure 4.14: The squares A an B represent the area in which the temporal changes of ice thickness are investigated.

black curve refers to area B. In addition, the air temperature at the study site is included as a reference.

During the main period of minus degrees, between February 25th to March 1st, only one photogrammetry model was collected, on February 29th. The initial ice formation is rapid, and the model of the 29th shows a significant ice quantity after only 4 days. Between March 2nd and March 7th the temperature is primarily between 0.5 to 3°C. Despite the plus degrees the ice tend to continue to increase slightly for around three days, until March 5th. Both sections thickens by approximately 20% during this period, reaching a final mean thickness of 9.4 and 19.3 cm. The following days the temperature increases further, initiating a decrease in ice volume. On March 9th the thickness of area B is reduced to approximately 60% of the maximum, while area A is reduced to 20% of the maximum. Between March 13th and 14th the temperature drops slightly below zero, followed by an increase to 9°C on the 15th.

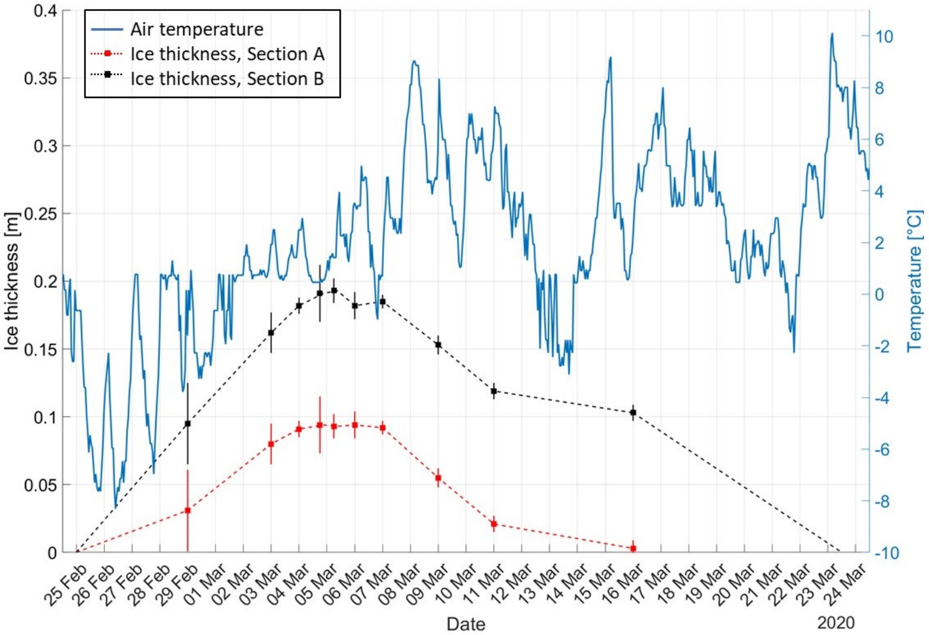

Figure 4.15: The red and black curves plots the evolution of the ice thickness in two areas during the cold period in February/March, as obtained from the ten DSLR photogrammetry models. Each measurement is represented by a square, and the corresponding SDE in vertical lines. The dotted lines are linear interpolations between each measurements, inferring the evolution of the ice thickness. The blue graph represents the temperature recorded at the study site.

The rate of ice decay decreases slightly during this period. On the 16th the ice thickness measures up to 10 cm in section B, while in Section A the ice is completely melted. The dashed line of section B continues to 0 cm on the 24th. This is not measured, but known from images on the stationary camera. The column that section B is part of is one of the lastly detached ice columns on the rock wall, as seen in Figure 4.11 B. The thickness of the ice of the November 11th 2019 model was calculated to 14.7 and 2.3 cm, which is significantly smaller than the maximum of the February/March period. This is due to the ice forming in different places each ice period, with the November model having larger thicknesses in other areas of the rock cut.

Furthermore, two cross sections covering areas of ice formation were investigated, presented in Figure 4.16. The black line represents the rock surface, as modelled by the reference mesh. The coloured graphs represent the ice models and their respective distance to the rock cut. The values are interpolated from the point cloud using a 1 cm resolution. The model collected on the November 11th 2019 is included, for comparison. Cross section BB' is separated into two graphs, for readability.

Cross section AA' covers the same vertical ice column that was studied in area B (Figure 4.14), showing a slightly overhanging rock cut. It shows a similar development as was described in Figure 4.15. On the 29th the average ice thickness over the cross section is 13.1 cm, increasing to 26.6 cm on the 03.03. The 29-02 model show "spikes" in parts of the section. These tend to correspond to areas of icicles. As the icicles for into massive ice columns, the ice generally grows in a plane manner, not following the structure of the rock. Between the 3rd and the 7th the daily growth is of 1-3 cm in thickness, while between the 9th and the 16th a continous decrease is observed, resulting in an average ice thickness of 16.6 cm on the 16th.

The horizontal cross section BB' covers both ice and rock. It reveals a skewness in the alignment between the reference model and some of the ice models, in particular the 29.02 model. The shift varies between 5 to 50 cm to the right of the reference model. This is apparent in the areas where the model is not covered by ice, showing deviations in the rock surface, which should coincide in the models. The 03.03 model also shows a slight shift of 0 to 10 cm to the left of the reference model. Neither of the models show consistent shifts, and studying extended cross sections, the shifts tend to decline towards the left in both models. The remaining models show a larger consistency, but with larger deviations compared to cross section AA'. Section BB' includes larger areas of freely hanging icicles, showing as spikes in the graph, and are particularly evident around meter 0.5, 2, 6 and 7. The trend in ice growth is similar to what was observed in section AA'. On the 16th a large part of the ice has melted, resulting in the graph corresponding closely to the rock surface.

In both cross sections, the model from 11.11.2019 is included, illustrating the change between two periods of ice formation. Along the ice pillar covered by section AA', the ice thickness is similar to the thickness that was obtained during the cold period in February/March. Section BB' shows that the ice formed in slightly different places, and with a larger thickness in some areas during the cold period in November.

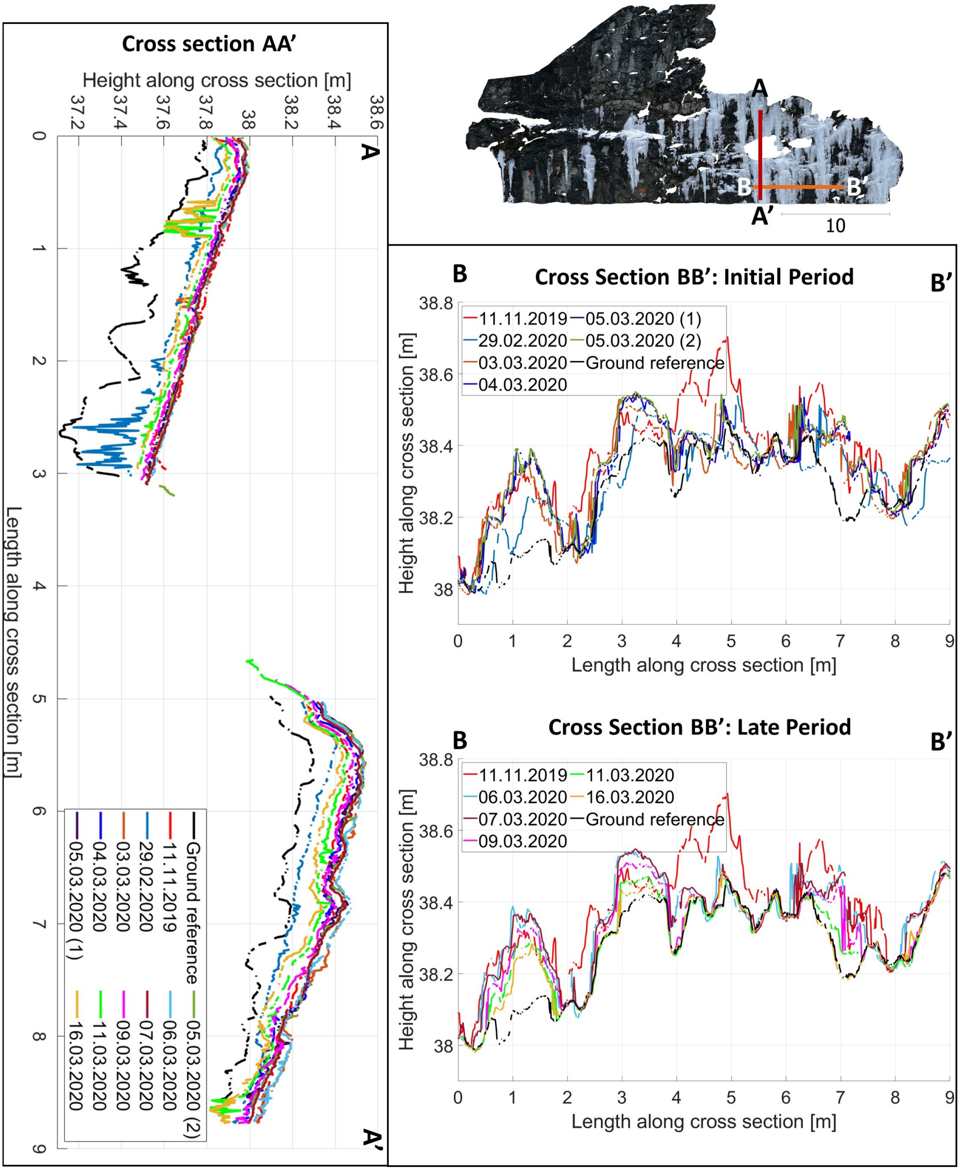

Figure 4.16: The figure illustrates the evolution of the ice along cross sections AA' and BB', positioned as shown in the upper right figure. Each graph represents the cross sections corresponding to the 12 photogrammetry models. The black line draws the surface of the rock, as produced by the reference model. The red graph is the cross section of the 11.11.19 model. The remaining graphs correspond to the models of February/March. The vertical cross section AA', covers a 9 m long section of an ice column. BB' covers a 9 m long horizontal section, only partly covered by ice. Notice that the scale of the axes does not correspond, resulting in an exaggerated y-axis. The graphs are acquired using the Cross Section tool in CloudCompare, projected along the length of the cross section, and the interpolated values in each 1 cm are plotted i Matlab. Areas that contain no points were omitted from the plot, resulting in areas of no data.

Lastly, the ice volume of each model was calculated, listed in Table 4.6. It was obtained based on the raster to raster comparison, as described in Section 3.3.5. An error interval is given based on the SDE (Table 4.5) of each model. It is calculated as the area of the ice cover times the SDE.

Between February 29th to March 3rd the volume calculations infer scattered changes in ice volume between 19.3 to 25.9 m^3, with no particular trend. On March 9th the ice volume is reduced to 60% of the maximum ice volume, and to 30% two days later. The largest value of error corresponds to the models of highest SDE, with the maximum error of ± 5.2 m^3 in the February 29th model. The lowest error is that of March 11th, with an error of ± 0.9 m^3. The volume calculations include all changes above zero in the volume. This will influence the models of low precision largely, and the method is not suitable for detecting detailed day to day changes.

Table 4.6: The table summarizes the calculated ice volume of each photogrammetry model. The error interval is calculated as the SDE times the area of the ice. Notice that "11.11" refers to the model of 2019, while the remaining models were all collected in the same cold period in February/March 2020.

Date	**11.11**	**29.02**	**03.03**	**04.03**	**05.03 (1)**	**05.03 (2)**	**06.03**	**07.03**	**09.03**	**11.03**	**16.03**
Volume [m^3]	29.2	23.5	25.3	24.2	25.9	19.3	24.5	23.3	14.7	7.6	12.4
Error [^{3}]	±4.1	± 5.2	± 2.9	± 1.1	± 4.3	± 1.9	± 2.0	± 1.0	± 1.3	± 0.9	± 1.0

4.3.3 Ice Evolution as Detected by Structure from Motion Embarked on a Vehicle

Overview of the SfM-EV Models

A total of eight SfM-EV models were collected using action cameras embarked on a car, of which four are presented in this thesis. The four remaining were discarded as the area of study was changed throughout the study, due to excessive snow cover or due to insignificant ice growth.

The SfM-EV model collected on October 3rd 2019 was used as the reference model for estimating ice growth. Another ice free model, collected May 1st 2020, was obtained as a tool to detect changes in the rock cut due to rock falls. The latter is presented in Section 4.4. Two models were gathered during ice cover, of which one was collected by NGU during the previous winter on March 13th 2019 and one was collected in the February/March period, on March 3rd 2020.

Table 4.7: List of the four SfM-EV models presented in the thesis. (1)Number of images used in the model / Total number of images. (2)Point density in a search radius of 0.5m. (3)The reprojection error is reported by the Agisoft software, and is the root mean square error of x, y and z averaged over all tie points in the sparse cloud. It is a measure of the accuracy of the tie points in the point cloud.

Acquisition Date	(1)**Images**	**Points in point cloud**	(2)**Point density [$m^{2^{-1}}$]**	(3)**Mean reprojection error [pixels]**
13.03.2019	193 / 193	40 144 592	6 113	0.96
03.10.2019	421 / 421	5 404 170	1 453	0.841
03.03.2020	429 / 429	4 459 913	1 210	0.741
01.05.2020	290 / 318	4 459 913	1 145	1.16

Precision

The precision of the SfM-EV models was calculated in a similar manner as for the DSLR models, on the same rock area. The errors are twice as large in the 13.03 model compared to the 03.03 model.

Table 4.8: The mean error and standard deviation of error of the two ice covered SfM-EV models, calculated on an ice free rock surface.

Aquisition date	ME [m]	SDE [m]
13.03.2019	-0.013	0.034
03.03.2020	-0.006	0.019

Calculated Ice Growth

The two ice covered SfM-EV models are presented in Figure 4.17. The point cloud generated from the photos collected in the previous winter (13/03/2019), failed to align properly, creating a slightly horizontally domed model. It was thus attempted to reduce the model to only include the area similar to the area of the DSLR models, as the doming effect is negligible over a shorter length. The ME and SDE in Table 4.8 is based on this alignment. The result is presented in Figure 4.18 showing both models from March 13th 2019 and March 3rd 2020 over a limited area, indicating a larger ice extent in the previous winter. This is apparent in the true colored models in Figure 4.17 as well.

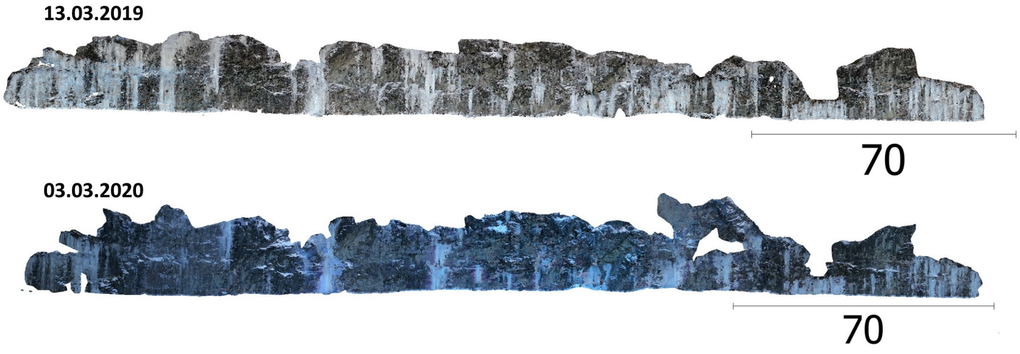

Figure 4.17: The two figures present the SfM-EV models collected on March 13th 2019 and March 3rd 2020.

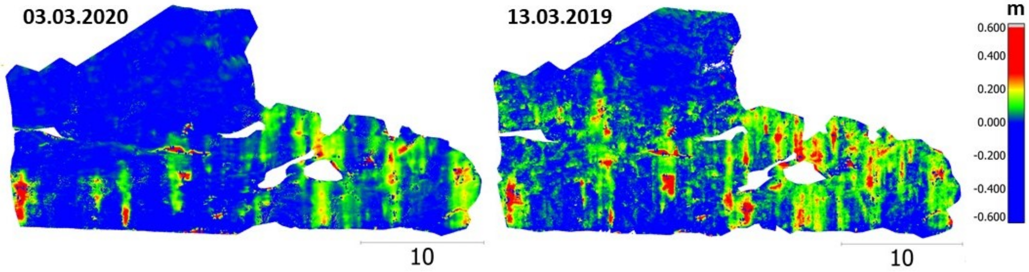

Figure 4.18: The cloud to mesh distance as calculated in the models of March 13th 2019 and March 3rd 2020.

4.3.4 Accuracy Analysis by LiDAR

A LiDAR scan and a DSLR model was collected on March 4th, when a significant amount of ice was present. The procedure was repeated on May 1st, when no ice was present. During both surveys plus degrees and melt water formed a thin film of water in certain areas. Table 4.9 summarizes the results of the obtained LiDAR clouds.

The DSLR models and corresponding LiDAR models are presented in Figure 4.19 A and B. The two LiDAR models cover the same area, but the ice model includes a slightly larger section on the top left and right. The recorded intensity of each point is a measure of the strength of the return pulse, and is largely dependent on the reflectively of the object. This allows for easy detection of the icicles. This is also apparent on the ice free model, separating the small dry spots from the wet surface (Figure 4.19) B. As the models were collected at a very close distance, the difference in intensity is not assumed to impact the quality of the model. Figure 4.19 C presents the cloud to mesh distances between the rock-rock (01.05.2020) and the ice-ice (04.03.2020) models of the LiDAR and DSLR model.

Table 4.9: Details of the two LiDAR models. The point density is calculated with a search radius of 0.01 m.

	Date	**Points in point cloud**	**Point density [$(\mathrm{m}^2)^{-1}$]**
With ice	04.03.2020	3 317 844	36 209
Without ice	01.05.2020	2 335 012	29 232

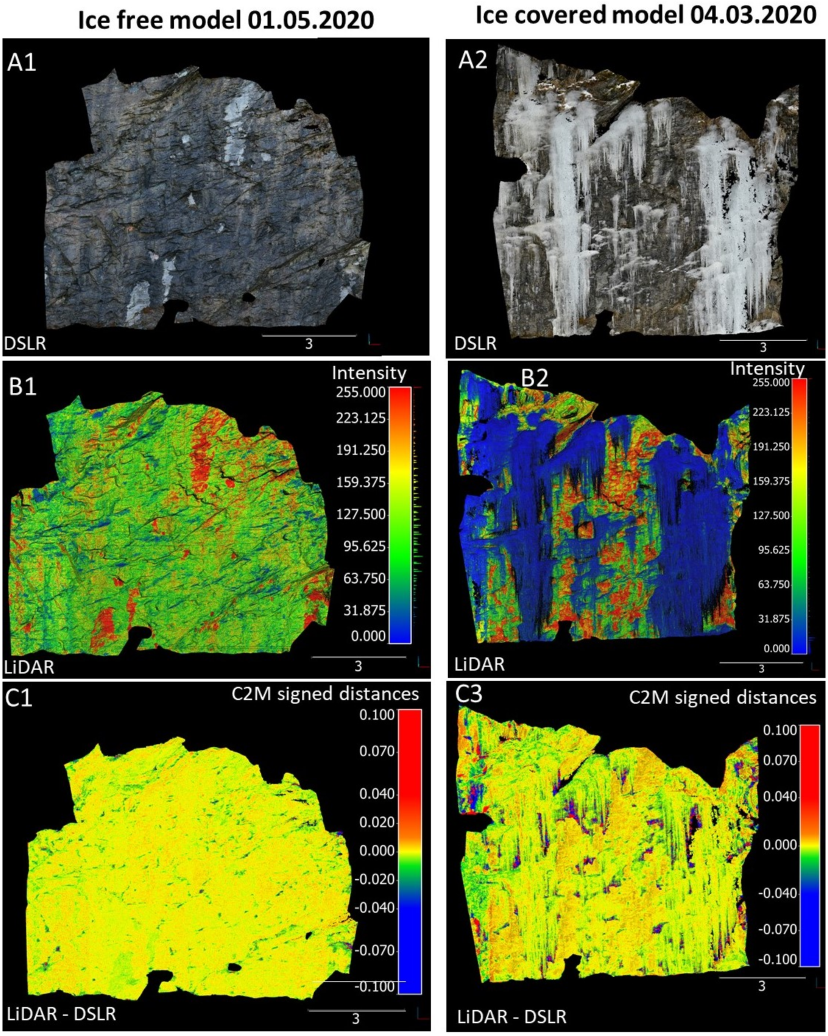

Figure 4.19: Comparison of two DSLR models to two LiDAR models, one ice free, and one ice covered. A1-2) DSLR models, showing the models with true colors. B1-2) The two LiDAR models, represented by the intensity, showing a large difference in signature on the ice or on wet spots. The scale is relative and without units. C) The cloud to mesh distances between the LiDAR and the DSLR models. The scale is in meters.

A measure of the overall surface accuracy of the photogrammetry models, applying the LiDAR scan as the «true» surface, can be evaluated from the ME and SDE of the cloud to mesh distances over the entire surface measured between the ice-ice and rock-rock models. The rock model have an ME of 0 mm and SDE of 4 mm. The ice model have a larger SDE of 12 mm. The values are listed in Table 4.10.

	Acquisition date	**ME m]**	**SDE [m]**
With ice	04.03.2020	0.000	0.012
Without Ice	01.05.2020	0.000	0.004

Table 4.10: The mean error (ME) and standard deviation of error (SDE) over the entire surface (Figure 4.19), obtained by aligning an ice covered DSLR model to an ice covered LiDAR model, obtained on the same day, and by aligning an ice free DLSR model to an ice free LiDAR model, and calculating the ME and SDE from the cloud to mesh distances between the models.

4.4 Registered Rock Falls During the Winter of 2019/2020

Based on mapping of the road shoulder, four changes in terms of rock deposits were observed between October 3rd 2019 and May 1st 2020. These are interpreted as rock fall deposits. The changes are photographed in Figure 4.20. The deposits in Figure 4.20 A are the most substantial in size, and consists of several blocks. The area of release is 0-15 m above the ground. The upper half of the above rock cut is covered by a rock fall net. Based on observations from photos, the rock fall occurred between the 04.02.2020 and 29.02.2020. A rock fall was registered in the NVE landslide database with date of occurrence on the 21.02.2020. The registered position deviates by 150 m, but based on the time of the event one may interpret that these represent the same event.

Figure 4.20 B shows an increase of colluvial soil, forming on top of previous rock fall deposits. This may indicate out wash of joint infill, which possibly can create stability problems over time. The material derives from 0-50 m above ground. Along this section, the majority of the wall is covered by a rock fall net. Figure 4.20 C and D show rocks of smaller size (∼10x10 cm). The release area is 0 - 50 m above ground. The time of release is difficult to estimate, as the ground and rock deposits are covered by ice in the majority of the images. Lastly, a rock block of approximately 30 x 20 cm have detached behind the rock fall net, but is caught by the net further down. The time of the event was between November 24th and January 30th, as detected from photos. The approximate positions of the deposits are given in Figure 4.21. The rock caught by the rock fall net is positioned slightly to the left of the area covered by the model. The section was excluded during processing due to poor alignment of the photos.

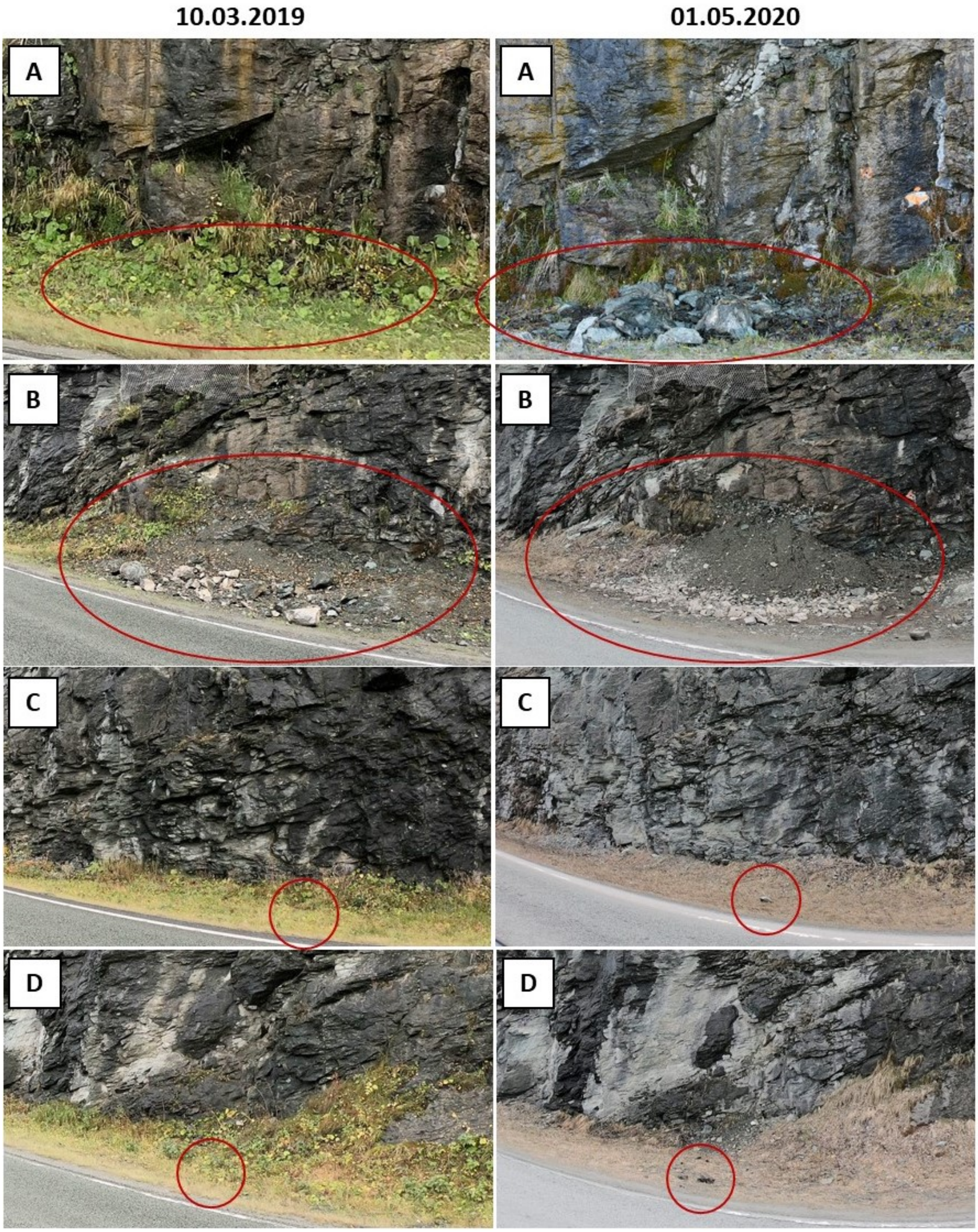

Figure 4.20: Changes along the road shoulder due to possible rock falls. The left photos were taken the 03.10.2019, while the photos to the right show corresponding images captured on the 01.05.2020. A total of five changes were observed, of which four are photographed here. The last occurred behind the rock fall net, and did not reach the ground. A) The largest rock fall observed, consisting of several smaller blocks of up to 20x20 cm. The rock fall occurred between February 4th to 29th. B) Increase in colluvial soil. C) and D) Small rock fall deposits of 10x10cm.

Furthermore, the ice free SfM-EV model of May 1st was aligned to the reference model of October 3rd. This was performed as a tool to detect changes in the rock wall due to rock falls. The model however failed to align properly, revealing a systematic error in the 01.05 model. This is apparent in Figure 4.22, showing excessively large cloud to mesh distances in the edges of the model. Table 4.11 lists the ME and SDE calculated on three surfaces, as a mean to estimate the deviations. The surfaces cover 1) an area covered by a rock fall net, 2) a rock surface in the central part of the model and 3) a rock surface in the right part of the model. The SDE vary from 4 to 28.6 cm. Due to the large deviations, it was not possible to separate areas of actual change from change related error.

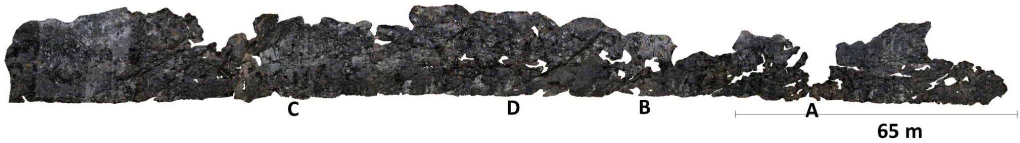

Figure 4.21: The photogrammetry model of 01.05.2020. The letters corresponds to the position of each rock fall deposit, as presented in Figure 4.20.

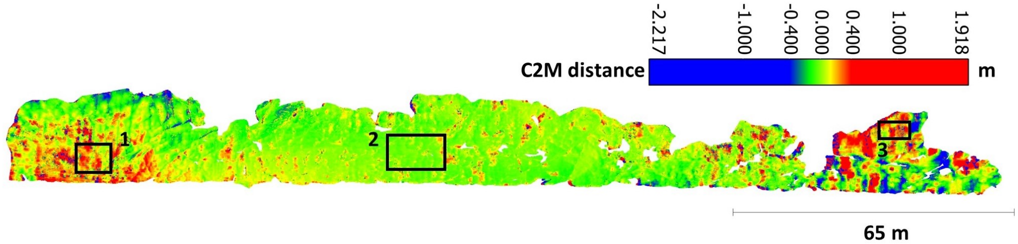

Figure 4.22: The cloud to mesh distances between the 03.10.19 and the 01.05.20 model. The three squares represent the areas in which errors were investigated, covering a rock fall net (1), and two areas of rock surface (2-3).

Table 4.11: The ME and SDE of the cloud to mesh distances in three areas of the model. Assuming no rock fall of significant size has occurred in those particular locations, the ME and SDE are a measure of the errors related to precicion.

Location	ME [m]	SDE [m]
1) Rock fall net	0.151	0.1442
2) Rock surface, center	-0.008	0.040
3) Rock surface, right	0.087	0.286

Chapter 5

Discussion

5.1 Evaluation of Methods for Investigating Ice Growth

The main goal of the various methods for surveying ice growth was to aid in understanding how the rockwall icing develops with time and temperature. Additionally, as there are only a few studies on the topic, it was of interest to evaluate the suitability of the methods, as SfM has, to the author's knowledge, not been applied for this particular purpose. As photogrammetry is often considered an easier and faster method for 3D modelling, compared to more traditional methods like LiDAR, it is valuable to investigate its suitability for various applications. The method of mapping the areal extent based on 2D images is considered an even simpler approach, and a brief discussion on its suitability is also included.

5.1.1 Comparing DSLR to LiDAR - Evaluation of the Accuracy

Comparing an ice free DSLR model to a corresponding ice-free LiDAR model showed an error of 0±4 mm between the rock-rock models (Figure 4.19). The introduction of ice in the model resulted in a tripling of the SDE, with an error of 0 ± 12 mm in the ice-ice models. In order to investigate how the errors distribute throughout the ice model of March 4th, three areas covering respectively massive ice, rock, and freely hanging icicles were studied, shown in Figure 5.1. The frequency histograms of the cloud to mesh distances for each area are plotted in Figure 5.1 C.

The cloud to mesh distance in the area of rock is 2 ± 4mm. The ice covered area show a similar result, with cloud to mesh distance of 0 ± 5 mm. The ice itself thus seems to be reconstructed well in the SfM model, with errors in the scale of millimeters. The largest errors in the ice model tend to concentrate in the areas surrounding the freely hanging icicles. It is apparent that the photogrammetry software has trouble detecting the limits between the icicles and the rock wall when there is a void between the two. Instead, the icicles are surrounded by a darker sphere in the photogrammetry models. The problem is also apparent in several of the other photogrammetry models. One might reduce this artifact by photographing the ice from more angles and distances, in addition to improving the exposure setting for the images. This may be considered the largest error that is introduced by the use of photogrammetry for reconstruction of rockwall icings. It will lead to a slight overestimation of the ice volume in the photogrammetry models.

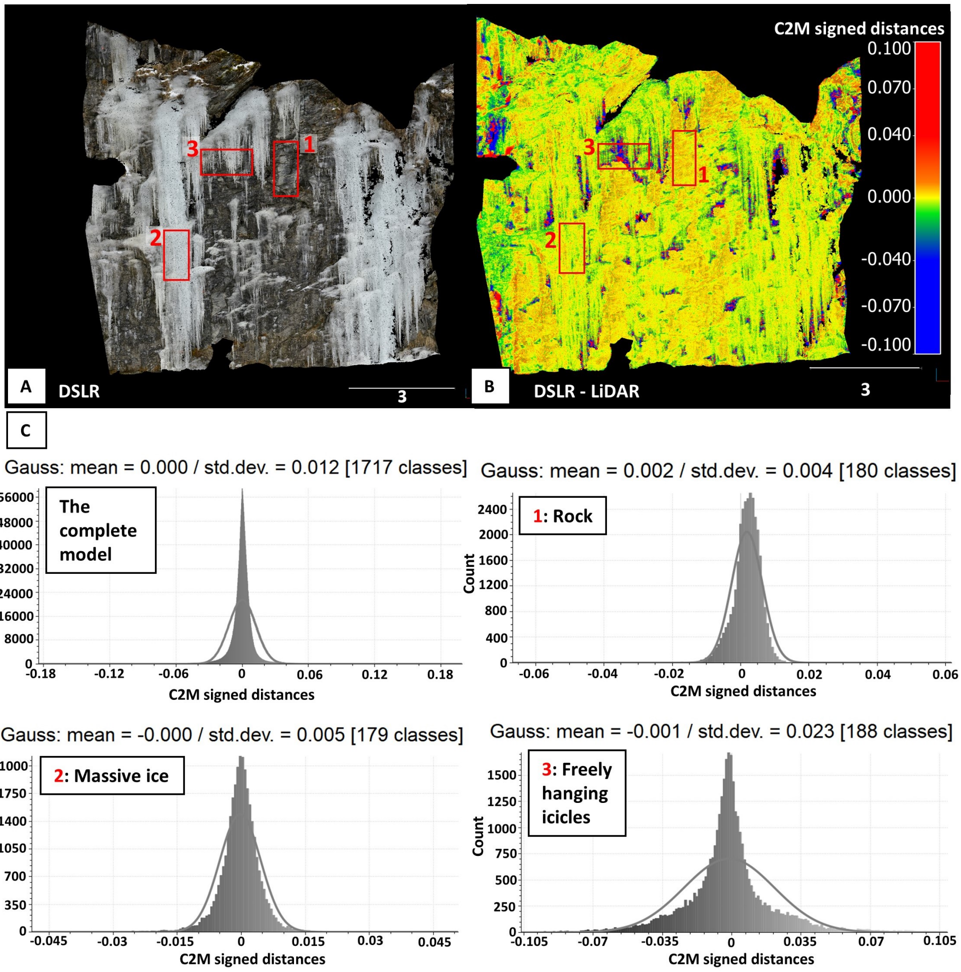

Figure 5.1: Investigating the deviations between an ice covered DSLR model and a corresponding ice covered LiDAR model, collected on March 4th. A) The DSLR model showing the true colored extent of ice and rock. B) The DSLR point cloud is aligned to the LiDAR mesh and the cloud to mesh distance is calculated over the entire surface. C) The graphs show the distribution of cloud to mesh distances in four different areas, as marked in Figure A. The first represents the errors throughout the entire model, while area 1, 2 and 3 correspond to areas covering rock, massive ice and freely hanging icicles, respectively. Notice that the x-axis varies for all graphs, and is based on the minimum and maximum value of the given data. All units are in meters.

The main errors of the ice free models occurs in sharp edges of the rock, where the point density is low, due to poor image coverage. This may also be affected by the LiDAR scan, as sharp edges are generally known to be more poorly reconstructed (Sturzenegger and Stead, 2009).

For more representative accuracy estimates of the rock-rock comparison, it would have been preferable to compare the LiDAR model to the October 3rd SfM model that was actually used as the reference mesh in the volume calculations. Instead, the LiDAR model was compared to an SfM model that was not used for other purposes than the comparison itself, simply due to no LiDAR scan existing from October 3rd. The 01.05.20 model showed the lowest mean reprojection error of all models, of 0.39 pixels, while the 03.10.20 model has the highest value of all the generated models, with 1.17 pixel error (as listed in Table 4.4). As the mean reprojection error can be used as a measure of the quality of the models, the calculated rock-rock error of 0 ± 4mm may thus be regarded as a slightly low estimate of the errors, compared to the 03.10 model.

Furthermore, the mean reprojection error can be used as an indication of the quality of the models where no LiDAR scan was available for comparison. The reprojection error in the majority of the remaining ice models is similar to value of the 04.03 model, indicating similar accuracies. The models of low precision correspond fairly well to the models of high reprojection error. An exception is the 03.03 model, that has a fairly low reprojection error of 0.51 pixels, but a high SD of 0.015. This may indicate that the model itself is of good quality, but the alignment to the reference mesh is poor. This is also confirmed from the cross section (Figure 4.16), showing a distortion in the alignment.

The comparison of LiDAR to SfM shows that SfM provides good results for mapping the ice cover. A large amount of freely hanging icicles will, however, degrade the result. The main disadvantage related to the method of LiDAR compared to photogrammetry is the increase of time spent in the field. The photogrammetry models were during certain periods collected once every day, and exchanging LiDAR with SfM would increase the time considerably. With a distance to the rock wall of only 10 meters, the field of view of the LiDAR is small, demanding several scans and an increase in time to cover the same area as with the DSLR camera. In addition, the LiDAR equipment is heavy and expensive compared to the equipment needed for photogrammetry, demanding a car for transport. Even though the LiDAR scan provided a good mapping of the ice coverage only based on the intensity, another advantage of the photogrammetry models is the possibility to obtain real colors, aiding in mapping the extent of the ice.

In addition to being slightly more accurate than photogrammetry, there are several other advantages related to LiDAR. The time consumption in the field is higher, but the processing time is considerably lower. All the photogrammetry models demanded significant manual adjustments in Agisoft Photoscan. In addition, generating the sparse cloud and the dense cloud requires processing time and computer power. The rock cut was partly covered by vegetation, which had to be removed during processing. In the photogrammetry models, this results in empty areas in the point cloud where vegetation is removed. The problem is reduced by applying LiDAR, as the pulses pass through vegetation, allowing for reconstruction of the rock covered by sparse vegetation. Lastly, another advantage of using LiDAR is that it does not depend on good light conditions. Photographing a north facing side during the winter at 63° north leaves only a short time span for collecting photos of good quality. This problem is omitted by the use of LiDAR.

5.1.2 Sequential Photogrammetry by DSLR

Following is a further evaluation of the individual SfM models, and a discussion on the various factors influencing the quality. Table 5.1 summarized the possible sources of error for the individual models, together with the ME and SDE for reference (as was calculated in Section 4.3.2, Table 4.5). Lastly, the various methods for calculating day to day changes and annual changes in ice quantity are discussed.

The surface of the rock cut is evaluated as fairly good for the purpose of photogrammetry, however the local presence of vegetation and rock fall nets are contributing to a decrease in quality, and an increase in time consumption during image processing and point removal. As the rock fall nets are installed specifically in areas where the ice formation is large, it was not possible to obtain a study site without rock nets and sufficient ice formation. Previous research show similar poor results in the reconstruction of protective nets (Voumard et al., 2017). As the presence of vegetation changes throughout the year, it impacts the models to various extents. The reference model, in particular was partly covered by leafy vegetation, while the other models were collected during the winter or early spring, with less vegetation present.

All models show a high point density, providing information about the surface on a millimeter scale. Based on literature it was expected that the introduction of ice in the model would reduce the quality and reconstruction accuracy, due to strong contrasts and reflective surfaces (Bemis et al., 2014; Smith et al., 2016). The largest challenges seemed to be related to the contrasts between the light ice and the darker rock. With large contrasts it is difficult to obtain photos with sufficient details in both the rock and the ice, as various camera exposures will favour either of the two. A correct camera exposure is thus particularly important for this type of motif, and had to be set manually for each model. Models with too dark or too bright photos tend to be associated with lower precision. Furthermore, the reflective properties of the ice changes throughout the cold period, with a more reflective surface in the early stage of formation, and more matte white after the initial stage and during melting, which may also be an impacting factor in the reconstruction quality of the SfM models (Arnhardt and Smith, 2016; Bemis et al., 2014).

The mean reprojection error of the reference model is particularly high, as mentioned in Section 5.1.1. This is assumed to be related to poor processing of the photogrammetry model, in addition to the vegetation still having leaves when the model was collected. As the quality of the images are good, and the ice-free model of May 1st show a significantly lower mean reprojection error, one cannot account the high error to the object photographed or to poor image quality, thus the assumption of poor processing. In addition, it may be related to a high amount of stations. This is in coherence with Bemis et al. (2014), stating that "Increasing angles of convergence between overlapping images will tend to increase reconstruction accuracy up to a point, but will eventually prevent matching due to the surface texture appearing too dissimilar in images from different directions".

There generally tends to be a decreasing trend in errors throughout the study period. The acquisition procedure and the processing of the models were both optimized and standardized throughout the study period, based on the knowledge obtained from the previous models. This highlights the value of a good preparation and early evaluation of the initial results. The four last models that were collected show a good coherence in precision with an ME of 1 mm and SDE of 5-7 mm. This suggests that the obtainable precision, assuming optimal acquisition and processing is around 5-7 mm. The high reprojection error of the reference model impacts the estimated precision of all aligned models, and an improved reference model may have improved the precision further.

Table 5.1: The table lists the various factors that are observed as factors possibly impacting the quality of the models negatively. The ME and SDE are given for each ice model (as was also given in Table 4.5), for reference.

Acquisition date	**ME**	**SDE**	**Error sources**
03.10.2019	-	-	Low angles between each station (17 stations), leafs on vegetation, high mean reprojection error.
11.11.2019	0.005	0.018	Poor image coverage (5 stations), high mean reprojection error.
29.02.2020	-0.004	0.030	Bright photos, slightly snow covered, reflective ice.
03.03.2020	0.004	0.015	Reflective ice.
04.03.2020	0.000	0.006	Reflective ice.
05.03.2020 (1)	0.003	0.021	Snow covered, dark photos.
05.03.2020 (2)	0.001	0.009	Snow covered, dark photos.
06.03.2020	0.002	0.010	Dark photos.
07.03.2020	0.001	0.005	-
09.03.2020	0.001	0.007	-
11.03.2020	0.001	0.006	-
16.03.2020	0.001	0.006	-

A high mean reprojection error is not directly an error source, moreover it is a result of the error source. It is however included as an error in Table 5.1, as it may also be an indication of poor manual processing, as mentioned above. In addition, snow coverage will not impact the precision or model quality, but will impact the calculated volume.

5.1.3 Photogrammetry by Action Cameras

The point clouds developed by SfM-EV were used to evaluate the annual variation in ice growth, based on models collected in the winters of 2018/2019 and 2019/2020. In addition, it was attempted to detect rock cut changes due to rock falls. The method provided results of various quality.

Both the point cloud generated from the data collected the previous winter (13.03.2019) and the 05.01.2020 model showed a "doming" effect, with errors increasing toward the lateral sides (James and Robson, 2012). For the 13.03.19 model, it was attempted to estimate the ice thickness on a smaller section of the model. In this area the error was calculated to -1.3±3.4 cm (Table 4.8). The 01.05.20 model showed even larger errors with an ME and SDE on a decimeter scale (Table 4.11). The 03.03.20 SfM-EV model did not show systematic errors of the same kind, and have errors similar to that of some of the DSLR models of lowest quality (Table 4.8).

The doming effect is a recognised problem in SfM and typically occurs when the photos are captured along a parallel line, as was the case here (James and Robson, 2012). Improvement may be obtained by including photos from a different angle, including ground control points of known position, or by applying correctly positioned targets obtained from a similar model. The latter was obtained, but did not provide an improved result.

The rock falls that occurred during winter were relatively small. As the errors are of a similar scale, the changes due to rock falls cannot be detected. Another important reason is the fact that the largest rock falls occurred behind rock fall nets or vegetation, which is poorly reconstructed by photogrammetry. As a consequence, detecting changes in these areas demands larger volume changes than what was observed from the size of the deposits, and/or methods of higher accuracy.

5.1.4 Calculation of Ice Change

Various methods were applied to quantify the growth and decay of the ice. These include calculating the areal extent based on images from the stationary camera, calculating the volume based on a raster to raster comparison, and by evaluating the thickness of the ice in specific areas of the models. Following is a brief evaluation of the various methods.

The method of calculating the mean thickness over a small area of the ice (Section 4.3.2) provided a good measure for estimating the detailed day to day changes in ice thickness. Figure 4.15 plots the uncertainty based on one SDE. This is regarded a slightly low level of confidence, and increasing the value of uncertainty to two standard deviations (95%) may be a more appropriate value (Brasington et al., 2003; Lato et al., 2015). The thickness variations between March 3rd and March 7th are very small, and depending on the size of the errors one cannot say with confidence that all are statistically different from each other.

The method is, however, not applicable for comparing the ice growth in separate cold periods, as the ice forms in slightly new locations every period. This was apparent in the cross section in Figure 4.16, with the November 11th model forming ice in other places than in the February/March period. The method is to a less extent affected by snow cover, as the largest volumes of snow are found on horizontal shelves and adhered to the rock.

The raster to raster comparison, calculating the volume, is a commonly used method for detecting changes such as landslides, glacier retreat etc. (eg. Kenner et al., 2011; Lim et al., 2005). The method did however prove challenging for estimating the detailed changes in ice volume, as the volume is largely impacted by the model errors. All changes larger than zero were included in the volume. This will result in including areas that are not related to «true change», and as the volume is relatively small compared to the area on which it is measured, the errors will impact the volume significantly. One may include values only related to the detectable change, typically set to a threshold of 95% of the error (Abellán et al., 2011; Lato et al., 2015), but this will result in omitting all areas of thin ice formation. Based on the values obtained, the maximum volume scatters around 25 m^3 during the February/March period. The volume calculated from the models of February 29th seems to bee too large, as it does not correspond to the thickness calculations or to visual observations, and the error interval of $\pm$ 5.2 m^3 confirms the large uncertainty. In addition, the March 5th (2) volume is small, considering both preceding and succeeding days have volumes of 5-6 m^3 larger. Additionally, the volume calculations are impacted by snowfall, which may wrongly increase the calculated volume. The method is however useful for assessing the approximate annual changes, and larger ice volumes and larger day to day changes may provide better estimates of the volume, as the impact of the errors will decrease.

Lastly, the images from the stationary camera were also applied as a method for estimating ice growth. The method is easy and the calculation of ice area is far less time consuming than for photogrammetry. The trend in the measured ice growth is fairly similar to what is measured by the method of ice thickness. A comparison is shown in Figure 5.2. The method is however highly sensitive to snow, and the normalized area increases significantly after every snow fall. The color recognition provides better results when the contrast in color is large, which it is during the period of melting. During this period, the calculated area coincide well with the thickness changes calculated from the photogrammetry. Regardless of the area calculations, the automated camera is considered a very valuable tool for understanding the ice growth, as it provides a good visual understanding of the detailed ice changes.

5.2 Discussing the Growth and Decay of Rockwall Icings

Finally, the ice formation and decay will be discussed based on the observations and results obtained during the two previous winters. The majority of the observations derive from the cold period in February/March 2020, which is the main period of focus. Despite sparse observations, the cold periods in March and November 2019 provide valuable information on the variations in each period of ice formation, and are compared to the February/March period. The air and rock temperature are the only controlled parameters impacting ice growth, and the ice growth is thus mainly discussed based on the changes related to temperature. Thoughts on other factors such as precipitation and runoff, sun impact and thermal radiation are also discussed briefly, but with far less certainty. Lastly, a discussion on the impact of climate change on rockwall icings is presented.

5.2.1 The Ice Evolution of February/March 2020

The various data collected during the period of February/March 2020 is summarized in Figure 5.2, including the rock temperature, air temperature, FDH, precipitation, ice thickness and areal extent, based on the previously presented Figures 4.12, 4.15, 4.4, 4.5 and 4.6. The ice formation and decay during this period can be divided into three main stages of ice evolution, characterized by ice growth, ice growth stabilization and ice decay. The duration of each period is marked as blue, yellow and red sections in Figure 5.2. The first stage is characterized by approximately six days (25.02 to 01.03) of negative temperatures, in which the majority of the ice was formed. The second stage is recognized by temperatures slightly above zero, lasting for around six days (02.03 to 07.03). During this period there is a small continuation of ice growth, followed by a stabilization around March 5th. The last stage is characterized by higher temperatures, initiating a decrease in the ice volume and a series of smaller ice falls.

Ice Formation
Observations from the stationary camera show that negative air temperatures lead to a high ice growth rate in the beginning of every cold period, with ice forming only a few hours after negative temperatures occur. The freezing is initiated by a thin crust of ice on the rock, followed by the formation of vertical stalactites formin on to of the crust. During the cold period in March, the ice volume is of a significant volume after only 4-5 days of minus degrees, with ice columns of several meters and a thickness of 15-25 cm. Already at this point, the size of the ice columns can

be regarded as large enough to create hazardous ice falls, based on its size. The FDH reached a maximum value of 388 on March 2nd.

Gauthier et al. (2015a) and Montagnat et al. (2010) observed a close to linear trend in the initial ice growth phase, corresponding well to the curve of the FDH, followed by an asymptotic growth progression. The asymptotic growth was initiated after more than 100 days of minus degrees and FDH of around 12 000 (Gauthier et al., 2015a), thus implying a completely different temperature regime than what can be observed at the study area. With only one photogrammetry model collected during the ice growth phase, inferring a correlation between the temperature and/or the FDH is challenging. Between February 25th and March 3rd a linear trend in ice thickness can however be suggested (Figure 5.2 C). As the temperature increases to above 0°C in the following days, it is not possible to interpret the proceeding growth if the cold period had been longer.

The ice volume of November 11th was measured after a period of 11 days of minus degrees, showing a slightly larger ice extent than what was measured the 29th of February, with ice volumes of 29.2 m^3 and 23.5 m^3, respectively. The FDH of November 11th and February 29th summed to 600 and 320, respectively. Inferring a linear correspondence between the ice volume and the FDH during the initial growth period would result in a volume on the 11.11 twice as large as what is observed on the 29.02. As this is not observed, this either suggests that 1) the growth rate in November was lower than that of March, suggesting a different growth regime, or 2) the growth rate was already declined before the 11.11, resulting in an asymptotic evolution as was observed by Gauthier et al. (2015a) and Montagnat et al. (2010). As these two models are of the models with the largest errors (0.5 ±1.8 cm and -0.4±1.5 cm, Table 4.5), the volumetric calculations, and the discussion above should however be evaluated with caution.

In addition to ice formation resulting from negative temperatures, it is apparent that snow fall increases the volume of the ice. This is particularly visible from the normalized area calculation (Figure 5.2 B and C). Part of the increase cannot be regarded as an actual increase in ice volume, however, the snow tends to recrystallize over days, resulting in a final increase in ice volume.

Growth Stabilization

The second stage shows a continuous increase in ice thickness for two to three days, even with temperatures above 0°C. The increase in ice thickness during positive temperatures implies that the changes in ice volume is not solely dependent on the air and rock temperature. As was stated in Section 2.1.5, the nocturnal radiation on cloudless nights may result in an outward energy transfer from the ice to the atmosphere, even with temperatures above zero. The phenomenon mainly occurs when the air temperature is only slightly above 0°C (Hamberg et al., 1987). The increase in ice thickness between the 3rd and the 5th may imply that the positive air temperature and radiation during the day does not counterbalance the nocturnal freezing. During some of these days, frost was observed on the ground in the morning, which is caused by the same phenomenon of nocturnal radiation (Hamberg et al., 1987).

On the other hand, the areal extent of the ice (Figure 5.2) C shows a trend of ice reduction during the same period, except between the 4th and the 6th. The latter increase can be explained by a heavy snowfall on the 5th of March. For the remaining days, the images on the stationary camera certainly show some decrease of areal extent during this period, even though the calculated thickness shows to be increasing or stabilizing. The reduction in the areal extent is mainly visible in the areas of thin ice crust superimposed on the rock. This suggest that the combination of the heat of the rock and the positive air temperatures is larger than the effect of the nocturnal freezing, and will melt the thin crusts during the day. In the areas where the ice is thicker, the increase due to nocturnal freezing may not be counterbalanced during the day, as the ice itself is below 0°C. As the slope receives close to no sun, the impact of sun radiation is non existing. Both Norem (1998) and (Gauthier et al., 2015a) found that the sun will influence the growth and decay to a large extent, and further studies should address this parameter by studying south facing slopes.

Ice Decay
The last stage of the February/March ice evolution is commenced by a fast temperature increase to 9°C on the 8th of March. This initiates a decay in ice thickness, and several smaller ice falls are generated during the following period. The largest ice fall is observed between the 7th and the 9th, where a column that is only slightly supported from the ground has toppled forward and into the road shoulder. In addition, two relatively large sections detach on the 12th and the 18th, as was visible in the frame of the stationary camera (Figure 4.10 and 4.11 A). The ice tends to melt considerably prior to every observed ice fall, such that the majority of the blocks are relatively small. In addition, the ice blocks seem to have a low strength as a result of the increase in temperature. Field observations show that the impact with the ground instantaneously attenuates the ice fall, breaking the blocks to small pieces, resulting in a short run out distance. No ice falls are observed to reach the road during the period of ice decay in March. The longest run out is related to toppling ice blocks, with the distance of the run out corresponding to the length of the ice column.

As stated by Norem (1998), ice falls occur by several release mechanisms. The perseverance of the ice to stay attached to the rock wall is dependent on the failure mechanisms, with direct falls typically occurring earlier than sliding and toppling ice falls. At the study site, all three types of ice fall mechanisms are observed. The majority of the ice falls occur by a combination of falls and sliding. The release plane of the ice seems to primarily be in the intersection between the rock and the ice. In addition, some of the freely hanging icicles break off in the lower part of the icicle, with no interaction with the rock. Ice columns supported by the ground have a higher endurance compared to the freely hanging ice, and are of the last sections to collapse. The majority of the ice columns are larger and thicker than the ice stalactites, often resulting in a more substantial ice fall than freely hanging ice.

An assumably important consequence of the increase in temperature during warm periods is not only the melting of the ice itself, but the melting of snow creating increased runoff, and the possible thawing of the ground. Whether the water derives from snow melt, liquid precipitation or ground water will impact the water temperature, and thus the rate of melting. Measuring the temperature of the run off water may increase the understanding of the impact from water. Observations show that the majority of the water forming the rockwall icing derives from the soils above the road cut, and water is continuously percolating over the surface.

There are four days of observed rain, on March 12th and from March 17th to 19th, as marked in Figure 5.2 B. During both periods, some of the largest ice falls occur. On the night between the 12th and 13th a large column collapses (as was marked in Figure 4.10), while on the 18th a larger flake collapses, in addition to several smaller ice falls (Figure 4.11 A). Based on these sparse observations one can infer that the ice fall frequency is accelerated by liquid precipitation, however it is difficult to specify the certain degree of impact from precipitation versus temperature. A larger amount of observations is necessary for further interpretation of the correlation. In addition, the quantity of precipitation was not registered, as all observations are based on what is visible from the automated camera.

Rock Temperature
Lastly, the changes in rock temperature throughout the study period was investigated. The rock temperature loggers all show similar trends, with the exception of logger 411b, 416 and 418, which were all covered by ice, and logger 413 which generally recorded a higher temperature than the other loggers. The temperature of the loggers that were not ice covered, coincides clearly with the trend of the air temperature, but are generally recognized by smaller amplitudes. There is a slight lag in the response of the rock temperature to changes in air temperature. However, the rock temperature tends to reverse towards 0°C before the air temperature does. This indicates that the frost intrusion in the rock is shallow, such that the logger temperature is impacted by the internal rock, which has a temperature above 0°C. Longer periods of minus degrees might create a deeper frost intrusion in the rock, leaving the rock frozen after the air temperature increases to 0.

The behaviour of the three ice covered loggers imply that the ice isolates the rock such that it is less impacted by the air temperature. The rock temperature measured by these loggers is above 0°C during the majority of ice coverage. This suggests that the ice is largely held up by friction between the ice and the rock, or by support from the ground, and not by being frozen to the rock. This is the opposite of the findings of Gauthier et al. (2015a), who observed rock temperatures below zero during ice coverage. The winter of 2019/2020 was characterized by mild temperatures, and it is reasonable to believe that longer and colder periods of negative temperatures would eventually impact the rock and create frozen ice bridges between the rock and the ice. This would allow for sustaining larger ice volumes on the rockwall, but may also result in larger collapses if the ice bridges melt, as the friction may not be sufficient for sustaining the weight. The latter is not observed due to the mild winter, but should be studied further in a possible continuation of the study.

There seems to be no particular correspondence between the depth at which the logger is installed and the temperature. The difference in depth was of maximum 1.2 cm, and with a measuring accuracy of ± 0.5 °C, the temperature differences may have been within the obtainable accuracy.

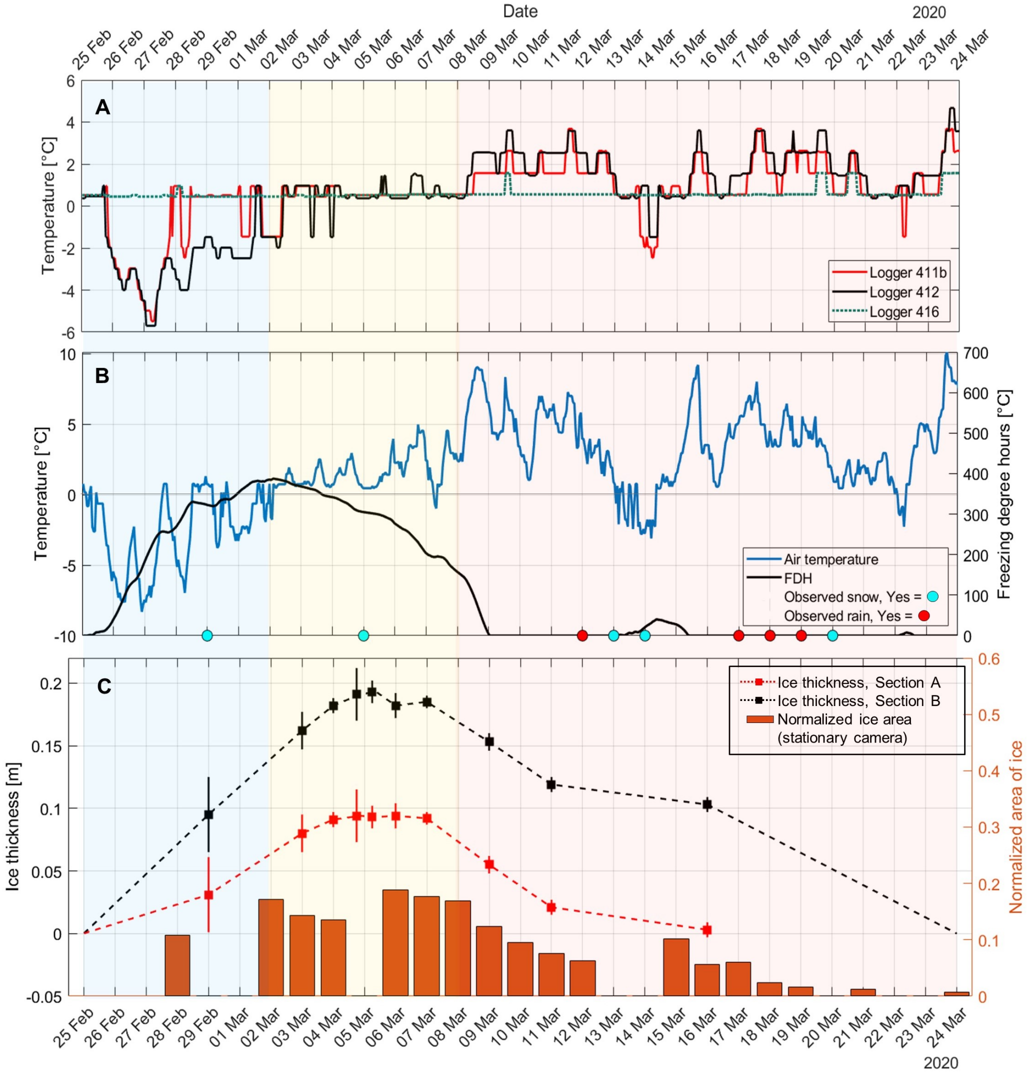

Figure 5.2: The graphs present a final overview of the collected data during the ice formation period of February/March. The graphs are based on the previously presented Figures 4.12, 4.15, 4.4, 4.5, 4.6. Figure A presents the rock temperature registered by logger 411b, 412 and 416. Only three loggers are included as these provide a general overview of the temperature for ice-covered and non-covered loggers. Figure B presents the air temperature, calculated as the hourly mean of logger 001, 002a and 002b, in addition to the FDH and the observed precipitation. Figure C shows the ice evolution as the calculated ice thickness, as obtained from the DSLR photogrammetry models, and the normalized ice area, as obtained from photos from the automated camera.

5.2.2 Comparing the Observed Periods of Ice Formation

A comparison of observations to other periods of ice formation is important, as it alters singular events to statistics. As the observations during the two other periods are sparse, this is however challenging. Following is an overview of the observations from March and November 2019, followed by a discussion on the main differences and similarities to the cold period in February/March 2020, summarized in Table 5.2. Figure 5.4 presents the temperature and FDH for all three periods, with the length of negative temperatures and ice formation marked in blue, and the period of observed ice falls marked in red. The latter is not known for March 2019. Figure 5.5 presents the cloud to mesh distances from the three different periods of ice formation, all representing what can be assumed to be close to the largest ice extent of that period. From the figure it is apparent that the ice extent was largest in the period of March 2019, followed by November 2019, while the ice quantity of the February/March period was the smallest.

March 2019

The rockwall icing of March 2019 was the largest in extent of the three observed periods, as is evident in Figure 5.5, but due to the low quality of the model it was not possible to calculate a comparable ice volume. The photogrammetry model was collected after a period of approximately 10 days of negative temperatures, reaching a maximum FDH value of 445 on March 13th, which was also the day the SfM-EV model was collected. Preceding this cold period was 25 days of negative temperatures, followed by 25 days of positive temperatures, reaching an FDH value of 2225. Based on experience from the November and February/March period, one may assume that the majority of the ice that formed in this period disappeared during the 25 days of positive temperatures. However, the larger ice volume that was recorded on March 13th might imply that the ice growth was impacted by the preceding cold period. No observations were made on ice decay and collapse. On March 21st the road authorities removed ice from the rockwall (Figure 1.9, indicating the volume of the ice was considered a hazard.

November 2019

Compared to the cold period in February/March 2020, the period in November was slightly more significant both in terms of duration, continuous minus degrees, ice volume and in terms of ice falls. Also during this period the observations are sparse, and exact time of ice falls, or the exact evolution of ice growth is equivocal.

The initial growth period was mainly governed by temperatures between 0 to -5°C, lasting for about 11 days, reaching a maximum FDH value of 667. On November 12th the temperature increased to 5°C, initiating a longer period of positive temperatures. The photogrammetry model was collected the day before the initiation of positive temperatures, suggesting that the registered ice volume can be regarded as close to the maximum volume generated during the November period. The volume was calculated to 29.2 m^3, 12% larger than what was measured as a maximum during the February/March period. The larger ice extent is evident in Figure 5.5 B.

After ten days of temperatures around 0 to 5°C, the temperature increased to around 7-8°C on November 21st. Two days after, several ice falls were registered, some of which crossed the road, as photographed in Figure 5.3 A. Between the 24th and the 29th a significant amount of ice blocks collapsed into the road shoulder. Figure 5.3 B shows photos of the same section of the rock cut on the 24th and the 29th, indicating a significant decrease due to ice falls during this period. Ice falls may indeed have occurred before the 23rd of February. However, as the road shoulder is more or less free of ice on the 23rd, one may assume that the ice fall activity was low.

The ice falls that occurred during November was of a larger size and quantity than what was observed during March 2020, and with a more massive character, forming larger blocks in the road shoulder, with volumes up to 100 dm^3. Both in November and February/March the first ice falls occurred when the FDH value was close to 0. This may imply that longer, and/or colder periods of ice formation requires longer, and/or warmer periods of melt, before ice falls occur. In addition, both periods of ice falls occurred after a quick temperature increase. Based on the sparse observations, it is challenging to infer any cause to the difference in the ice fall signature. Possible impacting factors may be related to the periods of positive temperatures being of a more fluctuating character in November than that of February/March, impacting the ductility of the ice. More melt water from snow may have impacted the melting process in March, while in November no snow was available for melting. Furthermore, the rock temperature might have been higher in November than in March, due to seasonal temperature variations, impacting the intersection between the rock and ice to a larger extent in November. Certain knowledge on the precipitation is neither known, and different amounts of precipitation may have been an impacting factor. This substantiates the fact that the topic of ice falls is complex, and several other factors than temperature may be of importance.

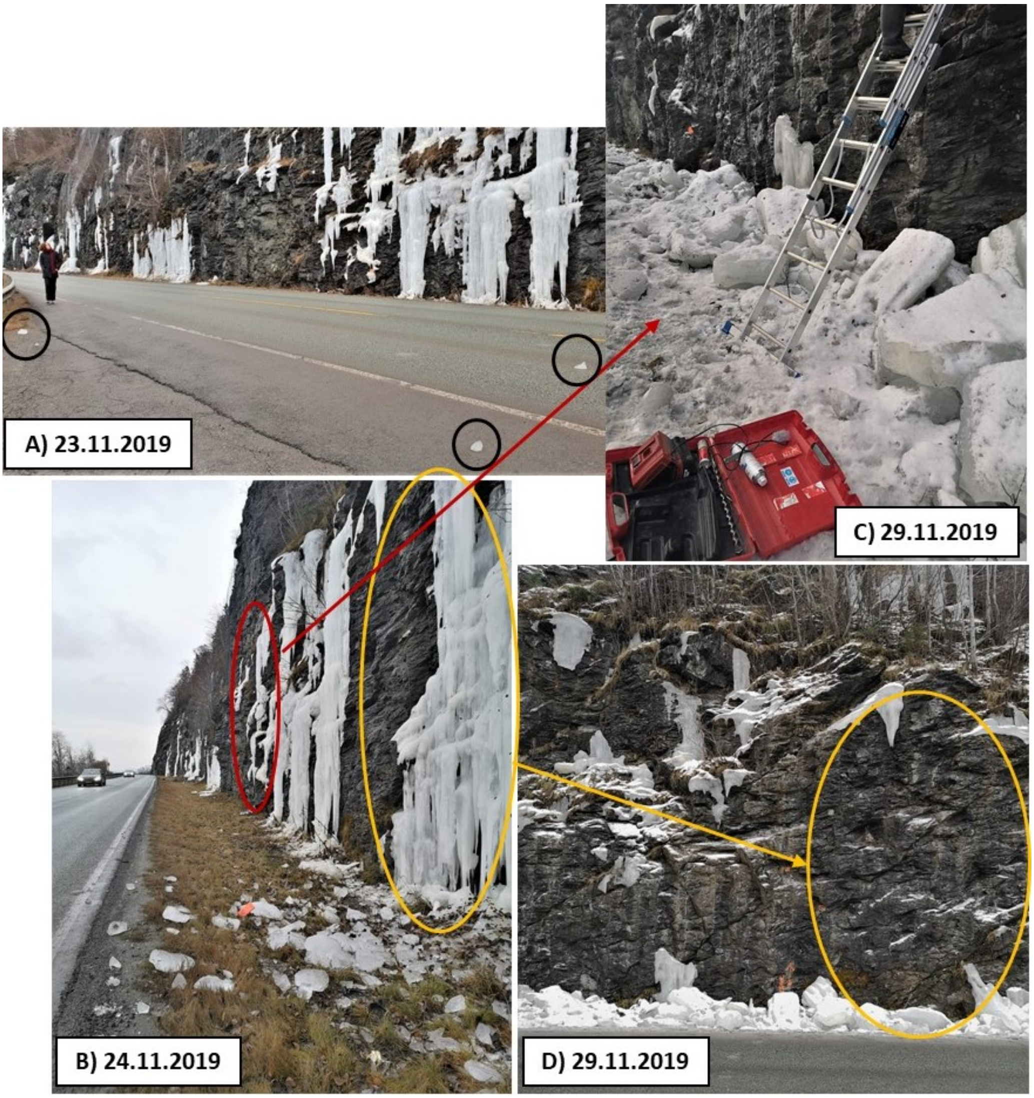

Figure 5.3: Photos shot on the 23rd, 24th and the 29th of November 2019 showing various ice blocks resulting from ice falls. A) Several ice blocks reaching the opposite side of the road. B-D) Figure B shows a small amount of ice blocks in the road shoulder, and a large amount of ice adhered to the rock. The photo is used as a reference for Figure C and D, where all the adhered ice is disappeared, and large ice blocks are present in the road shoulder. Photos: Reginals Hermanns (A) and Kari Noer Lilli (B-D).

Table 5.2: The table summarizes the observations of each ice formation period.

Period	**March 19**	**November 19**	**February/March 20**
Days of negative temperatures	11	11	6
Days between temperature increase to first registered ice fall	-	10	6
Max FDH	445	667	388
Ice volume (1=smallest, 3=largest)	3	2	1
Ice fall characteristics	-	Initiated after a fast increase in temperature (5°C/7hr). Large amount of ice blocks $\leq$ 0.5 m, one event crossed the road. Massive blocks, with relatively high strength.	Initiated after a fast increase in temperature (6.7°C/11 hr). Occurred by a combination of smaller ice falls and melt. Decayed significantly by melting before collapse. Low strength of ice blocks.

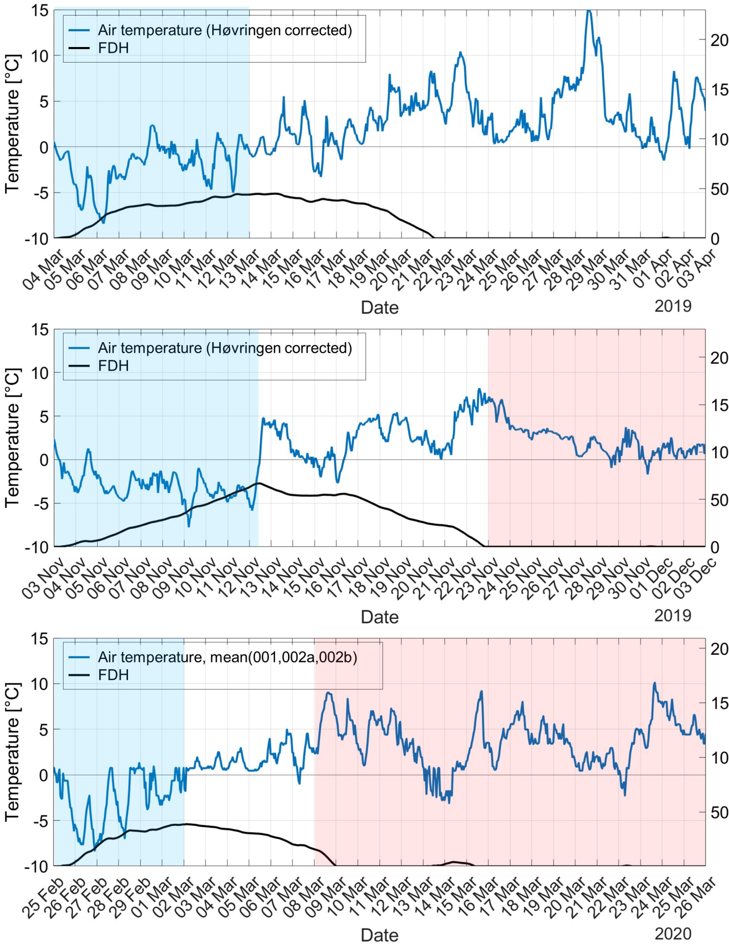

Figure 5.4: The graphs plot the air temperature and FDH for the cold period in March 2019, November 2019 and February/March 2020. The blue areas represent the length of the cold periods, where the majority of the ice is assumed to be formed. The red areas represent the initiation of ice falls, as registered in the field or by the automated camera. No data on ice falls exist from March 2019. The temperature in March 2019 and November 2019 is based on the linear temperature correlation between Høvringen weather station and the study site, as obtained in Section 4.2.2.

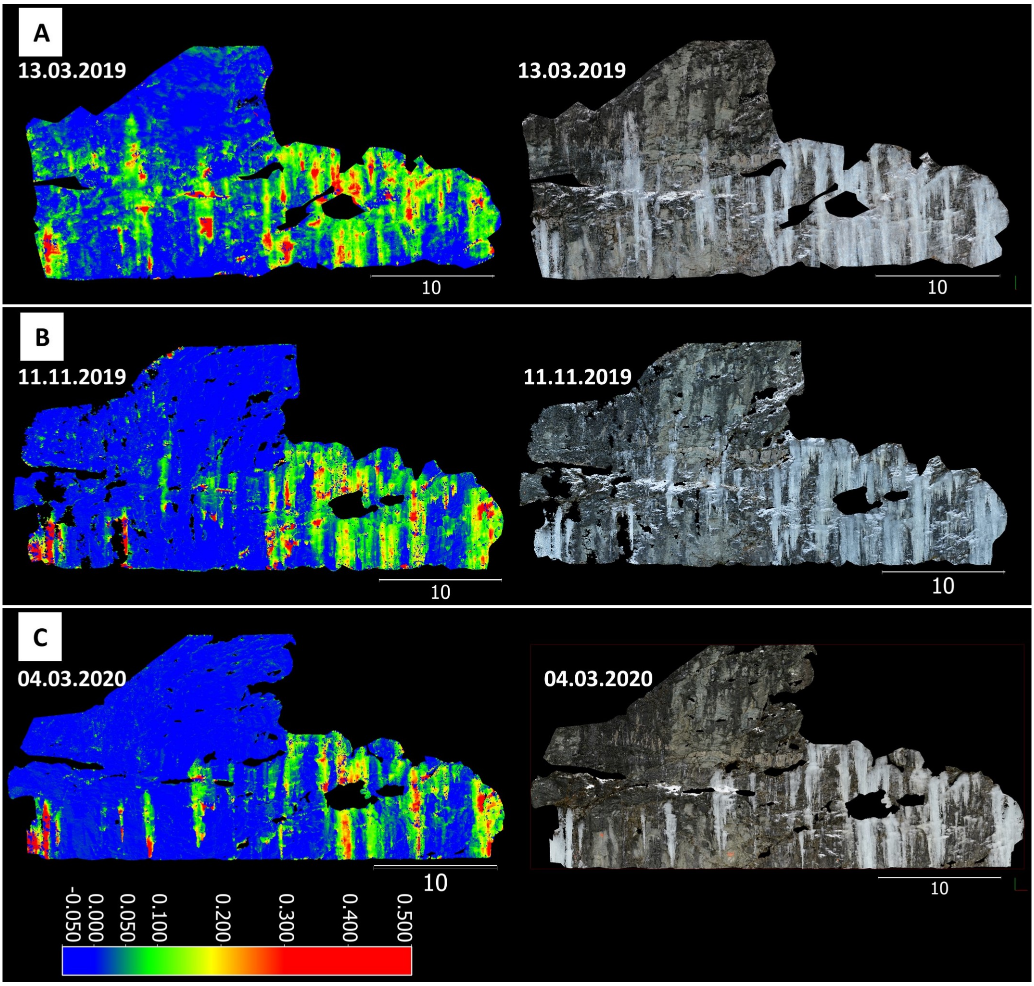

Figure 5.5: The figures present the ice extent on A) March 13th 2019, B) November 11th 2019 and C) March 4th 2020, which can be considered the approximate maximum ice extent for the three periods. The right figures show the photogrammetry models with true colors, while the left shows the cloud to mesh distances, illustrating the variation in ice extent and thickness. The largest ice extent was observed in March 2019, while February/March 2020 showed the smallest extent.

5.2.3 Ice Growth and Decay in the Past and Future

As a result of the direct correlation between rockwall icings and meteorological factors, climate change will directly impact the quantity of ice along roads, and the magnitude and frequency of ice falls. Based on the Intergovernmental Panel on Climate Change's (IPCC) emission scenario of increased anthropogenic climate emissions, the mean annual temperature in South Trøndelag is estimated to increase by 4 °C, with the largest increase during autumn, winter and spring of 4.5°C. The precipitation is expected to increase by approximately 20% in the summer, 25% in the autumn and 5% in winter and spring, towards the end of the century. The increase in precipitation will mainly occur as increased intensity and higher frequency of heavy precipitation. Days of snow are expected to decrease considerably, and periods of melting will increase as a result of increase in temperature (Hanssen-Bauer et al., 2017a,b).

Figure 5.6 plots the temperature recorded at Voll weather station, corrected by the linear correlation in Equation 4.4, during the last century until today. In addition, the freezing degree days (FDD, Equation 2.1) is plotted. It represents the same as FDH, but calculated with the mean of every day instead of hour. The annual maximum FDD is the maximum value of the FDD for each year, and has typically been applied as a measure of the severity of a winter season (Assel, 2003). Only 6 winters have had maximum FDD values lower than that of the winter of 2019/2020. Four out of these six winters occurred during the last 13 years.

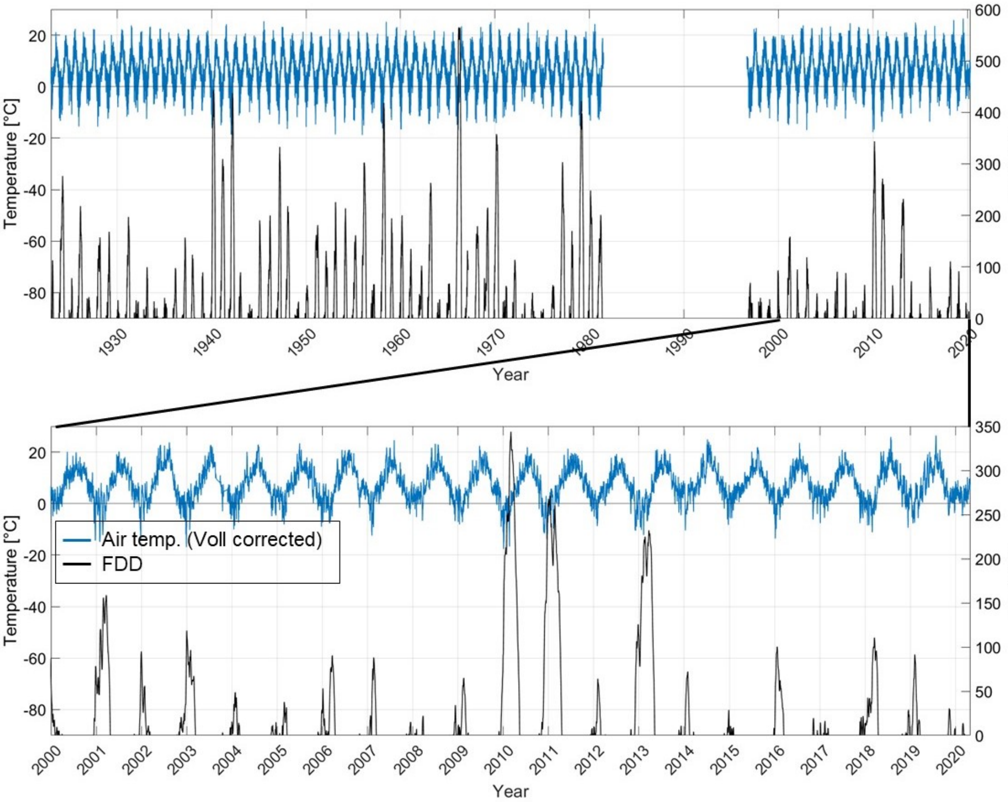

Figure 5.6: The upper graph plots the air temperature for the last century, with the corresponding FDD. The graph is based on data from Voll weather station, corrected by the linear correlation obtained in Section 4.2.2, Equation 4.4. Based on the FDD one can interpret a decrease in the severity of the winters, with an increase in short and mild winters. The lower graphs plots the last 20 years, showing large variations each winter. Only five winters during the last century have had lower maximum FDD values than the winter studied in this thesis. Four of the six winters occurred during the last 13 years. Temperature data does not exist between 1981 to 1996.

From Figure 5.6 it is apparent that there are large variations in winter severity at the study area, and the winter of 2019/2020 can be regarded a mild winter, compared to the average winters of the century. The ice formation observed during March 2019, November 2019 and February/March 2020 were all part of relatively short cold periods, with maximum FDD of 13, 18, and 29, respectively. The lowest annual FDD value throughout the century was of 18 FDD. On February 29th 2020 the FDD was 15, and the ice volume was already substantial, assessed as hazardous if detaching. Assuming the rock cut and hydrological conditions have been similar to that of today, this implies that every winter during the last century have experienced ice growth to the extent of being hazardous if detaching from the rockwall.

As observed in the study, ice can form repeatedly if the winter season has several periods of negative temperatures interfered by warmer periods of melting and detachment of the ice. A winter of alternating periods of negative and positive temperatures may thus result in more frequent ice falls, compared to persistent cold winters. An increase in liquid precipitation during the winter, as predicted by IPCC, may have a similar effect, increasing melt and possibly the ice fall frequency. On the other hand, longer periods of minus degrees may form larger volumes of ice, creating more consequential ice falls due to larger blocks.

Furthermore, the growth of ice during negative air temperatures will depend on the amount of water available for freezing. The asymptotic growth behaviour observed by Montagnat et al. (2010) and Gauthier et al. (2015a) can be related to freezing of the ground water and decrease in liquid precipitation during the period of ice formation, thus the volume will be limited by the water supply. The argument is highly relevant in Norway, leading to the geographical distribution of ice falls as was presented in Figure 1.3. As described in Section 2.1.3, areas of cold winters and little precipitation generally experience less ice formation, due to deeper frost lines. This also suggests that winters of fluctuating temperatures around 0°C may create even larger volumes of ice, compared to cold, persistent winters, as a result of the intermittent warm periods releasing water which may be available for freezing.

In addition, the severity of the intermittent warm periods are also of significance. As was observed in the study, up to several days of positive temperatures were necessary for diminishing the ice volume significantly or create ice falls. Shorter periods of plus degrees may thus not necessarily create two ice fall periods, but will only lead to a slight decay in ice volume and an increased runoff due to melt, followed by cumulative ice growth. Compared to previous studies on the same topic, one may argue that the process of ice growth and decay is more complex in Trøndelag than in Canada and the Alps, as a result of more fluctuating temperatures.

As observed from Figure 5.6 and based on IPCC's climate predictions, one may expect an increase in mild winters, with more fluctuating temperatures above and below 0°C. Based on the discussion above, this may not necessarily create less problems related to rockwall icings. Moreover, one may observe a higher frequency of ice falls, and possibly larger volumes.

5.3 Rock Fall Activity During the Winter

Mapping the road shoulder for rock fall deposits revealed four rock falls and one area of increase in colluvial soil. The results are only based on deposits of possible rock falls, and no thorough investigation of the release area could be performed. This is a slightly uncertain method, as one cannot confirm that the blocks have not been moved from other places, or derive from the slope above the rock cut. The road is frequently cleared by snow trucks during the winter, which may introduce foreign blocks. Figure 4.20A and B and the rock blocked by the rock fall net show deposits that are certainly connected to rock falls (or to soil colluvium) due to its size and appearance, while the blocks in Figure 4.20 C and D are more uncertain, as these are only singular small blocks that might have been moved.

The question of study was to evaluate how the ice growth impacts the stability of the slope and the rock fall frequency. As the known time of release for the majority of the rock falls is within time spans of several months, it is challenging to infer a certain relationship. One rock fall occurred on the 21st on February. Throughout the month of February, the temperature was mainly above zero, with some short periods of minus degrees of one to two days of duration. No precipitation was recorded at Høvringen weather station during February. The rock fall occurred on a day of positive temperatures.

Furthermore, the rock fall frequency of the summer has not been compared to the frequency of the winter. As a result, there is no data to evaluate whether the increase is larger during the winter than during the summer, throughout this season. In NVE's database, only one rockfall is registered during the summer of 2019, and one is registered during the winter of 2020, but from the winter's observations it is apparent that not all rock falls are registered.

This is however a question of statistics, and cannot be evaluated solely on one season. Figure 5.7 presents the distribution of registered rock and ice falls along a 1 km stretch of Bynesveien, covering the study area. It is apparent that more rock falls are registered during winter and spring, compared to summer and autumn. This is in agreement with previous studies on the topic (Bjerrum and Jørstad, 1968).

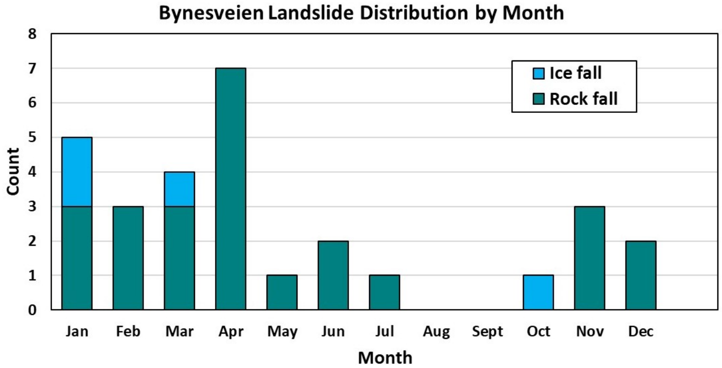

Figure 5.7: Landslide distribution throughout the year, based on data from NVE's landslide database. The data extraction corresponds to the area presented in Figure 1.10, containing 29 events over a 1 km stretch. The majority of the landslides occur during the winter and spring.

As noted in Section 2.1.7, research indicates that the rock fall probability increases during the melt and thaw season (Bjerrum and Jørstad, 1968; Macciotta et al., 2015; Matsuoka and Sakai, 1999), and can be correlated to the number of freeze thaw cycles during a winter (Pratt et al., 2019). Based on this, the winter of 2019/2020 can be characterized as a winter of high rock fall probability. The frost cycles did however result in short frost intrusions in the rock, only impacting the outermost rock.

5.4 Further Work

This thesis is an initial study on rockwall icings. With only one study on the topic of rockwall icings published previously in Norway (Norem, 1998), a large amount of work remains before a proper understanding of the growth and collapse of rockwall icings can be established. Following is a summary of recommendations on further work.

- Further gathering and analysis of data on the ice volume evolution in correlation to air temperature. The data presented in this thesis is limited both in time and amount of data, and further work would benefit from a better statistical basis.
- Investigation of the influence from other parameters than temperature, such as precipitation and water supply, wind speed and wind direction, solar radiation, humidity and slope aspect and angle.
- Geographical variation - The study is limited geographically, as only a short road section has been studied. Expanding the area of study may particularly allow for studying areas of different sun radiation, and different slope angles.
- Study on ice fall protection and its effect on reduction of ice falls. During the study it was observed that the ice fall nets gathered ice more quickly than the rock, due to the different thermal properties of the net and due to the anchoring fish net appearance. It was also observed that the ice melted more quickly on the nets. Further investigation on the appropriateness of nets, and possible other mitigation measures for reducing ice falls may aid in decreasing the costs related to road maintenance.
- In this study it was also attempted to apply a thermal camera to detect the temperature of the ice and the rock. The results were not included due to time constraints, but were of interest and may further work may aid in understanding the heat fluxes of the various surfaces.

Chapter 6

Conclusions

- **Ice Growth:** Ice forms directly after the initiation of negative temperatures, initially creating a thin ice crust and stalactites, merging into larger ice columns and ice sheets. The ice growth of February/March 2020 increased linearly during negative temperatures. After five days its volume was evaluated as being potentially hazardous if detaching. The ice thickness continued to increase slightly for around three days of positive temperatures, inferring that the ice growth is not only dependent on the temperature of the air and rock. Impact from nocturnal radiation was suggested, but must be studied further. The ice reached a maximum volume of approximately 25 m^3 after seven days. The ice volume of November 2019 summed to 29 m^3 after 11 days of negative temperatures indicating a slower growth or an asymptotic development in ice volume after a certain time.
- **Ice Decay:** In February/March 2020 the decay of the rockwall icing occurred by a combination of melting and small ice falls, which was initiated after a period of six days of positive temperatures. In November 2019 the decay occurred by larger ice falls of up to 100 dm^3, with some reaching the road, initiated after approximately 11 days of positive temperatures. In both periods, the first ice falls were initiated after a quick temperature increase and when the FDH was close to zero. The ice falls occurred by a combination of falls, toppling and sliding, with the surface of rupture mainly being at the rock/ice boundary.
- **Rock Temperature:** During the February/March 2020 period, the ice isolates the rock from changes in air temperature, resulting in rock temperatures above 0°C throughout the period of ice coverage. This suggests that the ice is not adhered to the rock wall by being frozen to the rock, but rather by friction between the rock/ice boundary.
- **Limitations:** The growth and decay of rockwall icings cannot be explained solely by changes in temperature. The impacting role of factors such as hydrology and water supply, water temperature, precipitation, wind speed and wind direction and solar irradiation have not been studied thoroughly, and a quantification of these factors will contribute to an increased understanding of the evolution of rockwall icings. The amount of data are

limited as only one period of ice formation and decay was thoroughly studied, and further collection of data is necessary to have a better statistical basis.

- **Climate Change:** Temperature data from 1923 until today show a large variation in the severity of the winters, and a trend towards shorter and warmer winters is apparent. Only five winters during the last century have had cold periods as short and comparable warm as the winter of 2019/2020, with four of the six winters occurring during the last 13 years. It is furthermore suggested that increased fluctuations from below 0°C to above 0°C due to climate change, and increased precipitation may increase the ice fall frequency.
- **Study Site Correlation to Weather Stations**: Temperature records from nearby weather stations generally record slightly higher temperatures than what is recorded at the study area. The coefficient of determination (R^2) show a good correlation between the study area and nearby weather stations, and the data are regarded applicable for describing the general evolution of temperature at the study site.
- **Rock Falls:** Four rock falls were registered along the 340 m long stretch during the winter. Only one was registered by the road authorities, revealing a bias in registrations. Statistics from the site show a trend of higher rock fall activity during the winter and spring, implying that the impact of freeze-thaw processes largely influence the stability of the slope.
- **Applicability of Structure from Motion:** The method of Structure from Motion with the use of a DSLR camera is regarded suitable for detecting changes in the rockwall icing. A large amount of icicles will degrade the quality of the model. Due to high contrasts between the ice and the rock, optimal camera settings are crucial for obtaining models of high quality. With optimal settings and thorough manual adjustments, a precision of 5-7 cm was obtained. The method of Structure from Motion with action cameras mounted on a moving car did not provide satisfactory results, as two of four models were not reconstructed correctly. As the ice growth occurs on a small scale, a method of higher accuracy is recommended.

References

Abellán, A., J. M. Vilaplana, J. Calvet, D. García-Sellés, and E. Asensio (2011). Rockfall monitoring by Terrestrial Laser Scanning - Case study of the basaltic rock face at Castellfollit de la Roca (Catalonia, Spain). *Natural Hazards and Earth System Science*, 11.3, pp. 829–841.

Adresseavisen (2012). Her er de mest rasutsatte veiene. URL: %7Bhttps://www.adressa.no/nyheter/article578443.ece%7D (visited on 05/30/2020).

Adresseavisen (2020). Planlegger tunnel mellom Ila og Flakk. URL: %7Bhttps://www.adressa.no/pluss/nyheter/2020/05/28/Planlegger-tunnel-mellom-Ila-og-Flakk-21933586.ece?rs1820011590820842842&t=1%7D (visited on 05/30/2020).

Alfredsen, K., C. Haas, J. A. Tuhtan, and P. Zinke (2018). Brief Communication: Mapping river ice using drones and structure from motion. *Cryosphere*, 12.2, pp. 627–633.

Alvestad, E. (2016). Analyse av faren for fjellskred/steinsprang langs Fv 715 Trolla-Flakk (Bynesveien). Master Thesis, NTNU.

Arnhardt, C. and Smith (2016). A new assessment method for structural-control failure mechanisms in rock slopes — case examples. *AIMS Geosciences*, 2.3, pp. 214–230.

Assel, R. A. (2003). Great lakes monthly and seasonal accumulations of freezing degree-days - Winters 1898-2002, pp. 1–15.

Bemis, S. P., S. Micklethwaite, D. Turner, M. R. James, S. Akciz, S. T. Thiele, and H. A. Bangash (2014). Ground-based and UAV-Based photogrammetry: A multi-scale, high-resolution mapping tool for structural geology and paleoseismology. *Journal of Structural Geology*, 69, pp. 163–178.

Bianchi, A. (2004). Frozen waterfalls : how they develope how they collapse. *IFMGA, Union Internationale des Associations de Guide de Montagne*, Unpublished.

Bjerrum, L. and F. A. Jørstad (1968). Stability of rock slopes in Norway. nr 79. Oslo: Norges Geotekniske Institutt.

Brasington, J., J. Langham, and B. Rumsby (2003). Methodological sensitivity of morphometric estimates of coarse fluvial sediment transport. *Geomorphology*, 53.3-4, pp. 299–316.

Davies, M., O. Hamza, B. Lumsden, and C. Harris (2000). Laboratory measurement of the shear strength of ice-filled rock joints. *Annals of Glaciology*, 31, pp. 463–467.

Davies, M., O. Hamza, and C. Harris (2001). The effect of rise in mean annual temperature on the stability of rock slopes containing ice-filled discontinuities. *Permafrost and periglacial processes*, 12, pp. 137–144.

Douglas, G. R. (1980). Magnitude frequency study of rockfall in Co. Antrim, N. Ireland. *Earth Surface Processes*, 5, pp. 123–129.

Fonstad, M. A., J. T. Dietrich, B. C. Courville, J. L. Jensen, and P. E. Carbonneau (2013). Topographic structure from motion: A new development in photogrammetric measurement. *Earth Surface Processes and Landforms*, 38, pp. 421–430.

Fossen, H., R. Pedersen, S. Bergh, and A. Arild (2013). “En fjellkjede blir til”. Landet blir til: Norges geologi. 2. utg. Trondheim: Norsk geologisk forening. Chap. 6, pp. 180–233.

Gale, G. H. and D. Roberts (1974). Trace element geochemistry of norwegian lower palaeozoic basic volcanics and its tectonic implications. *Earth and Planetary Science Letters*, 22, pp. 380–390.

Gauthier, F., M. Allard, and B. Hétu (2015a). Ice wall growth and decay: Meteorological analysis and modelling. *Permafrost and Periglacial Processes*, 26, pp. 84–102.

Gauthier, F., B. Hétu, and M. Allard (2015b). Forecasting method of ice blocks fall using logistic model and melting degree–days calculation: a case study in northern Gaspésie, Québec, Canada. *Natural Hazards*, 79, pp. 855–880.

Gauthier, F., M. Montagnat, J. Weiss, M. Allard, and B. Hétu (2013). Ice cascade growth and decay: A thermodynamic approach. *Journal of Glaciology*, 59.215, pp. 507–523.

Gauthier, F. (2008). Les glaces de paroi: Formation, écroulement et impact géomorphologique. Master Thesis, Université du Québec INRS.

Gauthier, F. (2013). Les glaces de paroi: Glaciologie, thermodynamique et prévision des chutes de blocs de glace sur les routes du nord de la Gaspésie. PhD Thesis, Université Laval.

Gauthier, F., B. Hétu, and N. Bergeron (Nov. 2012). Analyses statistiques des conditions climatiques propices aux chutes de blocs de glace dans les corridors routiers du nord de la Gaspésie, Québec, Canada. *Canadian Geotechnical Journal*, 49, pp. 1408–1426.

Gómez-Gutiérrez, Á., J. J. de Sanjosé-Blasco, J. de Matías-Bejarano, and F. Berenguer-Sempere (2014). Comparing two photo-reconstruction methods to produce high density point clouds and DEMs in the Corral del Veleta Rock Glacier (Sierra Nevada, Spain). *Remote Sensing*, 6.6, pp. 5407–5427.

Graveline, M. H. and D. Germain (2016). Ice-block fall and snow avalanche hazards in northern Gaspésie (eastern Canada): Triggering weather scenarios and process interactions. *Cold Regions Science and Technology*, 123, pp. 81–90.

Hamberg, I., J. S. E. M. Svensson, T. S. Eriksson, C.-G. Granqvist, P. Arrenius, and F. Norin (1987). Radiative cooling and frost formation on surfaces with different thermal emittance: theoretical analysis and practical experience. *Applied Optics*, 26.11, p. 2131.

Hanssen-Bauer, I., E. Førland, I. Haddeland, H. Hisdal, S. Mayer, A. Nesje, J. Nilsen, S. Sandven, A. Sandø, A. Sorteberg, and B. Ådlandsvik (2017a). Klima i Norge 2100 - A knowledge base for climate adaptation. Tech. rep. 1. Norsk Klimaservicesenter, p. 204. URL: www.miljodirektoratet.no/20804.

Hanssen-Bauer, I., E. Førland, I. Haddeland, H. Hisdal, S. Mayer, A. Nesje, J. Nilsen, S. Sandven, A. Sandø, A. Sorteberg, and B. Ådlandsvik (2017b). Klimaprofil Sør-Trøndelag. Tech. rep. Norsk Klimaservicesenter.

Hinkel, K. (1983). Ice-cover growth rates at nearshore locations in the Great Lakes. Tech. rep. Michigan.

Jaboyedoff, M., T. Oppikofer, A. Abellán, M. H. Derron, A. Loye, R. Metzger, and A. Pedrazzini (2012). Use of LIDAR in landslide investigations: A review. *Natural Hazards*, 61.1, pp. 5–28.

James, M. R. and S. Robson (2012). Straightforward reconstruction of 3D surfaces and topography with a camera: Accuracy and geoscience application. *Journal of Geophysical Research: Earth Surface*, 117.3, pp. 1–17.

Kenner, R., M. Phillips, C. Danioth, C. Denier, P. Thee, and A. Zgraggen (2011). Investigation of rock and ice loss in a recently deglaciated mountain rock wall using terrestrial laser scanning: Gemsstock, Swiss Alps. *Cold Regions Science and Technology*, 67.3, pp. 157–164.

Krautblatter, M., D. Funk, and F. K. Günzel (2013). Why permafrost rocks become unstable: A rock-ice-mechanical model in time and space. *Earth Surface Processes and Landforms*, 38, pp. 876–887.

Lane, S. N., T. D. James, and M. D. Crowell (2000). Application of digital photogrammetry to complex topography for geomorphological research. *Photogrammetric Record*, 16.95, pp. 793–821.

Lato, M. J., D. Jean Hutchinson, D. Gauthier, T. Edwards, and M. Ondercin (2015). Comparison of airborne laser scanning, terrestrial laser scanning, and terrestrial photogrammetry for mapping differential slope change in mountainous terrain. *Canadian Geotechnical Journal*, 52.2, pp. 129–140.

Liereng, A. (2016). Iskjøving i grøfter og skjæringer langs veg og jernbane. Master thesis, NTNU.

Lilli, K. N. (2019). Ice growth and collapse along road cuts - an initial case study from Trøndelag. Specialization report (Unpublished), pp. 1–49.

Lim, M., D. N. Petley, N. J. Rosser, R. J. Allison, A. J. Long, and D. Pybus (2005). Combined digital photogrammetry and time-of-flight laser scanning for monitoring cliff evolution. *Photogrammetric Record*, 20.110, pp. 109–129.

Lowe, J. (1996). Ice world: techniques and experiences of modern ice climbing. 1st ed. Calgary: The Mountaineers.

Macciotta, R., C. D. Martin, T. Edwards, D. M. Cruden, and T. Keegan (2015). Quantifying weather conditions for rock fall hazard management. *Georisk*, 9.3, pp. 171–186.

Maeno, N., L. Makkonen, K. Nishimura, K. Kosugi, and T. Takahashi (1994). Growth rates of icicles. *Journal of Glaciology*, 40, pp. 319–326.

Makkonen, L. (1988). A model of icicle growth. *Journal of Glaciology*, 34, pp. 64–70.

Mallalieu, J., J. L. Carrivick, D. J. Quincey, M. W. Smith, and W. H. James (2017). An integrated Structure-from-Motion and time-lapse technique for quantifying ice-margin dynamics. *Journal of Glaciology*, 63.242, pp. 937–949.

Matsuoka, N. (1994). Diurnal freeze–thaw depth in rockwalls: Field measurements and theoretical considerations. *Earth Surface Processes and Landforms*, 19, pp. 423–435.

Matsuoka, N. and J. Murton (2008). Frost weathering: recent advances and future directions. *Permafrost and periglacial processes*, 19, pp. 195–210.

Matsuoka, N. and H. Sakai (1999). Rockfall activity from an alpine cliff during thawing periods. *Geomorphology*, 28, pp. 309–328.

Montagnat, M., J. Weiss, B. Cinquin-Lapierre, P. A. Labory, L. Moreau, F. Damilano, and D. Lavigne (2010). Waterfall ice: Formation, structure and evolution. *Journal of Glaciology*, 56, pp. 225–234.

NGU (n.d). Løsmassekart. URL: http://geo.ngu.no/kart/losmasse/.

Norem, H. (1998). Sikring av vegar mot isras : årsaker til isras, samling av erfaringer, utføring av sikringstiltak. Statens Vegvesen.

Norsk Klimaservicesenter (n.d). Månedlige temperaturobservasjoner Trondheim - Voll, 1997-2018. URL: https://klimaservicesenter.no/observations/ (visited on 10/11/2019).

NRK (2013). Mann omkom i isras. URL: %7Bhttps://www.nrk.no/nordland/mann-omkom-i-isras-1.11431366%7D (visited on 05/30/2020).

NVE (n.d). NVE Skredhendelser. URL: https://gis3.nve.no/link/?link=SkredHendelser (visited on 04/24/2020).

Optech (n.d.). ILRIS Terrestrial Laser Scanner. URL: http://www.optech.ca/pdf/ILRIS_SpecSheet_110309_Web.pdf.

Patton, A. I., S. L. Rathburn, and D. M. Capps (2019). Landslide response to climate change in permafrost regions. *Geomorphology*, 340, pp. 116–128.

Piermattei, L., L. Carturan, and A. Guarnieri (2015). Use of terrestrial photogrammetry based on structure-from-motion for mass balance estimation of a small glacier in the Italian alps. *Earth Surface Processes and Landforms*, 40, pp. 1791–1802.

Pratt, C., R. Macciotta, and M. Hendry (2019). Quantitative relationship between weather seasonality and rock fall occurrences north of Hope, BC, Canada. *Bulletin of Engineering Geology and the Environment*, 78.5, pp. 3239–3251.

Rao, S. S. (Jan. 2011). "Formulation and solution procedure". The finite element method in engineering. Butterworth-Heinemann. Chap. 13, pp. 473–487.

Schwind, M. and M. Starek (2017). Structure-from-motion photogrammetry. *GIM International*, 31, pp. 36–39.

Smith, J. L. Carrivick, and D. J. Quincey (2016). Structure from motion photogrammetry in physical geography. *Progress in Physical Geography*, 40, pp. 247–275.

Solli, A., T. Grenne, T. Slagstad, and D. Roberts (2003). Berggrunnskart Trondheim 1621 IV, M 1:50 000. Norges geologiske undersøkelse.

Sonntag, R. E. and C. Borgnakke (2013). Fundamentals of thermodynamics. 8th ed. Weinheim, Germany: Wiley.

Statens vegvesen (n.d). Vegkart (Trafikkmengde). URL: https://www.vegvesen.no/nvdb/vegkart/v2/%7B%5C#%7Dkartlag:geodata/@600000,7225000,3 (visited on 12/10/2019).

Statistisk Sentralbyrå (2019). Befolkningsstatistikk på kart. URL: https://kart.ssb.no/befolkning (visited on 01/31/2020).

Sturzenegger, M. and D. Stead (2009). Close-range terrestrial digital photogrammetry and terrestrial laser scanning for discontinuity characterization on rock cuts. *Engineering Geology*, 106.3-4, pp. 163–182.

Voumard, J., A. Abellán, P. Nicolet, I. Penna, M. A. Chanut, M. H. Derron, and M. Jaboyedoff (2017). Using street view imagery for 3-D survey of rock slope failures. *Natural Hazards and Earth System Sciences*, 17.12, pp. 2093–2107.

Voumard, J., M. H. Derron, M. Jaboyedoff, P. Bornemann, and J. P. Malet (2018). Pros and cons of structure for motion embarked on a vehicle to survey slopes along transportation lines using 3D georeferenced and coloured point clouds. *Remote Sensing*, 10.11, pp. 1–28.

Walpole, R., R. Myers, S. Myers, and K. Ye (2016). Probability & statistics for engineers and scientists. 9th ed. Harlow: Pearson Education.

Weiss, J., M. Montagnat, B. Cinquin-Lapierre, P. A. Labory, L. Moreau, F. Damilano, and D. Lavigne (2011). Waterfall ice: Mechanical stability of vertical structures. *Journal of Glaciology*, 57, pp. 407–415.

Westoby, M. J., J. Brasington, N. F. Glasser, M. J. Hambrey, and J. M. Reynolds (2012). 'Structure-from-Motion' photogrammetry: A low-cost, effective tool for geoscience applications. *Geomorphology*, 179, pp. 300–314.

Whitehead, K., B. J. Moorman, and C. H. Hugenholtz (2013). Brief Communication: Low-cost, on-demand aerial photogrammetry for glaciological measurement. *Cryosphere*, 7.6, pp. 1879–1884.

Wilkinson, M. W., R. R. Jones, C. E. Woods, S. R. Gilment, K. J. McCaffrey, S. Kokkalas, and J. J. Long (2016). A comparison of terrestrial laser scanning and structure-frommotion photogrammetry as methods for digital outcrop acquisition. *Geosphere*, 12, pp. 1865–1880.

Wyllie, D. C. and C. W. Mah (2004). Rock Slope Engineering. 4th ed. Spon Press Taylor & Francis Group.

Appendix

A Position of Temperature Loggers

Temperature logger 411a and 411b

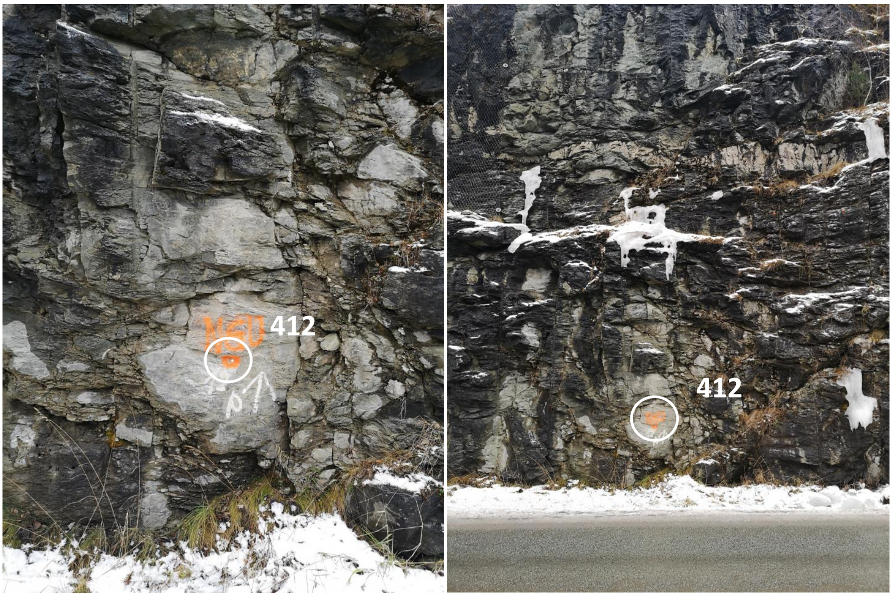

Temperature logger 413 and 414

Temperature logger 415 and 416

Temperature logger 417 and 418

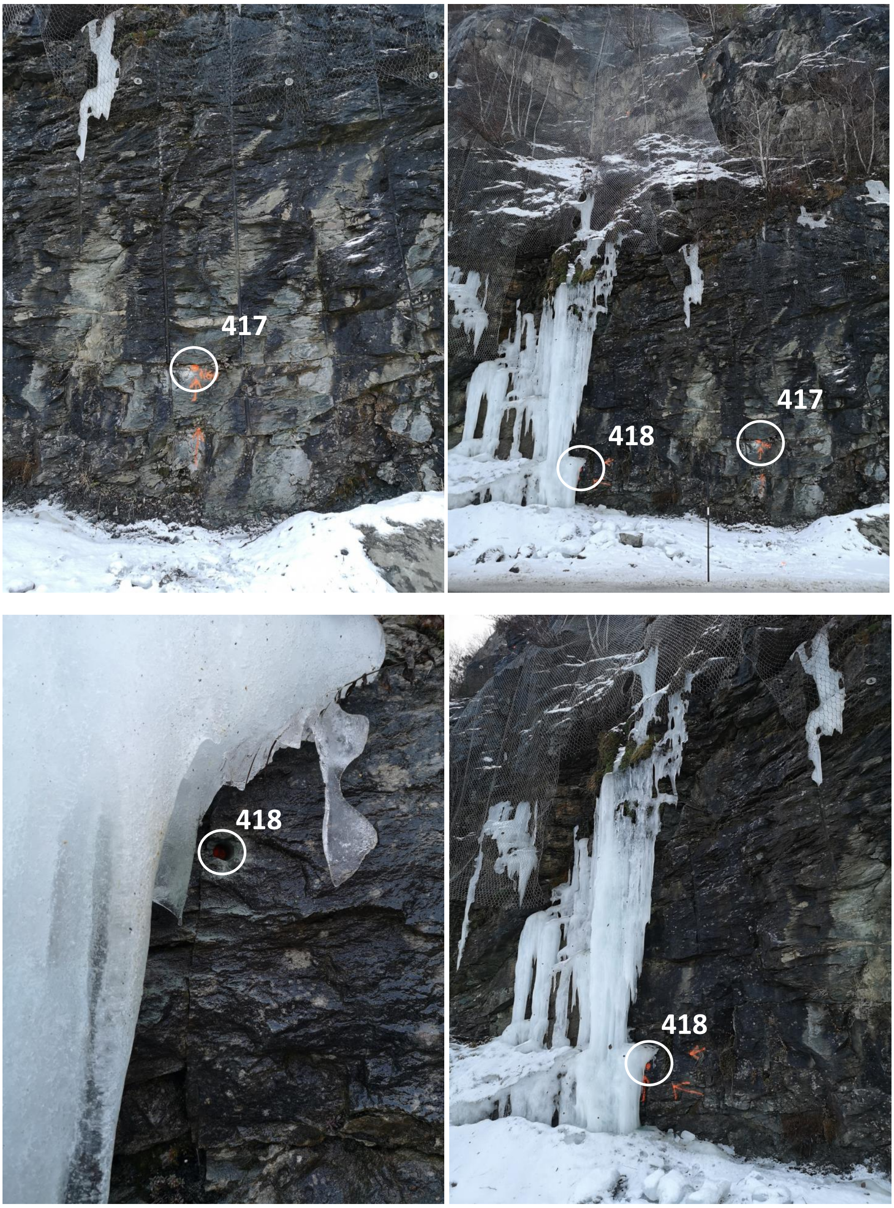

B Rock Temperature Measurements

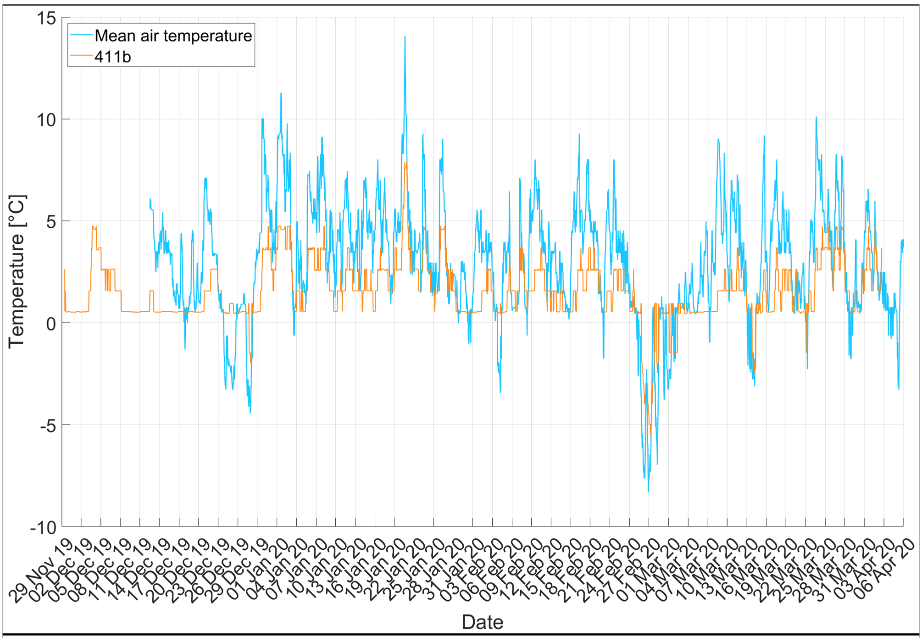

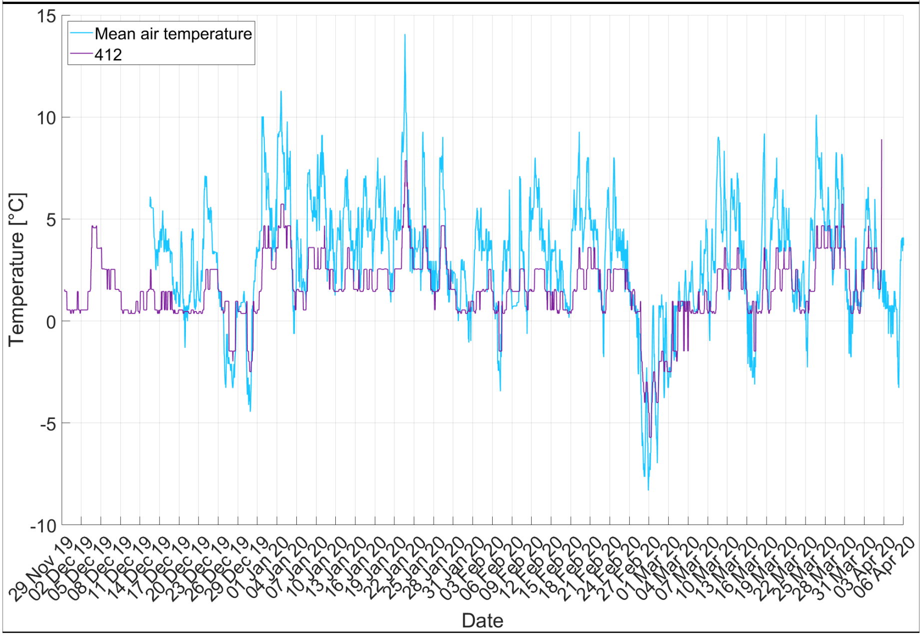

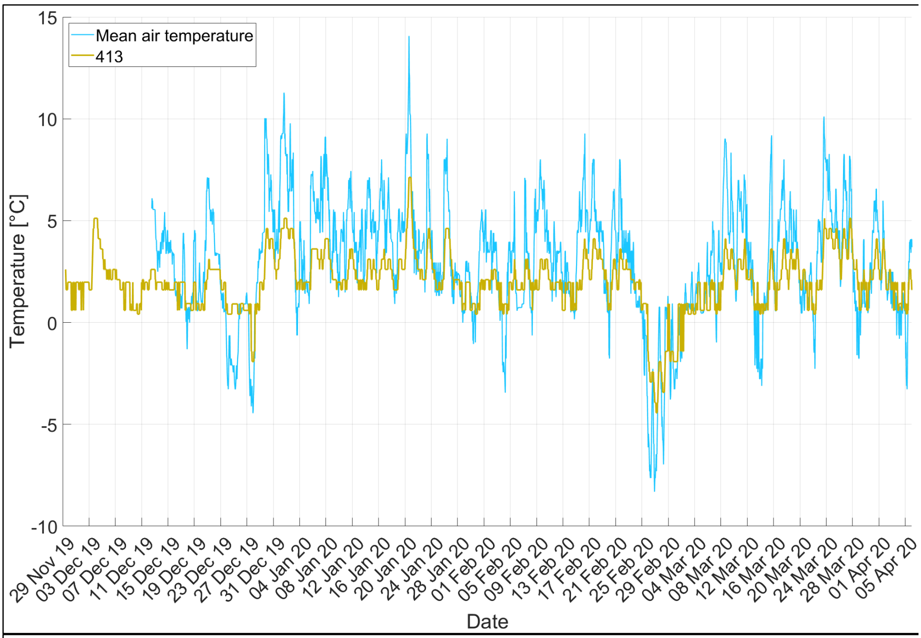
Mean air temperature
413
Temperature [°C]
15
10
5
0
-5
-10
29 Nov 19
03 Dec 19
07 Dec 19
11 Dec 19
15 Dec 19
19 Dec 19
23 Dec 19
27 Dec 19
31 Dec 19
04 Jan 20
08 Jan 20
12 Jan 20
16 Jan 20
20 Jan 20
24 Jan 20
28 Jan 20
01 Feb 20
05 Feb 20
09 Feb 20
13 Feb 20
17 Feb 20
21 Feb 20
25 Feb 20
29 Feb 20
04 Mar 20
08 Mar 20
12 Mar 20
16 Mar 20
20 Mar 20
24 Mar 20
28 Mar 20
01 Apr 20
05 Apr 20
Date

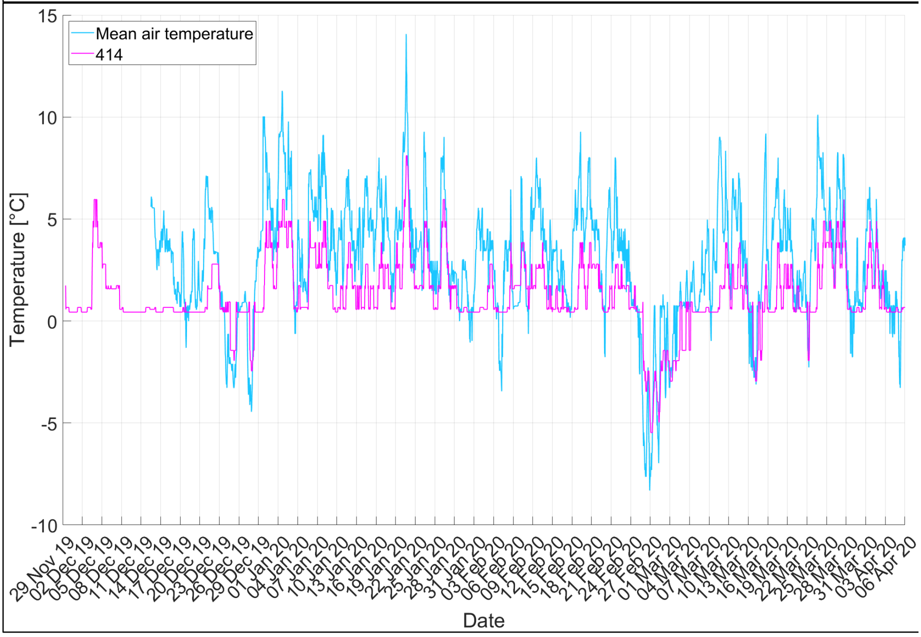
Mean air temperature
414
Temperature [°C]
15
10
5
0
-5
-10
29 Nov 19
02 Dec 19
05 Dec 19
08 Dec 19
11 Dec 19
14 Dec 19
17 Dec 19
20 Dec 19
23 Dec 19
26 Dec 19
29 Dec 19
01 Jan 20
04 Jan 20
07 Jan 20
10 Jan 20
13 Jan 20
16 Jan 20
19 Jan 20
22 Jan 20
25 Jan 20
28 Jan 20
31 Jan 20
03 Feb 20
06 Feb 20
09 Feb 20
12 Feb 20
15 Feb 20
18 Feb 20
21 Feb 20
24 Feb 20
27 Feb 20
01 Mar 20
04 Mar 20
07 Mar 20
10 Mar 20
13 Mar 20
16 Mar 20
19 Mar 20
22 Mar 20
25 Mar 20
28 Mar 20
31 Mar 20
03 Apr 20
06 Apr 20
Date

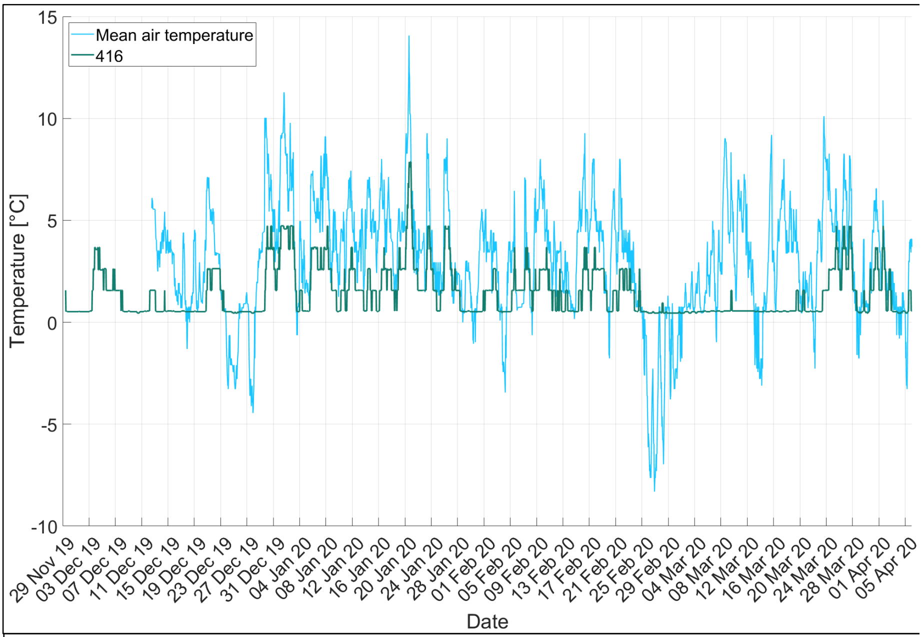
Mean air temperature
416
Temperature [°C]
15
10
5
0
-5
-10
29 Nov 19
03 Dec 19
07 Dec 19
11 Dec 19
15 Dec 19
19 Dec 19
23 Dec 19
27 Dec 19
31 Dec 19
04 Jan 20
08 Jan 20
12 Jan 20
16 Jan 20
20 Jan 20
24 Jan 20
28 Jan 20
01 Feb 20
05 Feb 20
09 Feb 20
13 Feb 20
17 Feb 20
21 Feb 20
25 Feb 20
29 Feb 20
04 Mar 20
08 Mar 20
12 Mar 20
16 Mar 20
20 Mar 20
24 Mar 20
28 Mar 20
01 Apr 20
05 Apr 20
Date

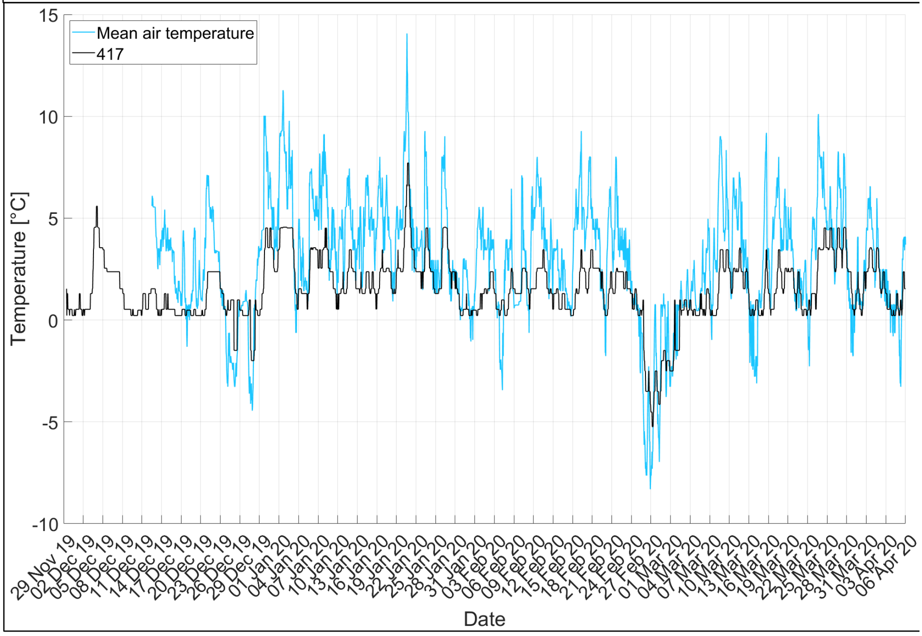
Mean air temperature
417
Temperature [°C]
15
10
5
0
-5
-10
29 Nov 19
02 Dec 19
05 Dec 19
08 Dec 19
11 Dec 19
14 Dec 19
17 Dec 19
20 Dec 19
23 Dec 19
26 Dec 19
29 Dec 19
01 Jan 20
04 Jan 20
07 Jan 20
10 Jan 20
13 Jan 20
16 Jan 20
19 Jan 20
22 Jan 20
25 Jan 20
28 Jan 20
31 Jan 20
03 Feb 20
06 Feb 20
09 Feb 20
12 Feb 20
15 Feb 20
18 Feb 20
21 Feb 20
24 Feb 20
27 Feb 20
01 Mar 20
04 Mar 20
07 Mar 20
10 Mar 20
13 Mar 20
16 Mar 20
19 Mar 20
22 Mar 20
25 Mar 20
28 Mar 20
31 Mar 20
03 Apr 20
06 Apr 20
Date

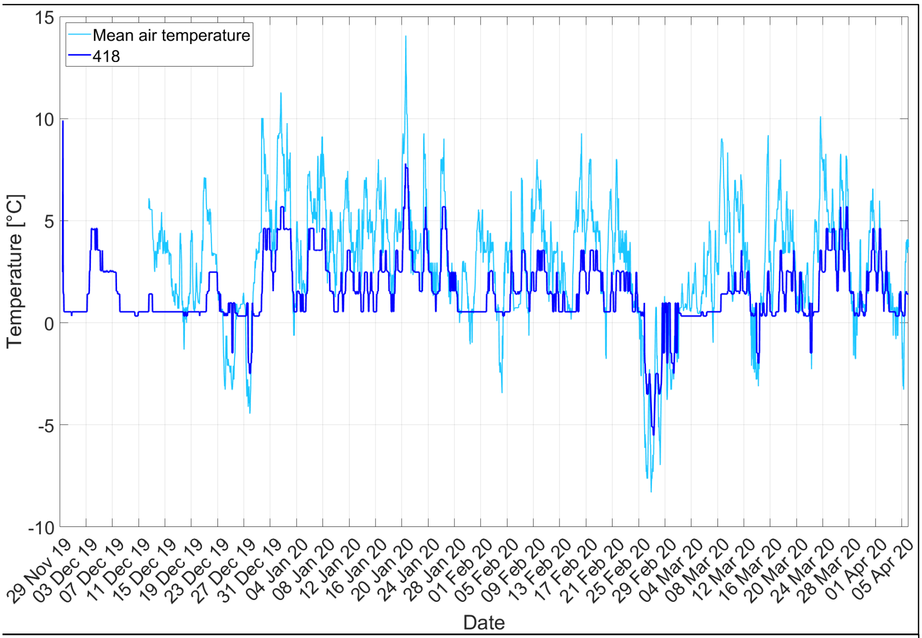
Mean air temperature
418
Temperature [°C]
15
10
5
0
-5
-10
29 Nov 19
03 Dec 19
07 Dec 19
11 Dec 19
15 Dec 19
19 Dec 19
23 Dec 19
27 Dec 19
31 Dec 19
04 Jan 20
08 Jan 20
12 Jan 20
16 Jan 20
20 Jan 20
24 Jan 20
28 Jan 20
01 Feb 20
05 Feb 20
09 Feb 20
13 Feb 20
17 Feb 20
21 Feb 20
25 Feb 20
29 Feb 20
04 Mar 20
08 Mar 20
12 Mar 20
16 Mar 20
20 Mar 20
24 Mar 20
28 Mar 20
01 Apr 20
05 Apr 20
Date

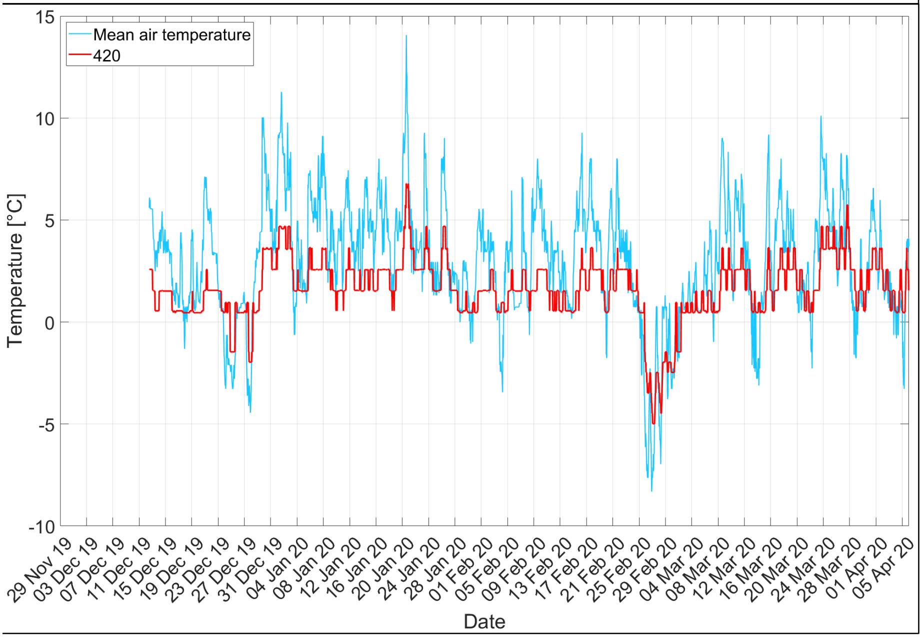
Mean air temperature
420
Temperature [°C]
15
10
5
0
-5
-10
29 Nov 19
03 Dec 19
07 Dec 19
11 Dec 19
15 Dec 19
19 Dec 19
23 Dec 19
27 Dec 19
31 Dec 19
04 Jan 20
08 Jan 20
12 Jan 20
16 Jan 20
20 Jan 20
24 Jan 20
28 Jan 20
01 Feb 20
05 Feb 20
09 Feb 20
13 Feb 20
17 Feb 20
21 Feb 20
25 Feb 20
29 Feb 20
04 Mar 20
08 Mar 20
12 Mar 20
16 Mar 20
20 Mar 20
24 Mar 20
28 Mar 20
01 Apr 20
05 Apr 20
Date

C Photogrammetry Models - Cloud to Mesh Distances

Reference models, 03.10.2019:

DSLR

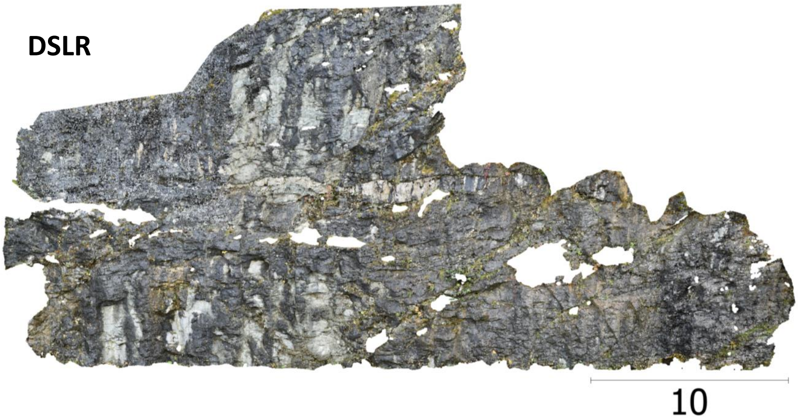

Action Camera

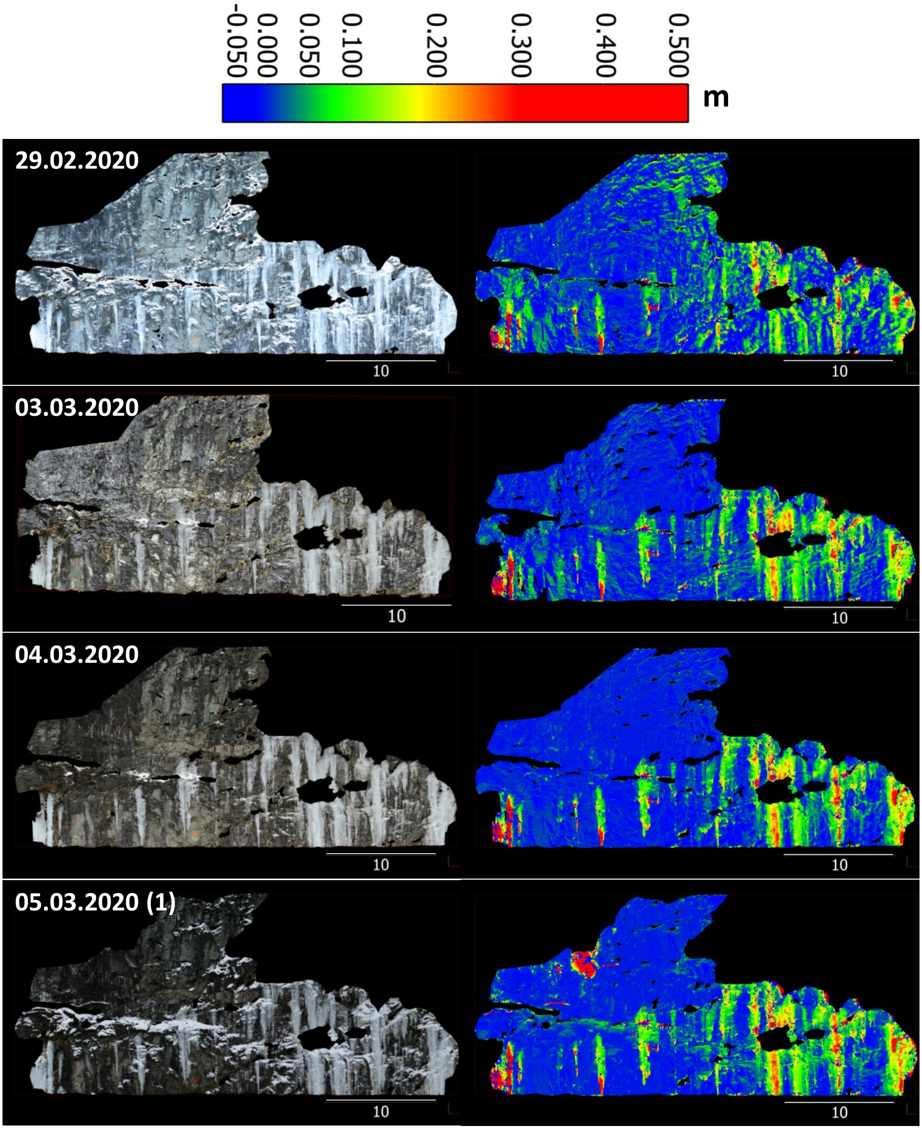
-0.050
0.000
0.050
0.100
0.200
0.300
0.400
0.500
m
29.02.2020
03.03.2020
04.03.2020
05.03.2020 (1)
10

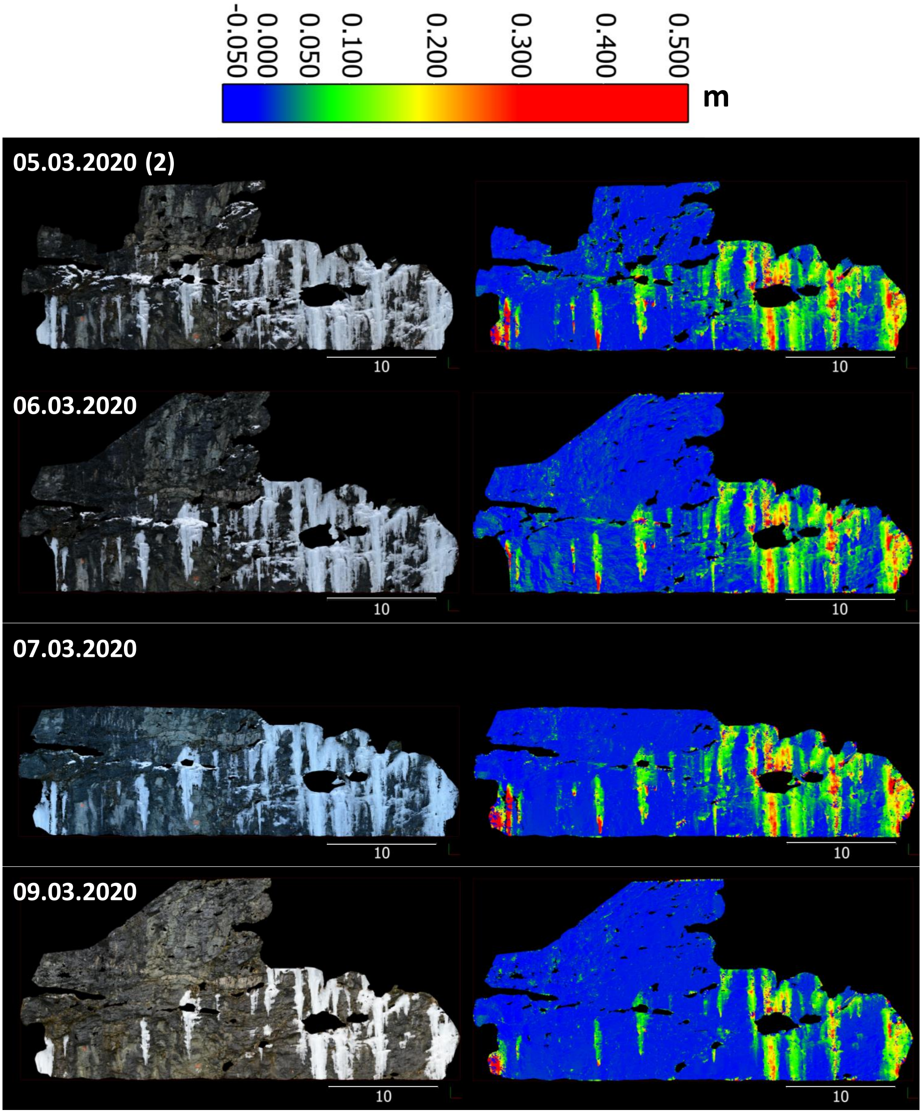
-0.050
0.000
0.050
0.100
0.200
0.300
0.400
0.500
m
05.03.2020 (2)
10
10
06.03.2020
10
10
07.03.2020
10
10
09.03.2020
10
10

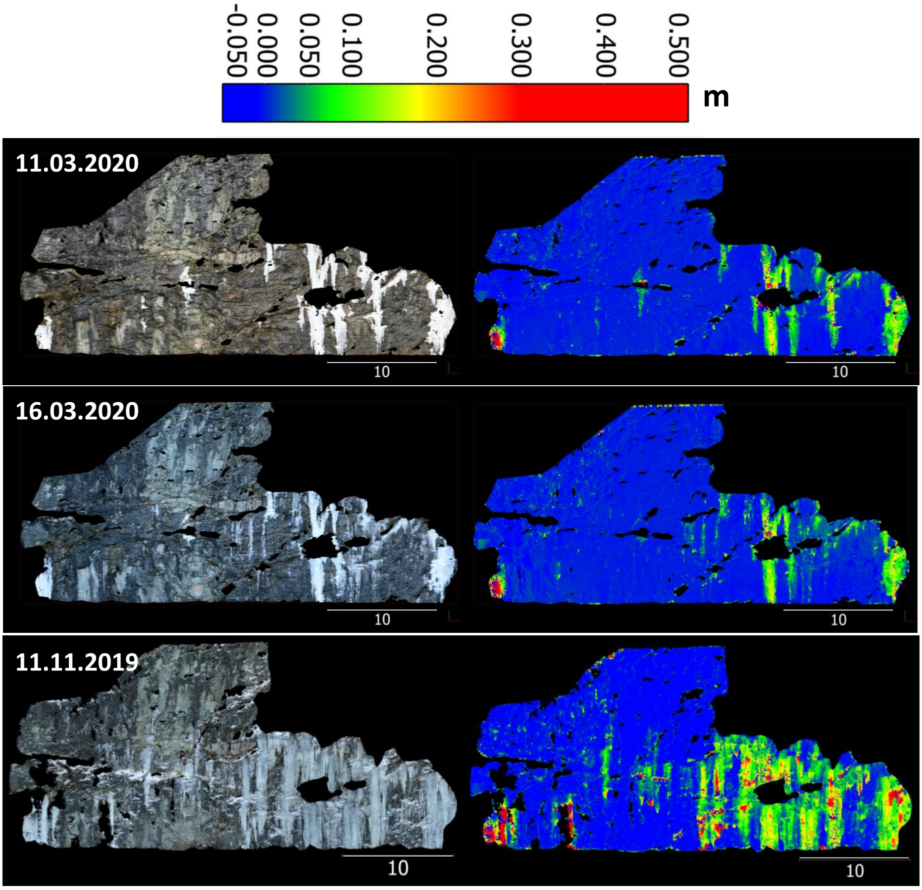
-0.050
0.000
0.050
0.100
0.200
0.300
0.400
0.500
m
11.03.2020
10
10
16.03.2020
10
10
11.11.2019
10
10

13.03.2019

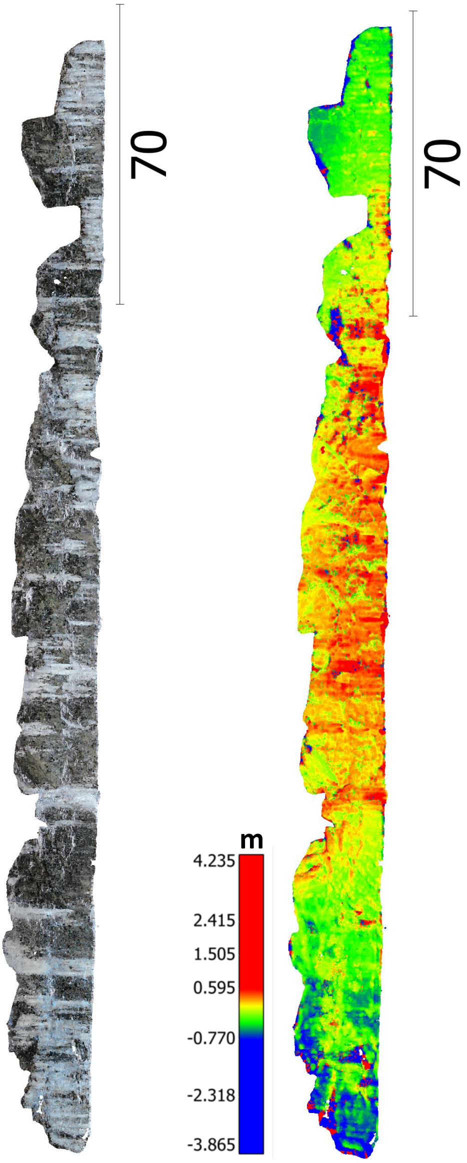

03.03.2020

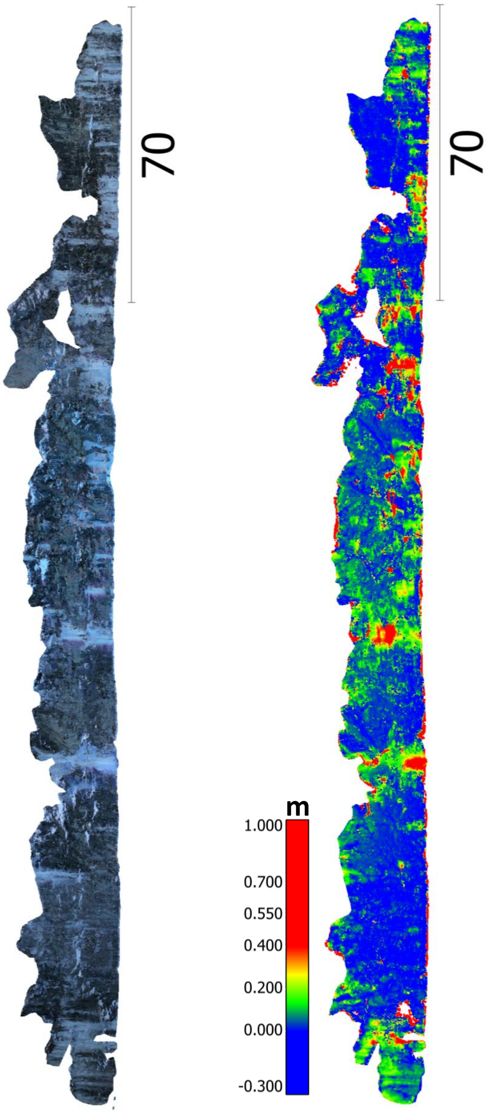

05.01.2020

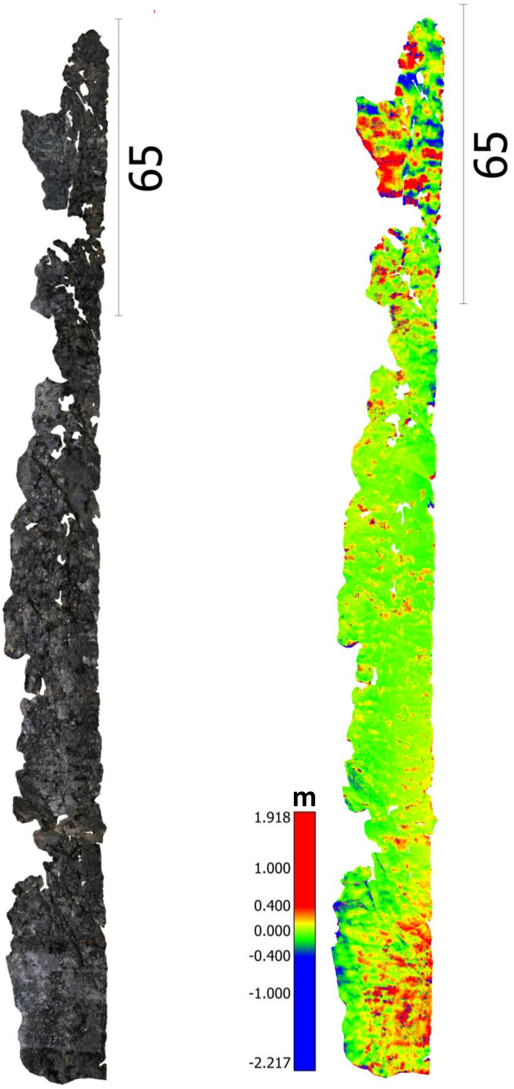

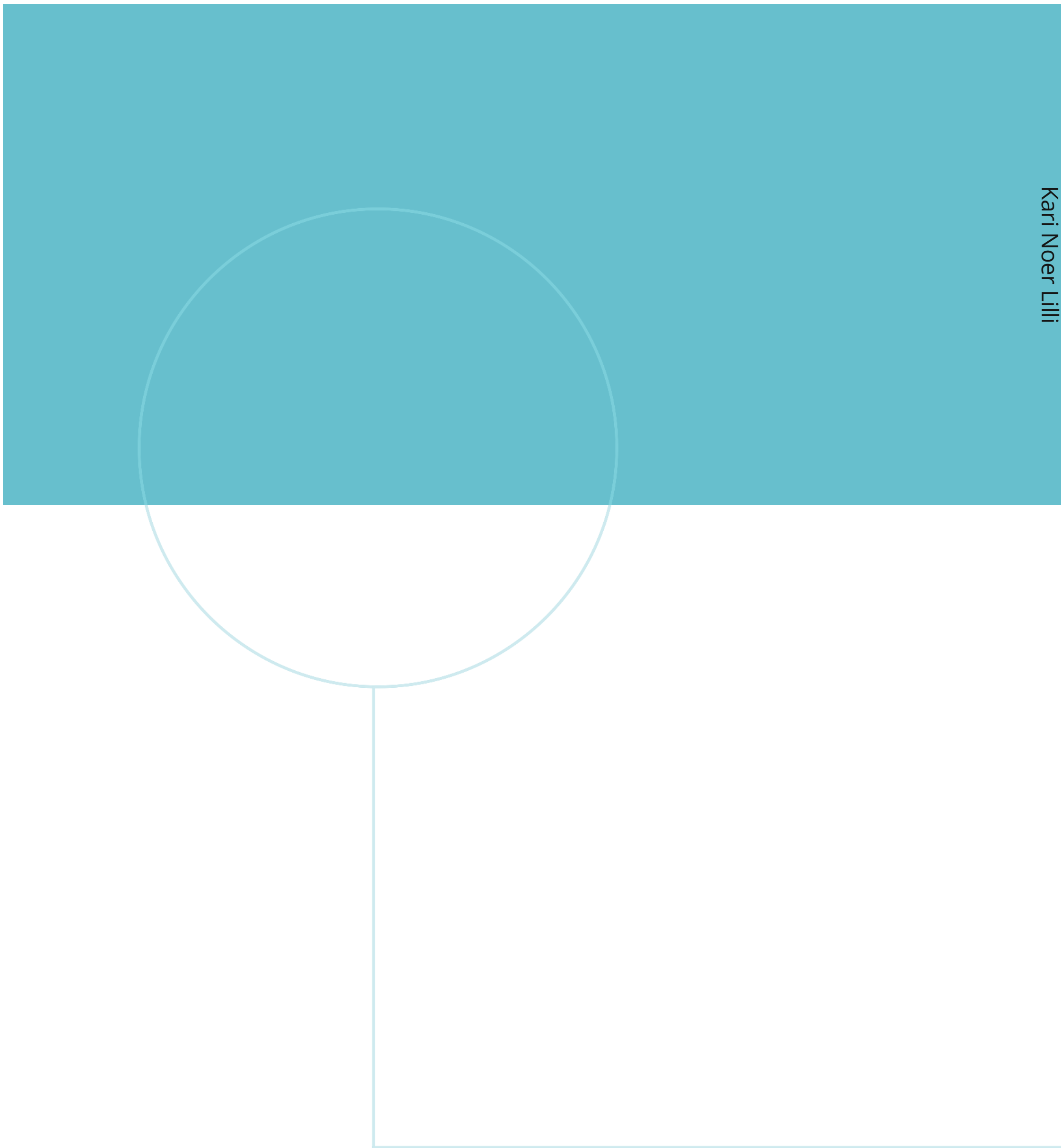

Kari Noer Lilli

NTNU
Norwegian University of
Science and Technology